



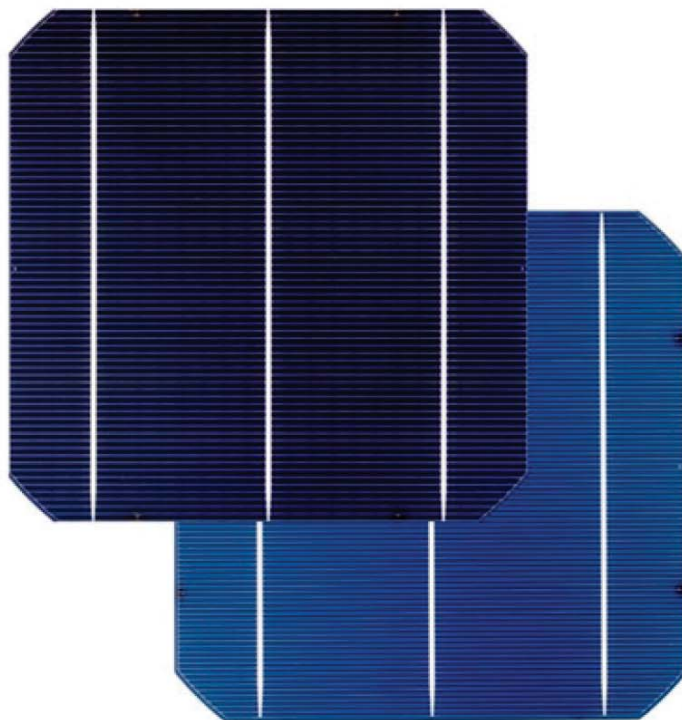
Fraunhofer
ISE

FRAUNHOFER INSTITUTE FOR SOLAR ENERGY SYSTEMS ISE

SOLAR ENERGY AND SYSTEMS RESEARCH

Philip Rothhardt

CO-DIFFUSION FOR BIFACIAL N-TYPE SOLAR CELLS



FRAUNHOFER VERLAG

Fraunhofer-Institut für Solare Energiesysteme ISE

SOLARE ENERGIE- UND SYSTEMFORSCHUNG /
SOLAR ENERGY AND SYSTEMS RESEARCH

Co-Diffusion for Bifacial N-Type Solar Cells

Philip Rothhardt

FRAUNHOFER VERLAG

Kontakt:

Fraunhofer-Institut für Solare Energiesysteme ISE
Heidenhofstraße 2
79110 Freiburg
Telefon +49 761/4588-5150
Fax +49 761/4588-9342
E-Mail info@ise.fraunhofer.de
URL www.ise.fraunhofer.de

Bibliografische Information der Deutschen Nationalbibliothek

Die Deutsche Nationalbibliothek verzeichnet diese Publikation in der Deutschen Nationalbibliografie; detaillierte bibliografische Daten sind im Internet über www.dnb.de abrufbar.
ISBN (Print): 978-3-8396-0841-8

Reihe: »Solare Energie- und Systemforschung / Solar Energy and Systems Research«

D 25

Zugl.: Freiburg, Univ., Diss., 2014

Druck: Mediendienstleistungen des
Fraunhofer-Informationszentrum Raum und Bau IRB, Stuttgart

Für den Druck des Buches wurde chlor- und säurefreies Papier verwendet.

© by **FRAUNHOFER VERLAG**, 2015

Fraunhofer-Informationszentrum Raum und Bau IRB
Postfach 80 04 69, 70504 Stuttgart
Nobelstraße 12, 70569 Stuttgart
Telefon 07 11 9 70-25 00
Telefax 07 11 9 70-25 08
E-Mail verlag@fraunhofer.de
URL <http://verlag.fraunhofer.de>

Alle Rechte vorbehalten

Dieses Werk ist einschließlich aller seiner Teile urheberrechtlich geschützt. Jede Verwertung, die über die engen Grenzen des Urheberrechtsgesetzes hinausgeht, ist ohne schriftliche Zustimmung des Verlages unzulässig und strafbar. Dies gilt insbesondere für Vervielfältigungen, Übersetzungen, Mikroverfilmungen sowie die Speicherung in elektronischen Systemen.

Die Wiedergabe von Warenbezeichnungen und Handelsnamen in diesem Buch berechtigt nicht zu der Annahme, dass solche Bezeichnungen im Sinne der Warenzeichen- und Markenschutz-Gesetzgebung als frei zu betrachten wären und deshalb von jedermann benutzt werden dürften. Soweit in diesem Werk direkt oder indirekt auf Gesetze, Vorschriften oder Richtlinien (z.B. DIN, VDI) Bezug genommen oder aus ihnen zitiert worden ist, kann der Verlag keine Gewähr für Richtigkeit, Vollständigkeit oder Aktualität übernehmen.

CO-DIFFUSION FOR BIFACIAL N-TYPE SOLAR CELLS



Dissertation
zur Erlangung des Doktorgrades der
Fakultät für Mathematik und Physik der
Albert-Ludwigs-Universität
Freiburg im Breisgau

vorgelegt von
Philip Rothhardt
aus Wuppertal

2014

Dekan: Prof. Dr. Micheal Růžička
Referent: Prof. Dr. Eicke R. Weber
Koreferent: Prof. Dr. Oliver Waldmann
Prüfungskommission: Prof. Dr. Eicke R. Weber
Prof. Dr. Andreas Buchleitner
apl. Prof. Dr. Bernd von Issendorff
Datum der
mündlichen Prüfung: 22.12.2014

Abstract

This thesis investigates the simultaneous diffusion of boron and phosphorus from an atmosphere containing POCl_3 and a borosilicate glass (BSG) layer deposited by atmospheric pressure chemical vapor deposition (APCVD).

The introduction of a second deposition phase in the POCl_3 based high temperature step allows for a controlled manipulation of the phosphorus doping, which is demonstrated by electrochemical capacitance voltage measurements. This new experimental approach allows for systematic investigation of the influence of the back surface field on bifacial n-type silicon solar cells. It is shown that a decrease in surface doping concentration leads to an increase in cell efficiency as long as inactive phosphorus is present.

The role of the surface near phosphorus doping concentration in the contact formation of silver thick film contacts is investigated by scanning electron microscopy and transmission line measurements. For the first time, the presented method allows time for a quantitative separation of the contribution of direct and indirect current conduction in silver thick film contacts. The extracted value of the specific contact resistance of a single silver crystallite of $(3.3 \pm 0.2) \mu\Omega\text{cm}^2$ agrees well with theoretical predictions.

The manifold influences of the gaseous atmosphere on boron diffusion from a BSG/ SiO_x layer stack are investigated in great detail. The most important interaction mechanism between the gaseous atmosphere and boron diffusion is mediated by the formation of an intermediate SiO_2 layer, which forms at the BSG/silicon interface. The formation of this layer is verified experimentally by ellipsometry and described quantitatively using an iterative model without free parameters.

The process sequence developed in this thesis allows for the fabrication of co-diffused bifacial n-type solar cells with peak efficiencies of 19.9 %, while reducing the process cost compared to state of the art processing by sequential diffusion.

Zusammenfassung

Diese Arbeit untersucht die simultane Diffusion von Bor und Phosphor aus einer POCl_3 -haltigen Gasatmosphäre und einem bei Atmosphärendruck abgeschiedenem Borsilikatglas (BSG).

Die Einführung einer zweiten Belegungsphase während des POCl_3 basierten Hochtemperaturschritts ermöglicht die kontrollierte Einstellung des Phosphor-Dotierprofils. Der Nachweis erfolgt mittels elektrochemischer Kapazitäts-Spannungs Messungen. Dieser neue experimentelle Ansatz ermöglicht eine systematische Untersuchung des Einflusses des Rückseitenfeldes (BSF) auf bifaziale n-Typ Siliciumsolarzellen. So wird gezeigt, dass eine Verringerung der oberflächennahen Dotierkonzentration die Effizienz der Solarzelle steigert, solange inaktiver Phosphor vorhanden ist.

Die Rolle der oberflächennahen Phosphor-Dotierkonzentration bei der Kontaktbildung durch Silber basierte Dickschichtmetallisierung wird mittels Rasterelektronenmikroskopie und der Transferlängenmethode untersucht. Die vorgestellte Methode erlaubt erstmals die Beiträge von direkter und indirekter Stromleitung quantitativ zu trennen. Dabei ergibt sich der spezifische Kontaktwiderstand eines Silberkristallits zu $(3.3 \pm 0.2) \mu\Omega\text{cm}^2$, in Übereinstimmung mit theoretischen Vorhersagen.

Die vielfältigen Einflüsse der gasförmigen Atmosphäre auf Bordiffusion aus einem BSG/SiO_x Schichtsystem werden detailliert untersucht. Der wichtigste Interaktionsmechanismus ist dabei die Bildung einer SiO_2 -Schicht an der Grenzfläche zwischen BSG und Silicium. Die Bildung dieser Schicht wird durch Ellipsometrie experimentell nachgewiesen und quantitativ durch ein iteratives Modell ohne freie Parameter beschrieben.

Die im Rahmen dieser Arbeit entwickelte Prozesssequenz ermöglicht die Herstellung von co-diffundierten bifazialen n-Typ Solarzellen mit Konversionseffizienzen von 19.9 % bei gleichzeitiger Reduktion der Prozesskosten im Vergleich zu einer Prozessierung mittels sequentieller Diffusion.

Contents

Introduction	11
1 Fundamentals	15
1.1 Fick's law of diffusion.....	15
1.2 Atomistic view of diffusion.....	16
1.3 Properties of boron and phosphorus in silicon	17
1.4 PSG layer formation	20
1.5 Oxidation models	21
1.6 Use of error bars in this thesis	23
2 Technology and characterization methods.....	25
2.1 Diffusion furnace	25
2.2 Atmospheric pressure chemical vapor deposition.....	27
2.3 Electrochemical capacitance voltage technique.....	28
2.4 Quasi steady state photoconductance measurement	29
2.5 Current voltage measurements	29
2.6 Other characterization techniques.....	30
2.7 Bifacial solar cells and Co-diffusion.....	32
3 Co-diffusion from borosilicate glass and POCl_3	35
3.1 Introduction	35
3.2 High temperature phosphorus diffusion	36
3.2.1 Experiment	36
3.2.2 Compensation of high phosphorus diffusivity by oxidation	36
3.2.3 Model for inhomogeneous phosphorus doping	42
3.2.4 Low concentration PSG sources	46
3.3 Influence of oxygen concentration on boron diffusion.....	49
3.3.1 Manipulation of boron doping profiles	50
3.3.2 Carrier concentration above solubility of boron in silicon	52
3.3.3 Discussion of carrier concentration above solubility.....	55
3.3.4 Influence of oxygen concentration in process atmosphere on boron doping profile	57

3.4	Simulation: Influence of surface depletion on cell efficiency	58
3.4.1	Introduction	58
3.4.2	Approach	59
3.4.3	Results	61
3.4.4	Discussion	64
3.5	Experimental and theoretical investigation SiO ₂ layer growth at SiO _x /Si interface	65
3.5.1	Course of experiment	66
3.5.2	Results	68
3.5.3	Discussion	69
3.5.4	Quantitative description of SiO ₂ layer growth at SiO _x /Si interface	70
3.5.5	Application of the iterative model to quantify the influence of difference parts of the process	76
3.5.6	Application of the iterative model to boron diffusion from a borosilicate glass layer	78
3.5.7	Summary	80
3.6	Influence of POCl ₃ on boron diffusion	80
3.6.1	Introduction	80
3.6.2	Experiment	82
3.6.3	Results	83
3.6.4	Discussion	89
4	Back surface fields in bifacial n-type solar cells	97
4.1	Introduction	97
4.2	Experiment	98
4.2.1	Test structures for the characterization of the back surface fields	98
4.2.2	Analytical modelling of bifacial solar cells	100
4.2.3	Fabrication of bifacial n-type solar cells	102
4.3	Electrical properties of phosphorus doped BSF	103
4.3.1	Carrier concentration and sheet resistance	106
4.3.2	Carrier recombination	106
4.3.3	Specific contact resistance	108
4.4	Discussion of electrical properties of phosphorus doped BSF	108
4.4.1	Carrier concentration and sheet resistance	108
4.4.2	Carrier recombination	109

4.4.3	Specific contact resistance	110
4.5	Selection of high temperature processes for cell fabrication.....	111
4.6	Influence of phosphorus doped BSFs on solar cells (experimental results).....	113
4.7	Discussion: Influence of phosphorus doped BSFs on solar cells.....	116
4.8	Modelling the impact of the phosphorus doped BSF on cell efficiency	118
4.9	Relevance of obtained cell efficiencies	122
4.10	Summary	123
5	Impact of surface near doping concentration on specific contact resistance	125
5.1	Introduction	125
5.2	Experiment.....	126
5.3	Results	127
5.4	Discussion and Modelling.....	131
5.5	Summary	134
6	Summary and Outlook.....	137
	Appendix	141
A	Code for the simulation of oxide growth.....	141
B	Simulation using the software tool Gridmaster	144
C	Model for lumped series resistance of BSF and base in PERT type structures.....	147
	List of abbreviations.....	151
	Bibliography.....	153
	Publications	166
	Danksagung	169

Introduction

The need to provide electrical energy without the emission of CO₂ is one of the most essential global challenges of this time [1]. Studies predict that photovoltaics will contribute considerably to solve this problem world-wide as well as in Germany [2]. Photovoltaics is not only interesting because of its application but also scientifically. The continuous development of new solar cell structures, the use of new processing methods and the steady increase in solar cell efficiency makes this field of research very dynamic.

Historically, solar cells were used mainly for space applications. In that case the cost of solar cell production was negligible compared to the transport cost, thus the aim was to increase the solar cell efficiency without being concerned much about the cost of cell production. This led to an increase in cell efficiency from less than 6 % [3] to 25 % [4], since the first introduction of a silicon solar cell in 1954.

During the last 20 years the main application has shifted from small area application in space to large area terrestrial application though. Since for large area terrestrial application photovoltaics needs to be cost competitive, especially compared to fossil fuel based technology, large scale and cost effective manufacturing of solar cells is of major importance. This requires short process sequences and the use of reliable technology.

Most current silicon solar cells are based on boron-doped (p-type) silicon, due to its resistance towards radiation damage, which was historically important for space applications. For terrestrial application the use of phosphorus-doped (n-type) silicon is more advantageous though, since it does not suffer from light induced degradation, is more resistant towards common metallic impurities e.g. iron [5] and the resistance towards radiation damage is of minor importance. Currently investigated solar cell structures based on n-type silicon include complex cell structures with comparatively high efficiencies like back contact back junction solar cells with efficiencies above 24 % [6] and hetero junction cells [7] and concepts with less process steps and efficiencies around 20 % like PhosTop [8] and bifacial n-type solar cells with peak efficiencies of 19.5 % produced using an industrial pilot line [9]. An increase in market penetration of n-type solar cells is currently hindered by highly complex processing sequences. Fortunately, significant potential for process simplification lies within the high temperature processes. In state of the art processing boron emitter and phosphorus back-surface field (BSF) are created in separate high temperature steps [9]. The technological aim

of this thesis is to develop a co-diffusion process, featuring the simultaneous diffusion of boron and phosphorus in one single high temperature step and to use this process for the fabrication of high efficiency n-type solar cells. In this approach phosphorus diffusion is based on POCl_3 based tube furnace processes, which is a widely used technology in photovoltaics. As a dopant source for boron diffusion, a borosilicate glass (BSG) layer deposited by atmospheric pressure chemical vapor deposition (APCVD) is utilized. Since APCVD does not require the use of vacuum technology this deposition technique is expected to be cost-effective and relevant for mass production.

The co-diffusion processes developed in this thesis are used for the fabrication of bifacial solar cells. Bifacial cells allow light from the front and the rear surface to enter the solar cell. Depending on the application this increases the energy yield compared to a monofacial solar cells by up to 50 % [10]. Since currently the market share of bifacial modules is negligibly small, bifaciality offers the possibility for distinction in a market that is characterized by very similar products. Historically the highest conversion efficiency of bifacial solar cells fabricated using co-diffusion was 13.7 % [11]. The aim of this thesis is to reach efficiencies around 20 %, while reducing process complexity to a point that allows for large scale cost effective industrial production of bifacial n-type solar cells.

Since high temperature processes involve a large number of parameters, historically very little quantitative research on high temperature processes for solar cells was published, especially with regard to n-type solar cells. One focus of this thesis is to find parameters that allow for a directed manipulation of doping profiles and then connect these changes to macroscopic properties of the solar cell.

During a co-diffusion process layers deposited by APCVD are subjected to an atmosphere containing N_2 , O_2 and POCl_3 at temperatures around 900°C. As a second focus thesis investigates for the first time the interaction between these gases and the dielectric layers deposited by atmospheric pressure chemical vapor deposition (APCVD). These interactions have been previously investigated [12-15] using thermally grown oxide, which has a higher degree of crystallinity than the SiO_x layers though.

This thesis is structured as follows:

Chapter 1 introduces fundamental mechanisms that are important for the understanding of this thesis.

In Chapter 2 the most important characterization techniques and machines for solar cell fabrication are described briefly. One boundary condition of the solar cells developed in this thesis is that they are “industrially relevant”, meaning amongst others that they are produced

using only equipment that is already in use in industry. For this reason all machines used in this thesis are commercially available and hence already well described in literature. The characterization techniques used in this thesis are also well known and thus need only a short description. The experimental difficulty in this thesis is thus not the introduction of a new experimental setup, but rather the preparation of samples (solar cells) that allow for investigating new effects using only well-known techniques.

The development of a co-diffusion process is described in Chapter 3. Section 3.2 discusses phosphorus diffusion at high temperatures and introduces a new method that allows for a directed manipulation of phosphorus doping profiles with unprecedented degrees of freedom. Here a major challenge consists in the homogeneous doping of single wafers. The second part of Chapter 3 discusses the influence of oxygen on boron diffusion from a borosilicate glass (BSG) layer deposited by atmospheric pressure chemical vapor deposition (APCVD). The observed influence of oxygen on boron diffusion is explained by the formation of an intermediate SiO_2 layer that forms at the Si/BSG interface. The development of an iterative model allows for describing this growth quantitatively. The influence of POCl_3 on layers deposited by APCVD is discussed in Section 3.6. Secondary ion mass spectroscopy (SIMS) measurements shown for the first time that the interaction between POCl_3 and SiO_x layers lead to the formation of a phosphosilicate glass (PSG) layer at the SiO_x /air interface. This behavior is similar to thermally grown SiO_2 layers. Within measurement accuracy the growth of a PSG layer in SiO_x may be described quantitatively by existing models.

Chapter 4 applies the previous findings to solar cells and demonstrates their relevance for application. The high temperature processes developed in Chapter 3 are used for the fabrication of bifacial n-type solar cells with peak efficiencies of 19.9 %. The used process sequence greatly simplifies solar cell fabrication compared to state of the art processing. Especially the back surface field (BSF) is characterized in detail. The influence of the back surface field on the solar cell is investigated experimentally as well as theoretically.

Chapter 5 investigates the influence of the surface near doping concentration on the specific contact resistance of screen printed contacts. Here the use of the high temperature processes developed in Section 3.2 allows for a directed manipulation of doping profiles. The influence of the doping profile on contact formation is investigated using scanning electron microscopy (SEM). In accordance to literature it is found that the area coverage of crystallites that are in direct contact with the bulk finger correlates with the specific contact resistance. For the first time this correlation is investigated quantitatively yielding the specific contact resistance of a single crystallite of $(3.3 \pm 0.2) \mu\Omega\text{cm}^2$. The introduction of a new method allows for the first time for quantitatively separating the influence of direct and indirect current conduction.

Chapter 6 summarizes the results and gives an outlook.

In the course of the author's research additional topics were covered that are not part of this thesis. For experimental results on co-diffusion from solid sources deposited by plasma enhanced chemical vapor deposition (PECVD) please refer to reference [16]. Results using the boron furnace that was put into operation as part of the author's Phd work are published by Lohmüller et al. [17, 18].

1 Fundamentals

After a brief overview of the mathematical basis of diffusion, atomistic models for impurity diffusion in silicon are introduced. Then the behavior of boron and phosphorus for concentrations above the activation limit and solid solubility is treated. Afterwards the formation of phosphosilicate glass (PSG) layers is briefly covered. Next multiple analytical descriptions for dry oxidation of silicon are described. The chapter concludes with remarks concerning the use of error bars in this thesis.

1.1 Fick's law of diffusion

This section discusses diffusion with a focus on boron and phosphorus diffusion in silicon. If not otherwise stated, this section is based on the textbook by Pichler [19].

If the distribution of atoms in a solid is not homogeneous, atomic movements occur to lead the system back towards thermal equilibrium. This process is called diffusion. In order to describe diffusion processes that are relevant for application, in general a phenomenological approach is chosen:

$$J = -D \cdot \text{grad}(c). \quad (1.1)$$

Fick's first law (1.1) connects the flow of impurities J with local variations in the concentration c by the diffusion constant D . This description of diffusion behavior is especially interesting for diffusion barriers as treated in Section 3.6. With regard to boron and phosphorus diffusion the interesting parameter is the doping concentration or more precisely its time dependent behavior. This is well described by Fick's second law (1.2). Fick's second law is presented in its one dimensional form under the assumption of a location-independent diffusion constant D , as relevant for the diffusion processes under investigation in this thesis.

$$\frac{dc(x,t)}{dt} = D(c,T) \cdot \frac{d^2c(x,t)}{dx^2}. \quad (1.2)$$

Please note that the diffusion constant D is dependent on the concentration c and the temperature T . The temperature dependence is well described by an Arrhenius relation

$$D(T) = D_0 \cdot \exp(-E_A / kT), \quad (1.3)$$

with the by the factor D_0 , the activation energy E_A , and the Boltzmann constant k . It holds for most diffusing species. The concentration dependence, however, is a property of the specific diffusing species [20-22]. In a simplified manner one may summarize: diffusion is caused by a concentration gradient, while the magnitude of the impurity flow depends on temperature and impurity concentration.

1.2 Atomistic view of diffusion

This section introduces the atomistic processes associated with the diffusion of boron and phosphorus in silicon. Boron and phosphorus in silicon both occupy predominantly substitutional lattice sites. In the case of phosphorus the dominating diffusion mechanism is concentration dependent. For concentrations below 10^{20} cm^{-3} diffusion occurs via self-interstitials, but for phosphorus concentrations above 10^{20} cm^{-3} the literature is inconclusive about the diffusion mechanism. Both vacancy and interstitial mediated diffusion describe the experimental data well [23]. In the following both vacancy and self-interstitial assisted diffusion is described on an atomic level.

Two possible mechanisms for diffusion via self-interstitials exist. The first mechanism [24] assumes that an interstitial atom (impurity or self-interstitial) moves a substitutional atom (impurity or host atom) into an interstitial site while becoming substitutional. The "new" interstitial atom now displaces another neighboring atom from its substitutional site. If one imagines the self-interstitial and the impurity to be bound, this corresponds to pair diffusion through the lattice.

A suggested diffusion mechanism for phosphorus concentrations above 10^{20} cm^{-3} is the diffusion via double negatively charged vacancies V'' [21]. The ionized donor atom and the double negatively charged vacancy experience a coulomb force and may change lattice sites. Then the donor vacancy pairs dissolves. Since the energy level introduced by V'' is 0.11 eV below the conduction band energy, a high doping concentration and a corresponding high Fermi level are needed in order to significantly increase the concentration of V'' . This could explain the onset of vacancy-mediated diffusion at high phosphorus concentrations of 10^{20} cm^{-3} .

Boron diffusion was originally proposed to be controlled by vacancies [25] and self-interstitials [26]. By introduction of self-interstitials through oxidation or suppression by nitridation, it was established afterwards that boron diffusion in crystalline silicon is

exclusively mediated by silicon self-interstitials [27]. Current experimental and theoretical evidence supports the model that a boron atom and a self-interstitial form a mobile species which then dissolves and brings boron back to its substitutional form [27].

In summary, during both boron and phosphorus diffusion the impurity atoms interact with point defects in silicon. Thus, a change in point defect concentration as caused e.g. by oxidation will affect their diffusion behavior.

1.3 Properties of boron and phosphorus in silicon

The purpose of boron and phosphorus doping in silicon within the scope of this thesis is the increase of hole or electron concentration in silicon. In a simplified picture both boron and phosphorus occupy only substitutional lattice sites in the silicon crystal structure [28]. Since the number of valence electrons of boron and phosphorus differs by one from those of silicon, in order to form a chemical bond with silicon one electron is taken (“accepted”) or given (“donated”) by each dopant. This either increases (phosphorus) or decreases (boron) the number of free electrons in the semiconductor. In this picture one electron or hole is supplied by each dopant atom. Experiments show that the fraction of ionized phosphorus and boron atoms in silicon depends amongst others on the impurity concentration. More concretely, for certain concentrations the average number of charge carriers per impurity atom introduced into silicon is smaller than one. Please note that doping, as used in photovoltaics, may either refer to the concentration of impurities or the resulting carrier concentration. While the carrier concentration is important for effects concerning conductivity, the impurity concentration is important for effects concerning recombination. Both conductivity and recombination are relevant quantities in photovoltaics.

The next paragraph discusses the physical reasons for differences in carrier and impurity concentration and estimates to which extent these are relevant for this thesis.

Two main effects are of interest: solubility and incomplete ionization. Solubility means that above a certain concentration impurities may cluster. This concentration depends on the maximum temperature of the diffusion process and is depicted in Figure 1.

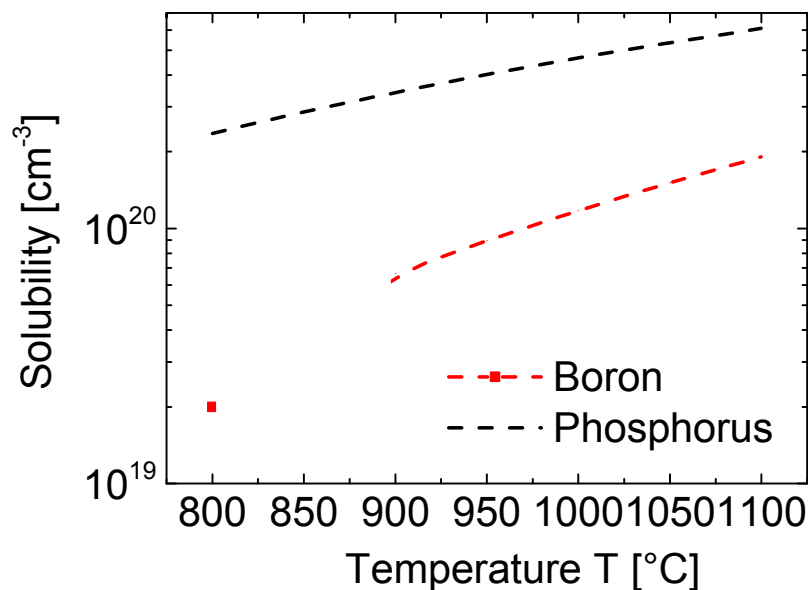


Figure 1: Solid solubility over temperature for boron and phosphorus in silicon. Phosphorus solubility after crystalline silicon [29].

Impurities in these clusters are generally electrically inactive, meaning they do not change the carrier concentration in the semiconductor. In order to show a possible magnitude of this effect Figure 2 presents a doping profile (carrier/impurity concentration over depth) taken from reference [30]. Here the carrier concentration (dots) and the impurity concentration (line) are plotted over the depth. For this doping profile the concentration of inactive phosphorus, which consists of mobile phosphorus and SiP precipitates, considerably exceeds the concentration of active phosphorus. In the case of phosphorus, the impurity concentration exceeding the activation concentration n_0 is electrically inactive, but it may be mobile or immobile depending on the concentration. The maximum active dopant concentration n_0 and the threshold concentration between mobile and immobile inactive phosphorus c_{sat} depends on temperature [30]. With regard to the application in solar cells, inactive phosphorus is reported to increase carrier recombination [31] and to play an important role in contact formation by silver thick film metallization [32].

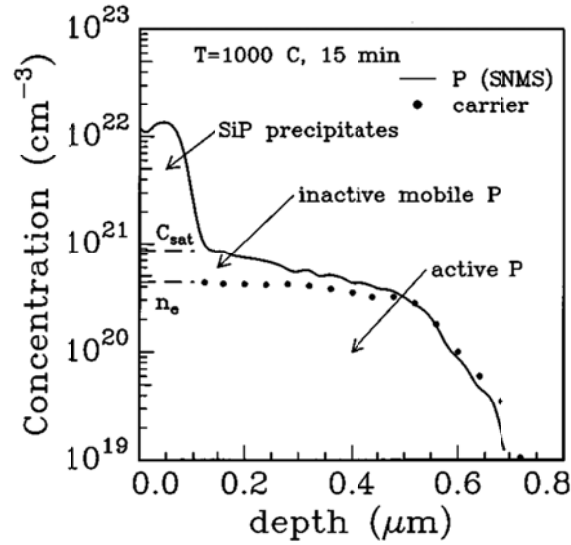


Figure 2: Phosphorus concentration in silicon determined by secondary neutral mass spectrometry and carrier concentration taken from Solmi et al. [30].

Similar but not identical effects are observed for boron doping in silicon. Similar to the behavior of phosphorus, a temperature dependent maximum concentration of active dopants is observed for boron [29]. In contrast to phosphorus, mobile but inactive boron has not been observed. For concentrations above solubility, boron in the silicon phase is in equilibrium with SiB_6 compounds which preferably form at the silicon surface. This so called boron rich layer (BRL) is generally unwanted for device application in photovoltaics, since it decreases the bulk lifetime of the silicon wafers [33] and increases surface recombination [34]. For heat treatments in an atmosphere containing nitrogen, boron rich layer thickness increases with increasing concentration of boron in the doping source, while suppression of BRL formation is possible by adding oxygen to the atmosphere [35].

A second effect that causes a difference in carrier and impurity concentration is incomplete ionization. Even below the activation limit not all impurity atoms contribute to the carrier concentration and are ionized. The magnitude of this effect depends on impurity concentration and is well described by Kuzmicz et al. [36]. There the following analytical expression is derived for the ratio between the concentration of ionized dopant atoms and the total doping concentration C_i :

$$C_i = 1 - A * \exp(-[B \cdot \ln(N / N_0)]^2), \quad (1.4)$$

with the doping concentration N and three constants A , B and N_0 that are temperature dependent and differ for different impurities. The magnitude of this effect for typical doping

profiles in this thesis is smaller than the relevant measurement accuracy. Thus this effect is of minor importance in this thesis. A third effect that might possibly cause discrepancies between carrier and dopant concentration is due to diffusion and drift of majority carriers, which occurs for abrupt changes in the impurity concentration. Since doping in this thesis is performed by diffusion, abrupt changes in the doping profile do not occur.

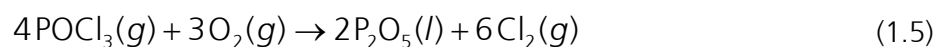
In summary: While solubility and activation are of major importance in this thesis, incomplete ionization and diffusion are of minor importance.

1.4 PSG layer formation

Subjecting silicon wafers to a high temperature step with an atmosphere containing POCl_3 , N_2 , and O_2 is the most common method in the photovoltaic industry to create phosphorus doped areas. For the bifacial cell structure under investigation in this thesis this area is called back surface field (BSF) and located at the rear side of the solar cell (Section 2.7). The chemical reaction that leads to phosphorus doping is described in this paragraph.

POCl_3 is introduced into the process atmosphere by conducting molecular nitrogen through a so called bubbler, which contains an aqueous solution of phosphoryl chloride (POCl_3). A mixture containing N_2 and POCl_3 , so called $\text{N}_2\text{-POCl}_3$, leaves the bubbler. The concentration of POCl_3 in $\text{N}_2\text{-POCl}_3$ depends on the vapor pressure. Since the vapor pressure is a function of the temperature, the temperature of the bubbler is kept constant and does not limit the accuracy of the experiments in this thesis.

The above mentioned gases react at surfaces forming P_2O_5 according to the following reactions [37]. Please note that these surfaces are not only the silicon wafer, but also the tube walls, which are part of the diffusion furnace (Section 2.1).

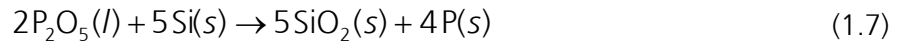


The resulting chlorine forms volatile metal compounds with possible present metal impurities and thus reduces metal contamination of the silicon wafer [38].

The reaction of gaseous oxygen and silicon results in silicon dioxide (SiO_2).



The PSG layer thus consists of SiO_2 and P_2O_5 . P_2O_5 reduces at the silicon surface forming SiO_2 and phosphorus.



The stoichiometric composition of the PSG layer depends on the O_2 and POCl_3 concentration in the atmosphere [39]. The “atomic” phosphorus that results from equation (1.7) then diffuses into the silicon wafer as discussed in Section 1.2. An understanding of PSG layer formation is important for Section 3.2.3, where the homogeneity of the doping process is explained using the chemical reactions presented in this section.

1.5 Oxidation models

This section briefly presents two analytical descriptions for dry oxidation that are applied in Section 3.5.4. “Dry oxidation” means that the process atmosphere contains O_2 , while for “wet” oxidation the process atmosphere contains H_2O (g).

The two models by Deal and Grove [12] and Massoud and Plummer [13] describe the growth of SiO_2 layers on silicon in an oxidizing ambient. The model by Deal and Grove is valid for oxide growth with a thickness above a few hundred angstroms [40] and assumes one single oxidizing species. According to this model the growth rate of the layer thickness L is described as follows:

$$\frac{dL_{DG}}{dt} = \frac{B}{(2L_{DG} + A)}. \quad (1.8)$$

The parameters B and A depend on the orientation of the silicon surface and on temperature. L_{DG} denotes the layer thickness calculated following the model of Deal and Grove. In thesis the parameterization by Moynagh et al. [41] for temperatures below 950°C and (100) oriented surfaces is used.

$$\begin{aligned} B &= 1.373 \times 10^7 \exp(-2.22\text{eV} / kT) \mu\text{m}^2 / \text{h} \\ B / A &= 4.666 \times 10^5 \exp(-1.76\text{eV} / kT) \mu\text{m} / \text{h} \end{aligned} \quad (1.9)$$

Integration of equation (1.8) for an oxidation time t_{ox} and constant A and B yields the thickness of the SiO_2 layer

$$L_{DG} = \frac{-A + \sqrt{A^2 + 4Bt_{\text{ox}}}}{2}. \quad (1.10)$$

The short and long term limits of equation (1.10) allow for a discussion of the limiting mechanism of the oxidation process. For small oxidation times $t_{ox} \ll A^2/4B$, the oxide thickness depends linearly on the oxidation time t_{ox} . In this regime the oxidation is governed by the reaction of oxygen with the silicon interface. For large oxidation times $t_{ox} \gg A^2/4B$ the oxide thickness is proportional to the square root of the oxidation time. Here the growth rate of the oxide is limited by the diffusion of oxygen through the already existing oxide layer.

A second model is introduced by Massoud and Plummer [13]. Their extension of the model by Deal and Grove adequately describes the growth rate for small layer thicknesses, where the model by Deal and Grove underestimates the growth rate. The layer thickness according to the model by Massoud and Plummer is denoted as L_{Mas}

$$\begin{aligned}
 K_1 &= 2.49 \times 10^{13} \exp(-2.18eV / kT) 10^{-20} \text{ m}^2 / \text{min} \\
 K_2 &= 3.72 \times 10^{13} \exp(-2.28eV / kT) 10^{-20} \text{ m}^2 / \text{min} \\
 \tau_1 &= 4.14 \times 10^{-6} \exp(1.38eV / kT) \text{ min} \\
 \tau_2 &= 2.72 \times 10^{-7} \exp(1.88eV / kT) \text{ min}
 \end{aligned} \tag{1.12}$$

$$\frac{dL_{Mas}}{dt} = [B + K_1 \exp(-t / \tau_1) + K_2 \exp(-t / \tau_2)] / (2L_{Mas} + A). \tag{1.11}$$

The authors also provide the following temperature dependent parameterizations for (100) oriented surfaces:

The necessity for the expansion of the model introduced by Deal and Grove is that their model underestimates the oxide growth for short oxidation times. While no widely accepted explanation for this effect exists, Massoud and Plummer suggest this to be a property of the silicon interface, which exhibits a time dependent decrease during the course of the oxidation process.

A third model that describes the growth of dry oxide in the nanometer regime is the model introduced by Han and Helms [40]. For the mathematical approach used in this thesis, this model is less appropriate compared to the model by Massoud and Plummer though. Thus in this thesis only results based on the models of Han and Helms and Massoud and Plummer are shown.

1.6 Use of error bars in this thesis

This section briefly explains the use of error bars in this thesis, since it deviates in part from conventions in photovoltaics. The following conventions exist:

For most parameters the averaged values and the standard deviation σ (represented as error bars) of the distribution are displayed. The rationale is that the distribution of the experimental data results from variations in sample preparation rather than random errors resulting from the measurement method. With respect to application the spread of the experimental data due to sample preparation, characterized by σ , is a relevant parameter, since the aim is to produce a large number of devices that are as identical as possible. This thesis deviates from this convention when the uncertainty of the average value is of interest. In order to estimate the relevance of effects σ divided by the square root of the number of samples is used. Meaning the error bars represent the standard deviation of the average value. This takes into account that the statistical error of the experimentally determined average value decreases with increasing number of samples.

Following conventions IV Data, which includes efficiency, open circuit voltage, and short circuit current determined at the Calibration laboratory Callab are displayed with errors representing a confidence interval of 95 %. The error bars include systematic and random contributions.

2 Technology and characterization methods

All experiments conducted in this thesis are based on commercially available equipment. As long as well-known methods allow for extraction and interpretation of the data and the signal is well above the measurement accuracy, in the following only short remarks and a list of more detailed references are given. For techniques where signals are detected that are either close to measurement accuracy or where fundamentally new correlations are observed, a short presentation of the underlying physical mechanism and measurement accuracy are given.

2.1 Diffusion furnace

The diffusion furnace is the most frequently used machine in this thesis. It is the commercially available horizontal quartz tube furnace E 2000 XL by Centrotherm Photovoltaics. Since this type of furnace has been used for a few decades the experimental setup is only described briefly. The gas inlet, where the process gases enter the tube is placed on the left side in Figure 3. The gases then propagate through the tube and leave the tube through the small

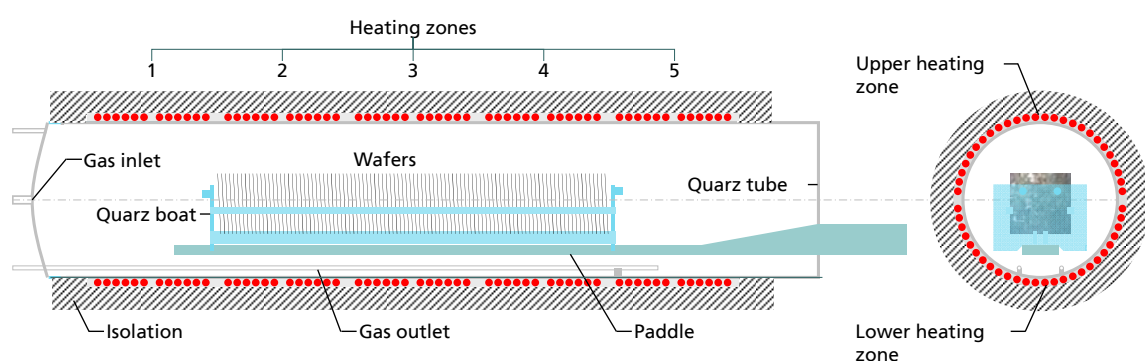


Figure 3: Schematic cross and longitudinal section of the quartz tube taken from reference [42].

gas outlet tube which is placed at the bottom of the quartz tube and has an open end on the right side. It is not exactly known, how the gas propagates through the tube. Simulations

2.1 Diffusion furnace

suggest turbulences and local variations in the gas velocity, which depend on the specific design of the quartz tube [43-45]. The temperature in the quartz tube is regulated by 10 heating zones, 5 at the top and 5 at the bottom of the quartz tube. The wafers are placed in a quartz boat, which is transported into the quartz tube by a so called "paddle". The process gases used in this thesis are O_2 , N_2 and N_2 - $POCl_3$. N_2 - $POCl_3$ denotes N_2 , which passes through a $POCl_3$ bubbler and contains gaseous $POCl_3$. The relevant process parameters for a high temperature process in this thesis are the evolution of the temperature T and the gas flows, which are denoted by Q_{gastype} . Please note that due to intellectual property rights it is not possible to publish the exact temperatures and gas flows for high temperature processes in this thesis. Instead the qualitative evolution of the temperature and the absolute values of parameters that are varied are given, while the gas flows that are constant remain undisclosed. The temperature in the tube is measured with an accuracy of $\pm 1^\circ\text{C}$, while the accuracy of the gas flows depends on the type of process gas. An overview is given in Table 1.

Table 1: Accuracy of mass flow controllers of the diffusion furnace.

Process gas	Error of absolute value [slm]	Reproducibility [slm]	Minimum flow rate [slm]
N_2 - $POCl_3$	0.03	0.006	0.06
N_2	0.3	0.06	0.6
$O_2 < 3$ slm	0.03	0.006	0.06
$O_2 > 3$ slm	0.3	0.06	0.6

The error of the absolute value is shown in the second column while the uncertainty to which a gas flow may be reproduced, called "reproducibility" is displayed in the third column. The minimum flow rate denotes the maximum gas flow when the mass flow controller is in the "closed" state. The placement of additional valves that are either open or closed prevents these gases from reaching the diffusion tube though, if a gas flow of zero is chosen. The oxygen gas flow Q_{O_2} may be regulated by two mass flow controllers, one with a maximum gas flow of 3 slm and the other with a maximum gas flow of 30 slm. Following the notation in literature gas flows in this thesis are given in slm (standard liter per minute) or sccm (standard cubic centimeter per minute). 1 slm corresponds to $1.68875 \text{ Pa}\cdot\text{m}^3/\text{s}$ in the international system of units (SI).

2.2 Atmospheric pressure chemical vapor deposition

In this thesis atmospheric pressure chemical vapor deposition (APCVD) is used to deposit borosilicate glass (BSG) and undoped SiO_x layers. Atmospheric pressure means that the deposition process occurs at atmospheric pressure. This is interesting for application since it makes the experimental setup very simple, and the machine cheaper, especially compared to the more frequently used plasma enhanced CVD (PECVD). While APCVD has been used extensively in the microchip industry the applications in photovoltaics have been very scarce.

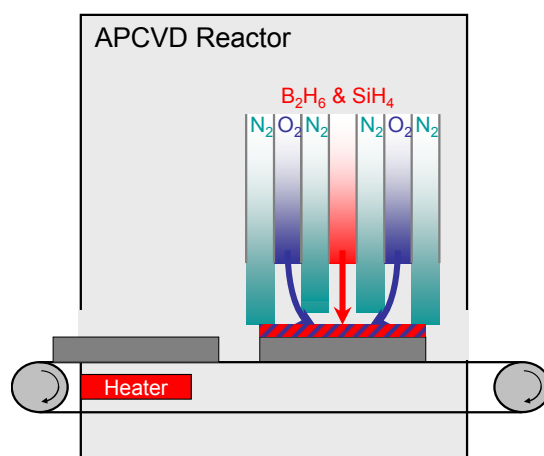


Figure 4: Sketch of the reactor and one injector used for the deposition of dielectric layers by atmospheric pressure chemical vapor deposition (APCVD)

Figure 4 presents a sketch of the APCVD system. For the experiments in this thesis depositions take place with an inline APCVD machine by SCHMID group located in the research facility of SCHMID Group in Freudenstadt, Germany. The inline deposition process works as follows. Wafers are placed on a moving belt and are heated to a process temperature of around 350°C. Then they pass three injectors, where different process gases are lead towards the wafer and form a dielectric layer. In this thesis the first injector is used for deposition of a BSG layer while the second and third are used to deposit undoped SiO_x layers, which are also referred to as “capping layers”. While the process gases SiH_4 and O_2 allow for the formation of SiO_x layers, for the formation of a BSG layer diborane (B_2H_6) is added. This boron precursor diborane is let into the atmosphere diluted with a concentration of 5 % in nitrogen. So called “N₂ curtains” protect the APCVD reactor chamber and the injectors from contamination and allow for a well contained deposition of the doped glass on the wafer only. Please note that for the notation of layer stacks the layers are given in the order of the deposition or in other words, the first layer is located directly on the silicon wafer surface, while the others are further away from the wafer surface.

2.3 Electrochemical capacitance voltage technique

Electrochemical capacitance voltage (ECV) measurements are used to characterize the doping of silicon wafers or more precisely the depth dependent charge carrier concentration. This section briefly introduces the measurement principle and experimental limitations. For further information please refer to references [46-48].

ECV is a destructive method, which allows for the determination of the depth-resolved charge carrier concentration on Si wafers with a planar surface. While a measurement on a textured surface is generally viable, extraction of the carrier concentration relies on assumptions concerning e.g. the increase in surface area compared to a planar surface and the depth of the etched craters. Values for the surface enlargement vary in literature [49, 50], thus in this thesis, ECV measurements are performed on planar surfaces. For the description of solar cells some interpretation is nevertheless needed, since the relevant solar cells in this thesis feature exclusively textured surfaces.

During the experimental procedure capacitance-voltage (CV) measurements and electrochemical etching steps are performed alternately. Each CV measurement provides the carrier concentration n at the wafer surface according to

$$n = \frac{2}{e\epsilon\epsilon_0 A^2} \frac{d}{dV} C^{-2}, \quad (2.1)$$

with the elementary charge e , the relative permittivity of silicon ϵ , the permittivity of vacuum ϵ_0 and the contact area between electrolyte and sample A . The evaluation of equation (2.1) in the linear range of $C^2(V)$ yields the carrier concentration at the wafer surface.

Etching the surface and subsequently performing a new CV measurement yields the depth dependent doping concentration. The etch depth is measured by integrating the etch-current that flows during etching and measurement.

The main contributions to measurement uncertainty result from errors in A and an inaccurate calculation of the etch depth. In order to guarantee high measurement accuracy in this thesis both area and depth are periodically measured directly using confocal laser scanning microscopy and compared to the assumptions used to extract the doping profile.

2.4 Quasi steady state photoconductance measurement

The quasi steady state photoconductance (QSSPC) method extracts the minority carrier lifetime, by measuring the decay of photo induced conductance [51, 52]. The resulting value is the effective carrier lifetime τ_{eff} , which characterizes the lumped bulk and surface recombination. The lower the value of τ_{eff} , the higher the recombination. Even though QSSPC is a well-known technique, the results obtained by different researchers are hardly comparable since different research institutions use different models, assumptions and wafer material. In order to investigate the comparability of QSSPC measurements the author of this thesis fabricated QSSPC samples in close collaboration with the PhD student A.Kimmerle and extracted the dark saturation current density J_0 using different methods [53]. This publications also discusses the influence of the sample type on the results of the QSSPC measurement. For details concerning the experimental setup please refer to [54]. According to specifications of the QSSPC tool, the measurement accuracy is 10 % for a single measurement.

2.5 Current voltage measurements

Most current voltage (IV) measurements in this thesis are obtained using a commercially available industrial cell tester at “standard test conditions” [55]. A detailed discussion of the IV parameters is published in a textbook [37]. For details of the setup please refer to references [56, 57]. Selected solar cells are also measured at Fraunhofer ISE Callab PV Cells. In the following the measurement errors represented by twice the standard deviation that are relevant for the samples investigated in this thesis are stated. This means that 95 % of the values are expected to lie within this interval. The aim of this table is to facilitate the interpretation of the experimental data in this thesis.

Table 2: Measurement error for IV parameters for the industrial cell tester and measurement at Callab.

Cell tester	error	V_{oc} [% _{rel}]	J_{sc} [% _{rel}]	η [% _{rel}]	FF [% _{rel}]
Industrial	Relative	0.04	0.03	0.1	0.07
Industrial	Absolute	0.7	2.8	3.1	1
Callab	Absolute	0.5	2.5	3	1

Absolute errors represent the measurement uncertainty for measurements compared with the “true” values. The relative error represents the uncertainty for comparing measurements of the same cell structure that were taken during the same day on one machine. Measurements by Fraunhofer ISE CalLab PV Cells are used in the photovoltaic community for relative comparison of solar cell efficiencies, for cells produced at different institutes. By comparing efficiencies measured using the same experimental setup and reference cell, the effect of systematic errors may be minimized.

2.6 Other characterization techniques

This section gives an overview of other characterization techniques used in this thesis. Since many of these techniques were originally developed for the semiconductor chip industry, today these techniques are well established and the measurement devices are commercially available. Thus these techniques are only described briefly. For the interested reader further references are provided.

The **transfer length method** (TLM), which is sometimes also referred to as transmission line method allows the extraction of the specific contact resistance of e.g. screen printed contacts. It was developed in 1964 [58] and later refined [59-61]. Detailed information is available in reference [46]. An overview treating the contact resistance with respect to the application in photovoltaics is given by Schroder et al. [62].

Secondary ion mass spectroscopy (SIMS) measurements in this thesis are performed at SGS Institut Fresenius GmbH using a Cameca IMS 7F setup. The measurement principle is as follows: Primary ions are accelerated towards a target. The collision of these primary ions with the target generates secondary ions that are then analyzed in a mass spectrometer. The amount of secondary ions then correlates with the concentration of this species in the target. Please note that strictly this only holds, if the matrix that contains the impurity is uniform. For the samples investigated in this thesis this may not be always the case, thus often only relative values are compared. As a drastic example, the ion yield may differ by up to 3 orders of magnitude for bare silicon and silicon dioxide [63]. In this thesis the concentration of oxygen, silicon, boron and phosphorus in SiO_x and BSG layers are of interest. In order to obtain quantitative results, well known standard samples with a known impurity concentration are used. For the creation of negatively charged secondary ions (^{30}Si , ^{18}O and ^{31}P), Cs^+ ions with an energy of 5 keV are used as primary ions. Primary O_2^+ ions with an energy of 5 keV create positively charged secondary ions (^{10}B , ^{11}B , ^{30}Si). For both ions O_2^+ and Cs^+ the measurement spot is circular with a diameter of 70 μm . The depth is calibrated using the sputter rate of a thermal SiO_2 layer. The quantification of the phosphorus and boron

concentration, meaning the conversion from measured counts per second to concentration is based on reference implantations of boron and phosphorus in thermally grown SiO_2 . The depth resolution is 1-5 nm. For more details please refer to reference [46].

Ellipsometry is used in this thesis to determine the layer thickness and the refractive index of dielectric layers. Ellipsometry measures the cumulated change in polarization caused by the transmission through a dielectric layer (stack). Layer stacks in this thesis are investigated by spectral ellipsometry, meaning ellipsometry at multiple wavelengths. This increases measurement accuracy [46]. For the extraction of the data a Cauchy model is used. The experimental setup is illustrated in reference [64].

Scanning electron microscopy (SEM) allows for the characterization of the microstructure e.g. of semiconductors. An electron beam is accelerated towards a sample with a typical energy in the range of keV. The interaction with the sample results in electron and photons that are emitted from the sample and detected. By scanning the beam over the sample different positions on the sample are correlated with the detected intensity of electrons. Changes in the signal of secondary electrons are dominated by changes in the sample topography, but may also be due to differently charged areas [65] or chemical bonds. Again a good introduction to the measurement principle is provided in reference [46]. The spatial resolution is in the order of a few nanometers and is determined by the diameter of the electron beam. Since the structures resolved in this thesis are larger than 100 nm, the spatial resolution of the SEM measurement is not a relevant limitation.

Inductive and four point probe measurements probe the sheet resistance R_{sh} , which is a property of a doping profile. Both inductive and four point probe measurements are well established. In this thesis the sheet resistance is measured inductively at 66 spots per wafer,

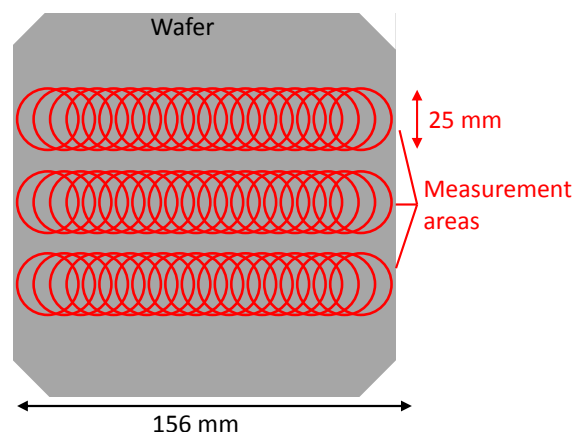


Figure 5: Schematic representation of the inductive sheet resistance measurement pattern.

which are distributed along 3 straight lines across the wafer (Figure 5). The sheet resistance of one wafer is then characterized by the average sheet resistance and the standard deviation of the sheet resistance over the wafer. Please note that this standard deviation does not represent the experimental uncertainty of the average value, but rather characterizes the homogeneity of the doping over one wafer. For 4 point probe measurements the measurements points are generally distributed equally spaced over the wafer. In comparison with the measurement pattern presented in Figure 5, this results in a larger standard deviation of the sheet resistance. For details concerning these methods refer to references [66] and [46]. Sheet resistance describes the resistance of a square two dimensional film, which is a property of the integrated specific conductance. In order to distinguish the sheet resistance from the electrical resistance, the unit of R_{sh} is denoted not as Ω but as "Ohm per square" Ω/sq [67].

2.7 Bifacial solar cells and Co-diffusion

This paragraph describes the terms "bifacial solar cell" and "co-diffusion". The schematic cross section of a bifacial solar cell based on n-type silicon is depicted in Figure 6.

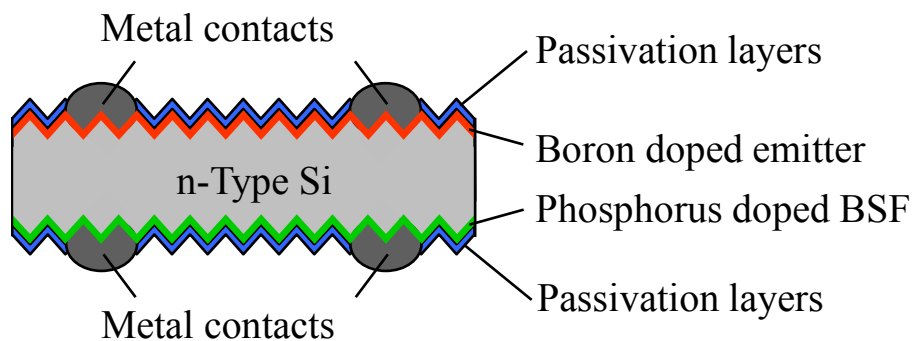


Figure 6: Schematic cross section of a bifacial n-type solar cell. Please note that the solar cell is not drawn to scale. The wafer thickness is roughly $180\ \mu\text{m}$, the depth of the emitter and BSF around $500\ \text{nm}$, the thickness of the passivation layers around $100\ \text{nm}$ and the width and height of the metal contacts 50 respectively $20\ \mu\text{m}$.

A bifacial solar cell features an open front and rear grid. This means that the metal contacts both on the emitter and back surface field (BSF) do not cover the whole wafer surface. This allows light incident from the front and the rear side to enter the solar cell and generate electron hole pairs. Bifacial solar cells investigated in this thesis are based on textured n-type Czochralski grown (Cz) silicon wafers with a thickness of around $180\ \mu\text{m}$. The full area boron

doped emitter and the phosphorus doped BSF extend roughly 500 nm into the wafer. Both emitter and BSF are covered by so called dielectric passivation layers with a thickness of roughly 100 nm. The metal contacts, which are referred to as metallization, with a width of around 50 μm and a height of approximately 20 μm allow for current extraction.

Co-diffusion refers to the process sequence that is used to form the boron and phosphorus doped areas. Current state of the art processing uses "sequential diffusion", which requires one high temperature step each for boron (BBr_3 or BCl_3) and phosphorus (POCl_3) diffusion. An exemplary process sequence featuring 5 process steps is depicted in Figure 7 a). The aim of co-diffusion is to create the same doping profiles as results from sequential diffusion, but using less process steps. This ultimately reduces the production cost of solar cells, which is important for industrial application. The approach to co-diffusion using 2 process steps, which is followed in this thesis, is shown in Figure 7 b). The first process step is the deposition of a borosilicate glass (BSG) layer and a SiO_x layer on one side of the wafer using APCVD. This is followed by a high temperature step in an atmosphere containing POCl_3 . Thus co-diffusion reduces the number of process steps by 3 compared to sequential diffusion. This is a relevant reduction, since the production of bifacial solar cells requires roughly 11 process steps in total. The development and characterization of this co-diffusion process is displayed in Chapter 3, while the application to solar cells is demonstrated in Chapter 4.

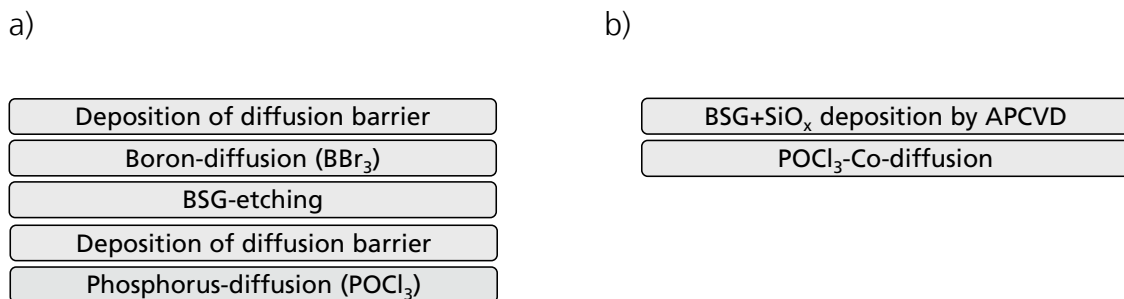


Figure 7: Process sequences for the formation of boron emitter and phosphorus BSF using a) sequential diffusion b) co-diffusion.

3 Co-diffusion from borosilicate glass and POCl_3

3.1 Introduction

This section describes the development of a co-diffusion process from a borosilicate glass (BSG) layer deposited by atmospheric pressure chemical vapor deposition (APCVD) and an atmosphere containing POCl_3 . The objective is a short high temperature process that allows for a simultaneous diffusion of the desired amount of boron and phosphorus into the silicon wafer, both boron and phosphorus doping being single-sided. Additionally an independent manipulation of doping profiles is required in order to investigate the influence of boron and phosphorus doping profiles on solar cell performance, since the optimum doping profiles that allow for maximum cell efficiency are unknown. In order to reach these aims the following topics will be addressed:

While the required doping profiles of boron and phosphorus are comparable in depth and surface concentration, the effective diffusivity of phosphorus is higher than that of boron by about one order of magnitude [68]. In sequential diffusion processes, this was historically compensated by using different temperatures for boron and phosphorus diffusion [69]. Since now boron and phosphorus diffuse simultaneously, a new approach needs to be identified that allows for the formation of adequate phosphorus and boron doping profiles.

In order to prevent cross-contamination, meaning the diffusion of phosphorus into the boron doped emitter, the diffusion of phosphorus through SiO_x layers deposited by APCVD needs to be minimized. Since the diffusion of phosphorus through thermally grown SiO_2 layers has been investigated in detail [70, 71], it has to be studied to which extend the diffusion behavior of a phosphorus containing species through the amorphous SiO_x layers may be described by existing models.

Furthermore it is unknown in which ways other components of the gaseous atmosphere interact with the APCVD layers and how this influences boron doping.

Following this argumentation Chapter 3 covers three main topics: firstly phosphorus diffusion at high temperatures; secondly the influence of oxygen in the process atmosphere on boron diffusion from BSG layers, and thirdly the interaction of POCl_3 with the APCVD deposited layer stack and the resulting boron doping.

3.2 High temperature phosphorus diffusion

Using boron doped layers deposited by plasma enhanced chemical vapor deposition (PECVD), it was shown that a high temperature process with a plateau at 950°C and a duration of 30 min allows for adequate boron doping [72]. Therefore all co-diffusion processes developed in this thesis comprise at least one plateau with a temperature of 950°C and a duration of 30 min. In this section two approaches for phosphorus diffusion at high temperatures are investigated. In the first approach the high diffusivity of phosphorus is compensated by in-situ oxidation. In the second approach an extremely low dose of phosphorus in the dopant source counteracts the high diffusivity. In addition this section presents a method for a controlled manipulation of a phosphorus doping profile.

3.2.1 Experiment

The sequence of the experiment is the same for Sections 3.2.2, 3.2.3 and 3.2.4 (Figure 8). Saw damage etched Czochralski (Cz) grown p-type silicon wafers with an edge length of 156 mm are subjected to a POCl_3 based high temperature step in a diffusion furnace (Section 2.1). Afterwards the PSG layer thickness d_{PSG} and sheet resistance R_{sh} are determined by ellipsometry and inductive measurements respectively. The carrier concentration profiles are measured by ECV after removal of the phosphosilicateglass (PSG), a so called “PSG etch”, in an HF based solution.

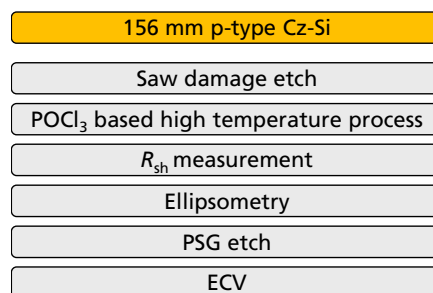


Figure 8: Schematic representation of the experiments in Sections 3.2.2, 3.2.3, and 3.2.4.

3.2.2 Compensation of high phosphorus diffusivity by oxidation

In the following first a motivation of the respective approach and then the results are presented. In this approach a high concentration dopant source similar to those used for the fabrication of phosphorus emitters for p-type solar cells is utilized. Since these high temperature processes typically involve temperatures below 850°C, high temperature phosphorus diffusion means that the diffusion temperature is around 100°C higher than for

emitter formation in p-type solar cells. Thus without additional oxidation the high concentration dopant source in combination with the high temperature leads to a very high doping concentration which in turn causes recombination which has a detrimental effect on solar cell efficiency. The increase of O₂ concentration in the process atmosphere (during phase R1B in Figure 9) after formation of the PSG layer leads to a growth of a SiO₂ layer at the PSG/Si interface [73, 74]. This layer causes two effects. Due to the fact that the diffusivity of phosphorus in SiO₂ is smaller than in PSG, the SiO₂ layer acts as a diffusion barrier between the PSG and the silicon, decreasing further diffusion of phosphorus into the silicon bulk [75]. The other effect is that silicon needed for the formation of the SiO₂ layer is taken from the bulk silicon. Thus a fraction of the already doped bulk silicon is converted into SiO₂ decreasing the total amount of doped bulk silicon. Additionally thermal oxidation leads to enhanced phosphorus diffusion through the introduction of silicon self-interstitials and a redistribution of the dopant [76]. The first issue under investigation is if this so called “in-situ oxidation approach” in combination with a highly doped dopant source allows for sufficiently low phosphorus doping concentrations or in other words if there are enough degrees of freedom, to achieve adequate doping profiles. A second aim is to find parameters that allow for a systematic manipulation of doping profiles.

Figure 9 a) presents a high temperature processes featuring an atmosphere containing POCl₃ and in-situ oxidation, while Figure 9 b) illustrates the resulting doping profiles. During the PSG deposition step (R1a), which takes place during the ramp up, N₂, O₂, and POCl₃ react to form a highly doped PSG layer on the wafer surface, as described in Section 1.4. Following PSG deposition, the N₂-POCl₃ gas flow stops and the oxygen gas flow increases, while the N₂ gas flow is adjusted to maintain a constant total gas flow. This step is the so called in-situ oxidation step (R1b). A detailed investigation of this in-situ oxidation step is currently submitted for publication [77]. For the remaining duration of the high temperature process only N₂ is injected in the diffusion tube. The investigated N₂-POCl₃ gas flows range from 0.6 to 1.8 slm. The resulting effect on the doping profiles is presented in Figure 9 b).

Results

Varying Q_{POCl_3} between 0.6 and 1.8 slm allows for reaching a large range of sheet resistances between 500 and 78 Ω/sq . As expected an increase in Q_{POCl_3} leads to an increase in doping concentration and thus to a decrease in R_{sh} . The depth (determined at 10^{17} cm^{-3}) and surface concentration of the doping profiles vary from 200 to 450 nm and from 7×10^{18} to $5 \times 10^{19} \text{ cm}^{-3}$, respectively. For contact formation by screen printing, the surface concentration is too low, since currently concentrations above $1 \times 10^{20} \text{ cm}^{-3}$ are needed [32]. Nevertheless

3.2 High temperature phosphorus diffusion

these doping profiles are suitable for a wide range of applications, e.g. as a front surface field (*FSF*) for back contact back junction solar cells or in interplay with plated metallization. As is

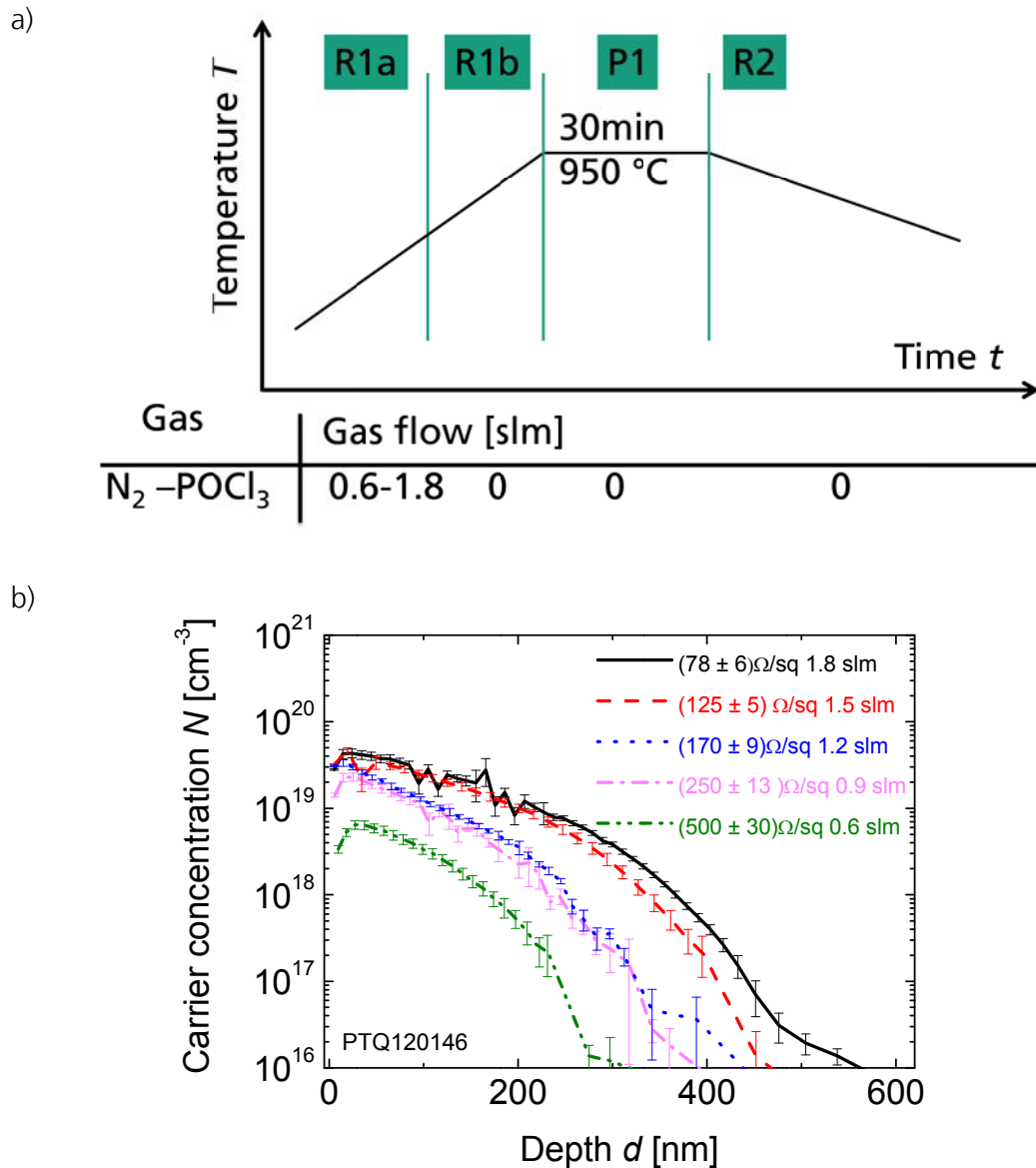


Figure 9: a) Schematic representation of the high temperature processes featuring one deposition phase (R1a) and in-situ oxidation (R1b). b) Carrier concentration over depth resulting from the high temperature processes depicted in a) measured by ECV in the center of the wafer. The error bars represent the measurement accuracy of a single ECV measurement. The different high temperature processes are labelled with their corresponding sheet resistance R_{sh} averaged over 3 wafers, its average standard deviation over one wafer (inductively measured), and N₂-POCl₃ gas flow [78].

common for POCl₃ based diffusion, a change in one process parameter influences both surface concentration and depth simultaneously. The simultaneous change in surface

concentration and depth caused by a change in Q_{POCl_3} is due to the fundamental physics of Fick's law of diffusion (equation (1.2)): A change in Q_{POCl_3} leads to a change in the phosphorus concentration in the PSG layer [79]. This increases the surface doping concentration and also the concentration gradient of phosphorus and thus the flux of phosphorus atoms into the wafer. Since the optimum doping profile for the application in solar cells is not known yet, it is of major importance to investigate the influence of surface concentration and depth on solar cell parameters separately. Thus the development of a high temperature process is needed where surface concentration and depth may be adjusted independently. This requires additional degrees of freedom. To reach this aim a second PSG deposition phase is added resulting in a high temperature process depicted in Figure 10 a). The second deposition step is performed on a plateau of constant temperature (P2) during ramp down (R2), while the remaining high temperature process remains unchanged. During the second deposition step $\text{N}_2\text{-POCl}_3$ is introduced into the process atmosphere.

Figure 10 b) shows the influence of the $\text{N}_2\text{-POCl}_3$ gas flow during this second plateau. Again an increase in Q_{POCl_3} leads to a decrease in sheet resistance. The standard deviation of the sheet resistance over one wafer is below 5 % relative for all processes, which is generally considered suitable for application. Interestingly this change in sheet resistance is mainly caused by an increase in the surface near doping concentration. The depth of the doping profile changes only marginally within the measurement accuracy, while the active surface doping concentration varies from 8×10^{19} to $3 \times 10^{20} \text{ cm}^{-3}$, where the latter is the activation limit of phosphorus in silicon. The phosphorus above this activation limit is inactive, meaning it does not contribute to the carrier concentration and is thus not detected by ECV [80]. The surface doping concentrations achieved by this approach are in the range that allow for contact formation by screen printing [32]. The application of this high temperature process to solar cells thus allows for the first time the investigation of the influence of phosphorus surface concentration independently from variation in the depth.

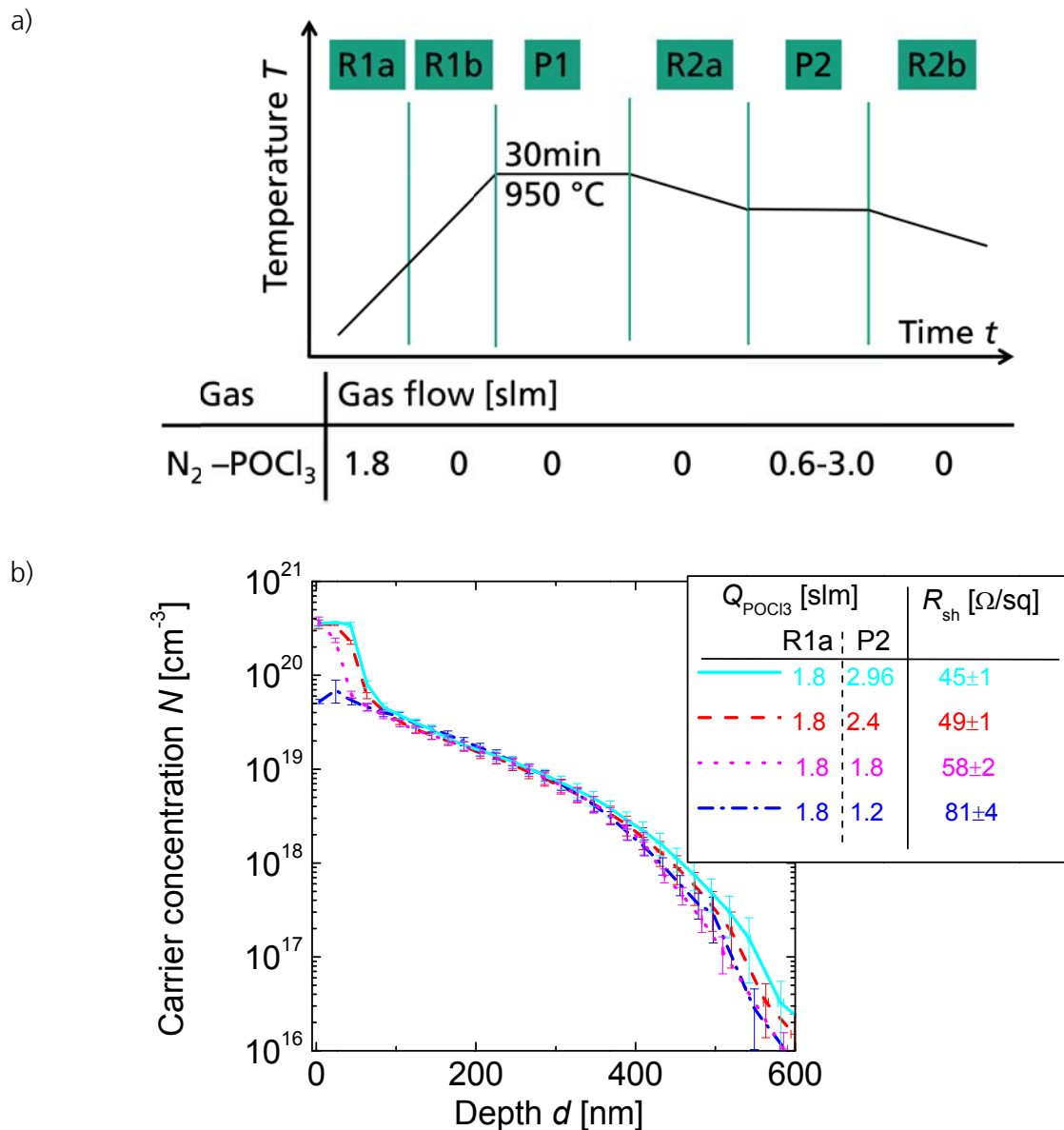


Figure 10: a) Schematic representation of high temperature processes featuring in-situ oxidation and two deposition phases. b) Carrier concentration over depth resulting from high temperature processes depicted in a) measured by ECV in the wafer center. The error bars represent the measurement accuracy of a single ECV measurement. The different high temperature processes are denominated by their sheet resistance R_{sh} averaged over 3 wafers, its average standard deviation over one wafer (inductively measured), and N₂-POCl₃ gas flows during first (R1a)/second (P2) deposition phase.

Summing up, this section presents a newly developed flexible high temperature process using in-situ oxidation and two deposition phases. By changing the N₂-POCl₃ gas flow a directed

manipulation of doping profiles is possible. The wide range of achievable doping concentrations makes this process suitable for application in different cell concepts, while the process temperature allows for simultaneous adequate boron doping [72]. The detailed investigation of the influence of Q_{POCl_3} on sheet resistance (Figure 9 and Figure 10) also allows for a deeper understanding of the technical aspects of the diffusion process. As an example the following section investigates the reason for inhomogeneous doping resulting from POCl_3 based high temperature processes.

3.2.3 Model for inhomogeneous phosphorus doping

For technical application in solar cells the spatial homogeneity of the doping process is important. In other words doping profiles for different positions on one wafer and for different wafer positions in the diffusion boat need to be approximately the same. This section discusses the homogeneity of the doping process over one wafer with the aim to find the underlying physical mechanisms and deduct possible strategies for increasing doping homogeneity.

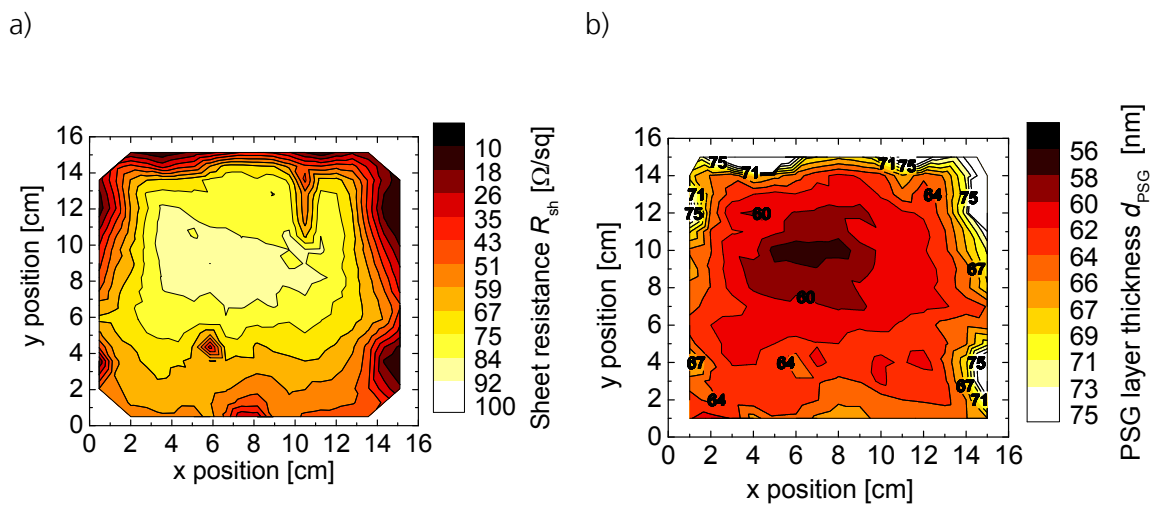


Figure 11: a) Sheet resistance over wafer surface determined by 4 point probe measurement
 b) Distribution of the PSG layer thickness over the wafer surface determined by ellipsometry using a fixed refractive index of $n=1.57$.

In theory many different causes for doping inhomogeneity are possible, to name only a few: The temperature of the wafer surface might be inhomogeneous, inhomogeneities might be caused by the wet chemical pre-treatment of the wafers, the gaseous atmosphere might vary locally, etc. To the author's knowledge none of these possibilities have been discussed in

detail though. The approach to this question is as follows. First a hypothesis is derived, then verified qualitatively and tested quantitatively.

Figure 11 presents the sheet resistance distribution over the wafer surface of a planar wafer determined by 4 point probe measurements resulting from a high temperature process with a N₂-POCl₃ gas flow of 1.8 slm in the first deposition phase (Figure 9) and the corresponding distribution of the thickness of the PSG layer determined by laser ellipsometry.

The sheet resistance increases towards the center of the wafer, while the corresponding PSG layer thickness decreases. In general PSG layer thickness and sheet resistance seem to correlate. The following section suggests a physical mechanism for this correlation and describes the relation between d_{PSG} and R_{sh} quantitatively.

A possible explanation for the increase in R_{sh} and the decrease in d_{PSG} towards the center of the wafer is a simultaneous reduction of the POCl₃ concentration in the process atmosphere due to the reaction presented in equation (1.5). This view is supported by measurements presented in Figure 12.

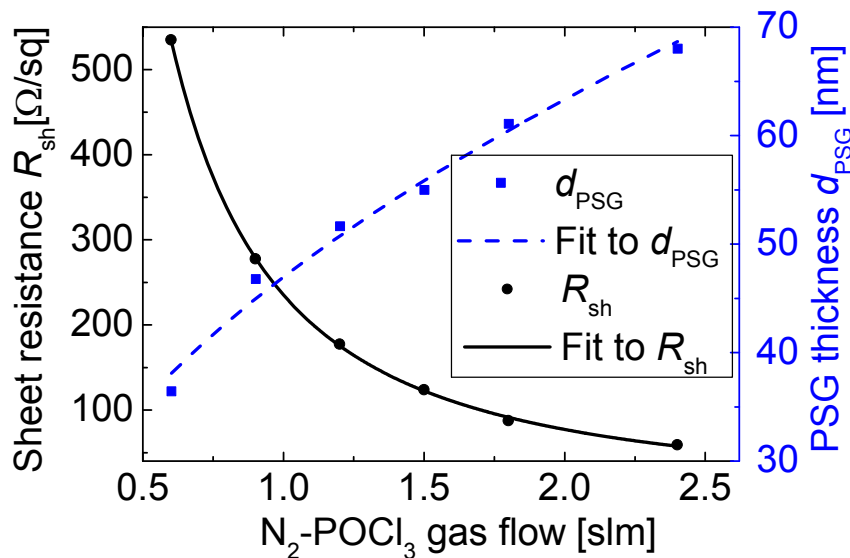


Figure 12: Sheet resistance R_{sh} and thickness of phosphosilicateglass (PSG) layer d_{PSG} over N₂-POCl₃ gas flow Q_{POCl_3} for high temperature process featuring one deposition phase (Figure 9). Both d_{PSG} and Q_{POCl_3} are measured in the center of one wafer. The Fit to R_{sh} is presented equation (3.1), while d_{PSG} is presented in equation (3.2).

Local inductive measurements of the sheet resistance in the center of the wafer and the corresponding local thickness of the PSG layer are plotted over the N₂-POCl₃ gas flow. An

increase in the N_2 - $POCl_3$ gas flow increases the $POCl_3$ concentration in the process atmosphere and results both in an increasing PSG layer thickness and a decreasing sheet resistance. The increasing PSG layer thickness correlates with a slight increase in the phosphorus concentration of the PSG and results in an increased total phosphorus dose in the PSG layer [39]. Thus qualitatively a decrease of $POCl_3$ concentration in the process atmosphere explains both the increase in R_{sh} and the decrease in d_{PSG} towards the center of the wafer. Now the question remains in how far a decrease of the $POCl_3$ concentration in the process atmosphere explains the trend in the sheet resistance quantitatively.

Discussion

Both R_{sh} and d_{PSG} in Figure 12 are linked by the N_2 - $POCl_3$ gas flow Q_{POCl_3} . Thus by fitting the data presented in Figure 12 the sheet resistance may be calculated from a given PSG layer thickness.

The dependence of the sheet resistance in the wafer center from the N_2 - $POCl_3$ gas flow is fitted empirically. The errors represent the errors of the fitting procedure.

$$R_{sh} = (235 \pm 1) \Omega / sq \cdot Q_{POCl_3}^{-1.61 \pm 0.01} \text{ min} / sl . \quad (3.1)$$

The relation between PSG layer thickness d_{PSG} and Q_{POCl_3} is approximated by a square root relation describing the PSG growth due to the change in N_2 - $POCl_3$ gas flow [70] and a constant term that accounts for the influence of the in-situ oxidation step. Again the errors represent the errors of the fitting procedure.

$$d_{PSG} = (39.5 \pm 2.3) \text{ nm} \cdot \sqrt{(Q_{POCl_3} \text{ min} / sl)} + (7 \pm 3) \text{ nm} . \quad (3.2)$$

Figure 13 compares the measured sheet resistance (a) with the calculated sheet resistance (b). The sheet resistance is calculated using the measured PSG layer thickness (Figure 11 b) as an input parameter to calculate a "local Q_{POCl_3} " based on equation (3.2) and then use this as an input parameter to calculate a local sheet resistance according to equation (3.1). Please note that sheet resistance values smaller than $45 \Omega/sq$ result from an extrapolation of the experimental data.

Calculated and experimentally determined sheet resistances in Figure 13 agree within an error margin of 10 - 20 %. This leads to the conclusion that the decrease in $POCl_3$ concentration towards the center of the wafer is the dominant mechanism for inhomogeneity in the doping process. Possible reasons that explain the above deviation of

the simulated from the experimental data are manifold. To name only a few: While the measurement area for the determination of the PSG layer thickness is circular with a diameter of around 1 mm, the sheet resistance is measured inductively in a circular area with a diameter of 25 mm. Since the surface of the wafers is not perfectly planar, but damaged etched, the PSG layers may only be measured using a monochromatic laser ellipsometer, since the signal detected by the spectral ellipsometer is below the detection limit of the setup. This does not allow the determination the refractive index directly and accordingly requires the assumption of a constant refractive index. Furthermore the sheet resistance map in Figure 13 b) is measured by 4-point measurement, while simulations are based on inductive measurements of the sheet resistance (Figure 12).

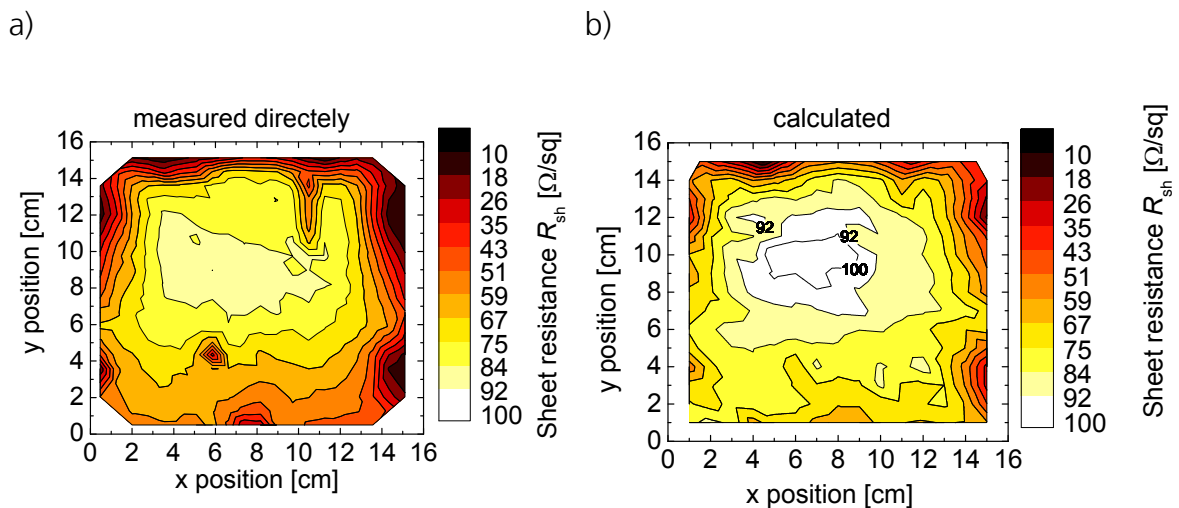


Figure 13: a) Measured sheet resistance determined by 4 point probe measurement
 b) Calculated sheet resistance using the measured PSG layer thickness (Figure 11 b) and equations (3.1) and (3.2).

The use of different detection methods is due to the fact that 4 point measurements exhibit a larger error in the absolute sheet resistance compared to inductive measurements, but their spatial resolution of 4 point probe measurements is higher [66]. As a last point the sheet resistance values smaller than 45 Ω/sq result from an extrapolation of the experimental data, which adds an uncertainty to the parameterization.

An illustration of the assumed underlying chemical reactions is presented in Figure 14.

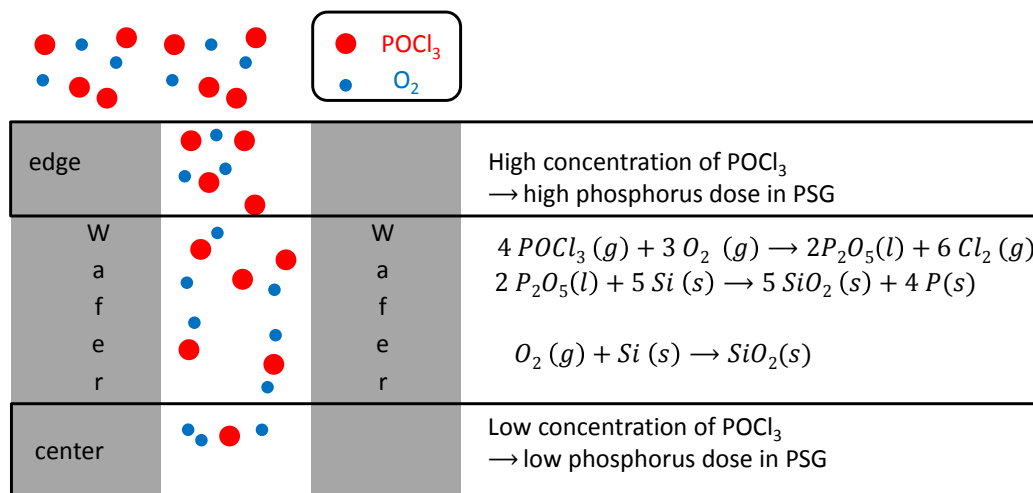


Figure 14: Simplified model for inhomogeneous sheet resistance and PSG layer growth in $POCl_3$ based diffusion processes.

The concentration of $POCl_3$ (red large circles) is highest in the process atmosphere at the wafer edge and decreases towards the center of the wafer. This decreases the dose of phosphorus deposited on the wafer by decreasing P_2O_5 formation according to equation (1.5) and thus also the amount of phosphorus diffusing into the wafer. Since the concentration of oxygen is not reduced equally, a decrease in phosphorus concentration in the PSG layer as observed also by other authors [79] is expected. This theory is consistent with observations that the sheet resistance on textured surfaces is higher than or equal to those on planar surfaces (Figure 47). Based on this view different possibilities for increasing doping homogeneity follow:

One option is a decrease in the ratio between reacting $POCl_3$ molecules and total $POCl_3$ molecules. This may e.g. be achieved by increasing the $POCl_3$ concentration until the reaction $4 POCl_3 + 3 O_2 \rightarrow 2 P_2O_5 + 6 Cl_2$ is saturated. Another possibility is to decrease the probability for the reaction between $POCl_3$ and O_2 by e.g. decreasing process temperature during deposition.

3.2.4 Low concentration PSG sources

An alternative to in-situ oxidation for achieving adequate phosphorus doping profiles is to decrease the dose of phosphorus deposited on the wafer. One possibility to do so is to reduce Q_{POCl_3} . The results in Section 3.2.3 indicate that the sole reduction of Q_{POCl_3} will considerably decrease the homogeneity of the doping over the wafer. For this reason here a twofold approach is adapted. A reduction of Q_{POCl_3} below 0.6 slm as was used in Section 3.2.2 in order to decrease the phosphorus dose and a simultaneous increase in the N_2

gas flow to further reduce the POCl₃ concentration in the process atmosphere. The following questions are investigated: Is it possible to achieve adequate doping profiles, which means in this case surface concentrations around $3 \times 10^{20} \text{ cm}^{-3}$ and how is it possible to manipulate the

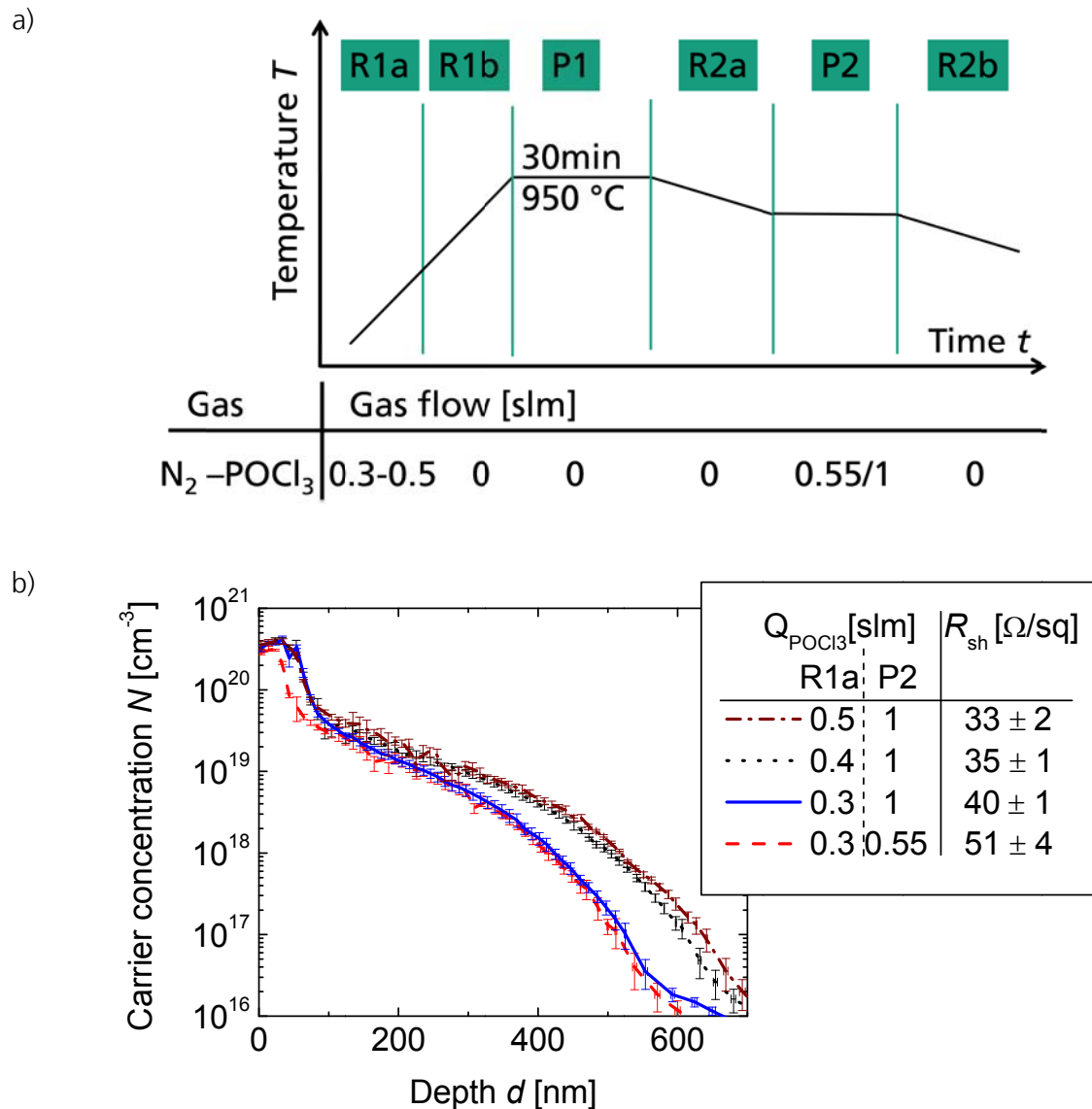


Figure 15: a) Sketch of the high temperature processes featuring lowly doped PSG sources and two deposition phases. b) Carrier concentration over depth resulting from high temperature processes depicted in a) measured by ECV. The error bars represent the measurement accuracy of a single ECV measurement. The different high temperature processes are denominated by the N₂-POCl₃ gas flow Q_{POCl_3} during first (R1a) and second (P2) deposition phase and their averaged sheet resistance R_{sh} with the average standard deviation over one wafer, which are both averaged over 3 wafers.

doping profile in a controlled manner? With regard to the application to solar cells it is advantageous to find a way of manipulating the phosphorus doping profile independently from the boron doping profile, because this facilitates linking changes in the cell behavior directly to one specific property of the phosphorus doping profile (Chapter 4). This means in particular that both temperature and duration of the process, which are relevant for boron diffusion must remain unchanged. Figure 15 a) shows a schematic of the adapted high temperature process.

During the deposition phase (R1a) a PSG layer grows at the wafer surface. In contrast to the high temperature process featuring in-situ oxidation, the oxygen concentration in the process atmosphere during the remaining process stays below 10%. Please note that the O_2 and N_2 gas flows are constant for all high temperature processes depicted in Figure 15 a). During the second plateau (P2) $POCl_3$ is supplied to the process atmosphere a second time. The second plateau is introduced with the aim to increase the degrees of freedom and gain more control over the doping profile.

The influence of Q_{POCl_3} during the two deposition steps (R1a, P2) on the doping profiles is depicted in Figure 15 b). Each doping profile is named with Q_{POCl_3} during the first (R1a) and second deposition phase and the averaged sheet resistance over a planar 156 mm wafer. The three doping profiles featuring $Q_{POCl_3,P2}=1$ slm during the second deposition phase show the same surface near doping concentration, while the high temperature process with $Q_{POCl_3,P2}=0.55$ slm in the second deposition phase exhibits a lower surface near doping concentration and a shorter plateau length of constant carrier concentration. For depths larger than 120 nm the two doping profiles featuring $Q_{POCl_3,R1a} = 0.3$ slm in the first deposition phase are identical within the margin of error, whereas the doping profiles resulting from higher $Q_{POCl_3,R1a}$ in the first deposition phase exhibit a higher doping concentration for depths larger than 120 nm. Thus an increase in $Q_{POCl_3,R1a}$ correlates with an increase in the doping concentration for depths larger than 120 nm, while an increase in $Q_{POCl_3,P2}$ during the second deposition phase correlates with an increase in the surface near doping concentration and an increase in the plateau length of constant carrier concentration at the wafer surface, as was also observed for the high temperature processes featuring in-situ oxidation (Figure 10). This enables the manipulation of phosphorus doping profiles resulting from $POCl_3$ based high temperature processes with unprecedented degrees of freedom. The surface concentration is in the range of 10^{20} cm^{-3} which makes these processes applicable for cell concepts with screen printed metallization. As far as application in solar cells is concerned a relative standard deviation of the sheet resistance over one wafer below

10 % (determined by inductive measurements) is generally considered acceptable for the application in solar cells.

In summary: The use of lowly concentrated PSG sources allows for reaching a wide range of phosphorus doping profiles at temperatures that are suitable for boron co-diffusion. By introduction of a second deposition phase the surface near doping concentration may be adjusted without changing the depth of the doping profile which will allow for systematic investigations of the influence of surface doping concentration on e.g. recombination and contact resistance (Chapters 4 and 5).

After discussing phosphorus diffusion processes the following section treats the other part of the co-diffusion process, namely boron diffusion.

3.3 Influence of oxygen concentration on boron diffusion

It has been shown that boron diffusion from a borosilicate glass (BSG) layer deposited by plasma enhanced chemical vapor deposition (PECVD) at a temperature plateau of 950°C with a duration of 30 min results in a boron doping profile with a surface concentration of around $5 \times 10^{19} \text{ cm}^{-3}$ and a depth around 600 nm [81]. The atmosphere under investigation consisted of nitrogen with a small fraction of oxygen. These findings are taken as a starting point for the development of an industrially feasible co-diffusion process.

In this work layers deposited by atmospheric pressure chemical vapor deposition (APCVD) are investigated. In contrast to PECVD, atmospheric pressure CVD does not require vacuum formation, which decreases complexity of the deposition process and might make APCVD in interesting for industrial application. A first question of interest is thus in how far doping profiles resulting from APCVD layers are comparable to those resulting from PECVD layers. The second point of interest is how the gaseous atmosphere during the high temperature process influences the doping profile. The aim is to find parameters that allow for the manipulation of the boron doping profiles without affecting the phosphorus doping profile.

A third issue is reaching surface concentrations that allow for contact formation by screen printing (around $5 \times 10^{19} \text{ cm}^{-3}$) and at the same time prevent the presence of a boron rich layer (BRL). Very little investigations of the optimum emitter doping profile have been published [82, 83]. It is reported that a BRL hinders effective surface passivation [34]. Benick et al. [84] present efficiencies for n-type PERL solar cells for two different boron emitters. Their findings are that in interplay with plated emitter metallization the doping profile with a surface doping concentration below 10^{19} cm^{-3} and a depth greater than 1 μm allows for higher

efficiencies than an emitter with a surface concentration around 10^{20}cm^{-3} and a depth around 300 nm. The main reason is a higher open circuit voltage for the lowly doped emitter due to a decrease in recombination. As far as solar cells with screen printed metallization of the boron emitter are concerned the exact optimum boron emitter doping profile is not known, yet [85]. So as a last point it is investigated by which means the doping profile may be manipulated and how a change in the doping profile influences properties of bifacial solar cells featuring screen printed metallization.

3.3.1 Manipulation of boron doping profiles

As an introduction into boron diffusion from solid sources, this section presents different possibilities for manipulating the boron doping profile. The corresponding physical mechanisms and the relevance for solar cells are then discussed in the following sections. The experiment is depicted in Figure 16 .

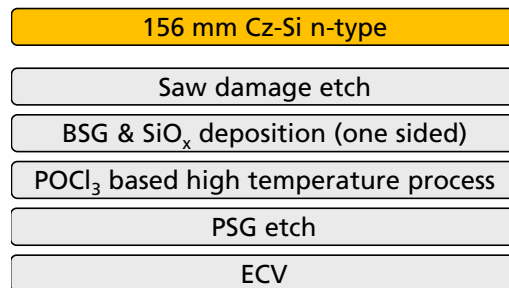


Figure 16: Schematic representation of experiments performed in Section 3.3.1

Layer stacks consisting of one BSG and one SiO_x capping layer on top are deposited on planar Cz silicon wafers with an edge length of 156 nm by APCVD. The SiO_x layer features a thickness of (211 ± 7) nm and a refractive index at a wavelength of 632 nm of 1.443 ± 0.001 for all depositions. The BSG layer either feature a thickness of (75 ± 7) nm and a refractive index of 1.464 ± 0.002 "highly doped" or of (65 ± 7) nm and a refractive index of 1.470 ± 0.001 "lowly doped". The given errors represent the error of the ellipsometric measurement. For the deposition of the "highly doped" BSG layer the B₂H₆ concentration during deposition is increased by a factor of two. These wafers are then subjected to different high temperature processes, which are described below.

- The process "low O₂" consists of one high temperature step with a temperature plateau at 950°C for 30 minutes in an atmosphere containing mainly nitrogen and a low concentration of oxygen.

- The process “post ox.” comprises two high temperature processes: First wafers are subjected to the process “low O₂” then the wafers are stripped from the APCVD layers in an HF-based solution and finally subjected to an oxidation step with a plateau at 840°C that lasts for 5 min and results in the growth of a thermal oxide layer with a thickness of 5-10 nm.
- During the process “in-situ ox” the concentration of oxygen in the process atmosphere is increased compared to the process “low O₂”. The evolution of the temperature is similar to the process “low O₂”, but with the addition of a plateau of constant temperature during ramp down (Figure 15 a).

After the high temperature process the dielectric layers are removed in an HF based solution, a so called “PSG etch”. ECV measurements are then performed on the side of the wafer that was previously covered by the BSG/SiO_x layer stack. The resulting doping profiles are depicted in Figure 17.

Results

The highly doped BSG layer in combination with the high temperature process “low O₂” (Figure 17) results in a carrier concentration of $5 \times 10^{20} \text{ cm}^{-3}$ at a depth of 3 nm. The second data point at 25 nm exhibits a carrier concentration of 10^{20} cm^{-3} . The doping concentration then decreases further until reaching a concentration of 10^{17} cm^{-3} at a depth of approximately 480 nm. Using the same high temperature process but a boron source that was deposited using a lower gas flow of diborane (“low dop., low O₂”) results in a doping profile with a surface concentration of $1.3 \times 10^{20} \text{ cm}^{-3}$ that decreases to $7 \times 10^{19} \text{ cm}^{-3}$ within 7 nm and reaches a concentration of 10^{17} cm^{-3} at a depth of 525 nm. Thus in this case decreasing the diborane gas flow during BSG deposition, results in a reduction of the surface concentration, while the depth of the doping profile is increased. For both BSG layers the measured surface concentration is above the solubility of boron in silicon. Since to the author’s knowledge no such effect has been observed for ECV measurements of boron doped silicon before the results will be discussed further in Section 3.3.2.

A reduction of the surface concentration is caused by both post and in-situ oxidation. While the process “post-ox” leads to a decrease of doping concentration towards the wafer surface by a factor of 4 compared to the maximum doping concentration, the doping concentration resulting from the processes “in-situ Ox” drops by less than a factor of 2. This so called “surface depletion” after oxidation is well known from literature [76]. Surface depletion is caused by the formation of a SiO₂ layer at the silicon surface and a subsequent diffusion of boron from the silicon wafer into the SiO₂ layer due to the high solubility of boron in SiO₂. The possibility of reaching a relatively flat doping profile by continuous in-situ oxidation is to the author’s knowledge less well known, though. The next section provides a microscopic picture for the effects observed in this section.

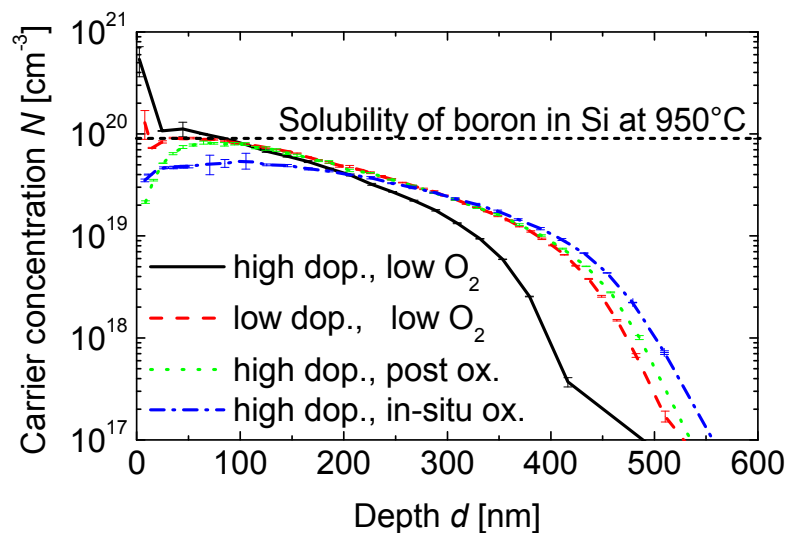


Figure 17: Carrier concentration over depth for diffusion from BSG/SiO_x layer stacks (“high doping” and “low doping”) deposited by APCVD and different high temperature processes (“low O₂”, “post ox.”, “in-situ ox.”) measured by ECV [86]. The error bars represent the measurement accuracy of a single ECV measurement. Solubility of boron in Si taken from reference [29].

3.3.2 Carrier concentration above solubility of boron in silicon

This section discusses the doping profiles presented in Figure 17 with regard to the carrier concentration above solubility of boron in silicon.

The observed carrier concentration is, based on the author’s understanding, physically impossible, when assuming it to result from boron doped silicon. Since ionized boron in silicon contributes one electron to the conduction band even under the assumption of

complete ionization the carrier concentration cannot exceed the doping concentration. Thus it is of interest if the measured data is caused by a measurement artefact or by a physical property of the sample.

An important point for clarification is if the measured carrier concentration is consistent with other measurement methods. To this end the sheet resistance is calculated from the measured carrier concentration profile and then compared to inductive measurements of the sheet resistance.

The carrier concentration is linked to the sheet resistance by

$$R_{sh} = \frac{1}{e \int_0^d N(x) * \mu(N) dx}, \quad (3.3)$$

with the elementary charge e , the carrier concentration N , the mobility μ , which depends on carrier concentration and type, and the depth of the doping profile d . Using the parameterization of $\mu(N)$ for boron doped silicon from references [87,88], the sheet resistance corresponding to the doping profile may be calculated. Please note this implies the assumption that the mobility is that of holes in silicon, even for the data point above solid solubility.

$R_{sh\ sim}$ is calculated from the doping profiles presented in Figure 17 using equation (3.3). For the calculation of $R_{sh\ sim\ solubility}$ all measured carrier concentrations above solid solubility are reduced to $9 \times 10^{19} \text{ cm}^{-3}$. $R_{sh\ measured}$ is determined experimentally by inductive measurements on planar surfaces before the removal of the BSG/SiO_x layer stack on symmetrically processed samples. These values are depicted in Table 3.

Table 3: Comparison of simulated $R_{sh\ sim}$ (equation (3.2)) and measured sheet resistance $R_{sh\ measured}$ (wafer center) for doping profiles presented in Figure 17. Errors for experimental values are estimated to be 2.5 % relative [66] . Errors for simulated values result from the uncertainty of the ECV measurement. Simulated values are printed in bold. For the calculation of $R_{sh\ sim, solubility}$ the values of the doping concentration above solubility of boron in silicon are reduced to $9 \times 10^{19} \text{ cm}^{-3}$.

Doping profile	$R_{sh\ measured}$ [Ω/sq]	$R_{sh\ sim}$ [Ω/sq]	$R_{sh\ sim, solubility}$ [Ω/sq]
High dop. low O_2	52 ± 1	54 ± 3	65
Low dop. low O_2	62 ± 1	58 ± 1	59
High dop. post ox.	70 ± 1	73 ± 1	

With respect to the doping profile “High dop. post ox”, experimentally determined and calculated values deviate by 3 % relatively. For the doping profile “High dop. low O_2 ” including the contribution from the carrier concentration above solubility $R_{sh\ measured}$ and $R_{sh\ sim}$ agree. Neglecting the contribution from the carrier concentration above solubility ($R_{sh\ sim\ solubility}$) leads to a difference between calculated and measured values of 25 %. With regard to the doping profile “low dop. low O_2 ” the difference between $R_{sh\ sim}$ and $R_{sh\ sim\ solubility}$ lies within the margin of error caused by the accuracy of the ECV measurement.

Thus, the best agreement between simulated and experimentally obtained sheet resistance values is reached, for the doping profiles with the measured carrier concentration above solubility of boron in silicon. This is an indication that the detected value is not a measurement artefact.

In order to find an explanation for this effect, the wafers are investigated concerning hydrophilic behavior. It is found that wafers with a surface doping concentration above solid solubility show hydrophilic behavior while wafers with a surface doping below solid solubility show hydrophobic behavior.

In order to increase statistics planar wafers are subjected to two BBr_3 based high temperature processes that result in a wafer surface that is partially hydrophilic and partially hydrophobic (Figure 18 a). The resulting doping profiles are depicted in Figure 18 b). Again a hydrophilic surface correlates with a surface concentration above solubility of boron in silicon, while a hydrophobic surface correlates with a surface concentration below solubility. Since the measurement of carrier concentrations above solubility of boron doped silicon by ECV seems

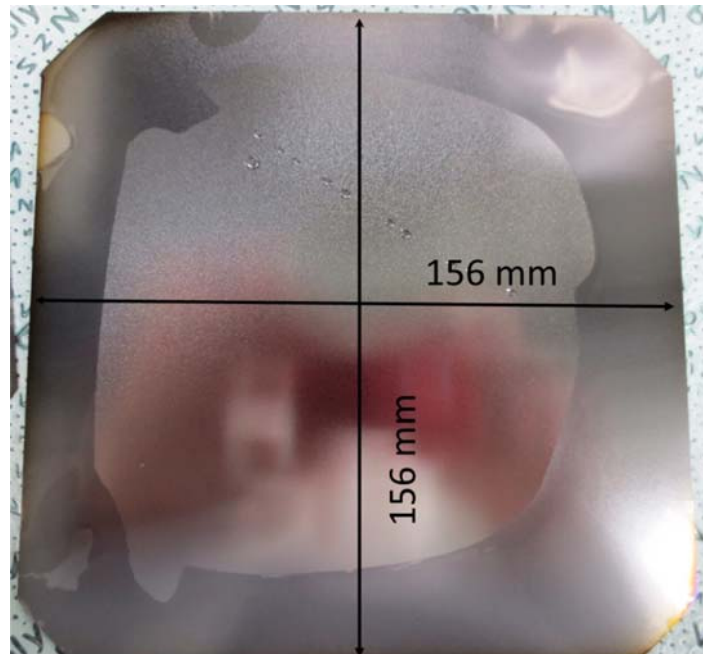
both recurring and relevant for conductivity, the next section presents a possible explanation for this effect.

3.3.3 Discussion of carrier concentration above solubility

From high temperature processes using gaseous [89] and solid sources [90] it is known that increasing the boron concentration in the atmosphere during the deposition of the borosilicate glass layer may lead to the formation of a “boron rich layer” which is also sometimes referred to as “boron skin”. This layer consists of SiB₆ compounds and is known to be hydrophilic [89]. It is also reported that increasing dopant concentration in the process atmosphere during BSG deposition increases BRL thickness, which leads to a decrease in the depth of the doping profile [90]. This could explain the difference in depth between the doping profile “high dop. low O₂” and “low dop low O₂”: The increased flow of diborane during APCVD leads to an increased BRL layer thickness which decreases the depth of the doping profile. A possible reason for the retardation of boron diffusion due to boron rich layer formation is a lower diffusivity of boron in the boron rich layer compared to silicon [35]. This assumption could e.g. be verified by investigating the diffusion of a different impurity that diffuses by the same diffusion mechanism as boron. A second hypothesis is retardation of the diffusion by the injection of point defects as proposed by Kurachi et al. [90]. A BRL is known to be conductive. The effective hole mobility μ_{eff} of a BRL was determined to be $\mu_{\text{eff}} = 43.8 \pm 1.6 \text{ cm}^2/(\text{Vs})$ [89]. Using this value to simulate the sheet resistance of the boron emitter “High dop. low O₂” results in $R_{\text{sh sim}} = 51 \text{ } \Omega/\text{sq}$, which is in agreement with the experimentally determined value of $R_{\text{sh meas}} = (52 \pm 1) \text{ } \Omega/\text{sq}$. Depending on the thickness of the BRL, its presence could be confirmed by cross-sectional REM measurements [33, 91].

In summary: The observation of carrier concentrations above solubility of boron in silicon by ECV may be explained by the formation of a BRL during the diffusion process. This finding is very important for application, since a BRL degrades device performance (Section 1.3). The next section treats the influence of oxygen on boron doping observed in Figure 17.

a)



b)

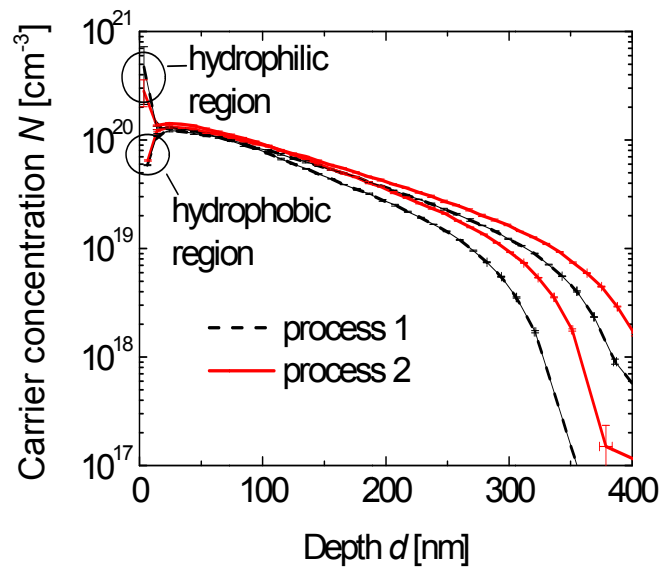


Figure 18: a) Planar Cz-Si wafers with an edge length of 156 mm after BBr_3 based high temperature processes. After removal of the BSG layer in an HF based solution the wafer is soaked in distilled water and then photographed 5 seconds after soaking. b) Doping profiles measured by ECV on hydrophilic and hydrophobic parts of planar wafers for two different BBr_3 based high temperature process. The error bars represent the measurement accuracy of a single ECV measurement.

3.3.4 Influence of oxygen concentration in process atmosphere on boron doping profile

This section briefly discusses the microscopic mechanisms behind the influence of the oxygen concentration in the process atmosphere on the boron doping profiles that were presented in Figure 17. The first part of this section deals with “post oxidation” while the second part treats “in-situ oxidation”.

The mechanism of boron depletion after post-oxidation has been observed many times before [76, 92]. The concept is as follows: Oxygen in the atmosphere reacts with the silicon at the wafer surface and forms a SiO₂ layer. The solubility of boron in this SiO₂ layer is larger than in silicon. Thus if boron is already diffused into the wafer, during SiO₂ formation some surface boron diffuses out of the wafer into the SiO₂ layer.

A second mechanism is based on the fact that the silicon needed for SiO₂ formation is taken from the bulk, which removes the amount of doped bulk material. Since the density of bulk silicon and SiO₂ is similar, as a rough estimation a bulk Si layer with a thickness of around half the layer thickness of the SiO₂ layer is converted into SiO₂. Before ECV measurements this oxide layer at the surface is removed in an HF based solution. Since the thickness of the SiO₂ layers grown on boron doped surfaces in this thesis is ≤ 10 nm, this effect roughly concerns the first 5 nm of the doping profile. Thus the extent of this effect is small in comparison to the depletion of the surface concentration which extends until a depth of around 80 nm. Concerning the loss in carrier concentration the effect of depletion is larger by a factor of around 4 compared to the loss introduced by conversion of bulk silicon into a silicon oxide layer.

The third mechanism concerns BRL formation. It is reported that a boron rich layer which is exposed to an atmosphere containing oxygen is converted into a silicon-oxide layer [93]. Since silicon-oxide layers are removed before ECV measurements, no BRL will be detected in the ECV measurement.

Based on the mechanisms described above the author proposes the following model for in-situ oxidation. During in-situ oxidation, oxygen diffuses through the dielectric layers towards the wafer surface, where a SiO₂ layer grows. This layer decreases the amount of boron diffusing into the wafer because of the difference in solubility of boron in SiO₂ and silicon. Since the SiO₂ layer is present at the wafer surface during the whole diffusion process, the conditions at the interface stay constant and no “depletion” takes place. Since the surface concentration of boron is reduced compared to an atmosphere without oxygen, the growth of the SiO₂ layer may prevent BRL formation. The constant growth of a SiO₂ layer at the wafer surface, constantly create silicon self-interstitials which enhances boron diffusion.

While the above sections characterized the doping profiles, it is not clear, which doping profile is best for application in solar cells. An experimental investigation using solar cells is difficult, since a change in O_2 concentration, will not only affect boron but also phosphorus diffusion [76], which significantly increases complexity of the analysis. Thus concerning the influence of a decrease in doping concentration towards the wafer surface, investigation by simulation is a reasonable alternative.

3.4 Simulation: Influence of surface depletion on cell efficiency

3.4.1 Introduction

In this section the form of the optimum boron doping profile for a solar cell structure featuring a front side boron emitter (Figure 6) is investigated using simulations. Of special interest is if a decrease of the boron concentration towards the surface “depletion” decreases or increases cell efficiency compared to a profile without depletion (Figure 19). The relevant effects are first described qualitatively in order to develop an appropriate approach for a quantitative investigation. Concerning the decrease of boron doping concentration towards the wafer surface multiple different cell parameters may be affected:

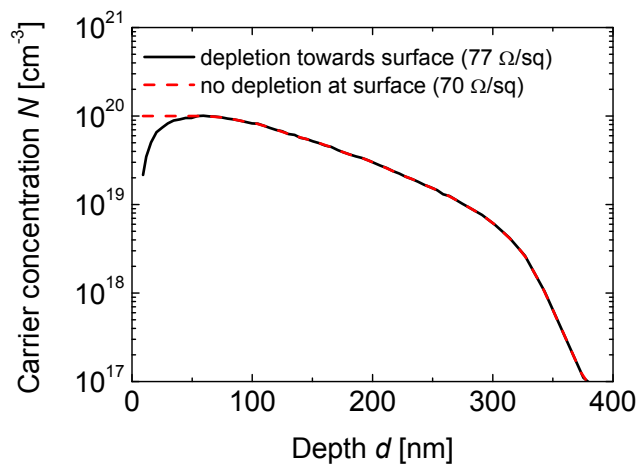


Figure 19: Carrier concentration over depth used as input parameters for simulations concerning the optimum doping profile. Each doping profile is denoted by its sheet resistance.

Changing the doping concentration will change carrier recombination, which influences V_{oc} and J_{sc} . With regard to the influence on V_{oc} and J_{sc} a distinction needs to be made between

metalized (not illuminated, high surface recombination velocity) and unmetalized/passivated (illuminated, low surface recombination velocity) areas. In metalized areas an increase in doping concentration increases shielding of the metal contacts, which may decrease surface recombination. At the same time an increase in doping concentration increases Auger recombination. In passivated areas an increase in surface doping concentration will increase surface recombination, which increases recombination. As for the metalized area the increase in doping concentration leads to an increase in Auger recombination. Concerning recombination and the corresponding cell parameter V_{oc} , it is not clear if a depleted boron doping profile increases or decreases cell efficiency compared to the identical doping profile without surface depletion.

Apart from recombination, as a second point resistive losses need to be taken into account. Here the picture is very clear. A decrease in surface concentration will increase (specific) contact resistance [94] and also decrease lateral conductivity, which both increases resistive losses and decreases solar cell efficiency. Since the quantification of this influence on e.g. contact resistance is very difficult, the influence of surface depletion on series resistance is neglected in a first step. Based on the considerations from above the following approach is chosen:

3.4.2 Approach

The simulations in this section are based on software tool EDNA version 1.2 [95] that is modified in order to allow for a local reduction of the bulk lifetime. Two doping profiles (Figure 19) are used as input parameters for calculating the collected current $J_{collect}$ in the emitter and the recombination characterized by J_0 for the metallized and unmetallized areas. The doping profile "depletion towards surface" features a sheet resistance of 77 Ω/sq and is obtained experimentally. For the doping profile "no depletion at surface" the concentration for depths below 60 nm is kept constant at 10^{20} cm^{-3} which results in a sheet resistance of 70 Ω/sq . An additional input parameter is the surface recombination velocity (*SRV*) of the passivated area. Its parameterization is valid for boron doped surfaces passivated by Al₂O₃ deposited by atomic layer deposition (ALD) [96], the passivation technique used in this thesis. The effective *SRV* of the metalized area is set to $2 \times 10^7 \text{ m/s}$ following the parameterization by Green [97]. This is the maximum possible value of the *SRV*, limited by the movement of carriers in the semiconductor and a common approximation for metalized areas. In order to explain experimentally obtained values for the dark saturation current density in the metalized area of 3000 fA/cm² [98], the assumption of additional recombination is necessary. Since the metal contacts are reported to penetrate into the doped silicon [99], the

assumption of a reduced bulk lifetime up to a certain penetration depth seems justified. Since both the penetration depth and the lifetime in the penetrated volume are unknown, different combinations of penetration depth and corresponding lifetime are investigated. Each data pair of depth and lifetime (Figure 19) in combination with the doping profile “depletion towards surface” results in a dark saturation current density in the metalized area of $3 \times 10^3 \text{ fA/cm}^2$ and is thus consistent with experimental data.

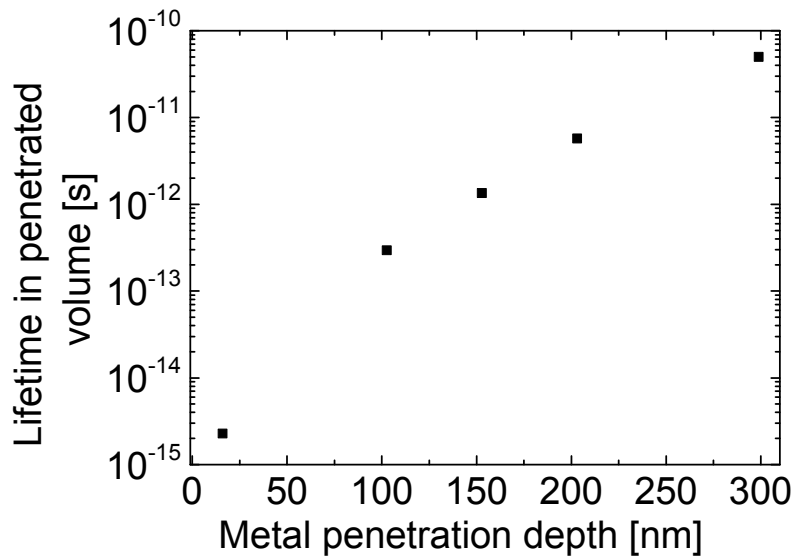


Figure 20: Assumed lifetime in silicon volume penetrated by the metallization over the corresponding penetration depth.

In order to show the relevance for solar cell application not only the dark saturation current densities of the boron emitter, but also the open circuit voltage V_{oc} of a possible solar cell device will be discussed. The conversion from J_0 to V_{oc} is performed as follows. The total value of J_0 for the boron emitter is obtained as the sum of the contributions from the passivated and the metalized part, weighted by their respective area coverage, using a common area coverage of the metallization of 5 %. The textured surface is considered by multiplying the values for J_0 in the passivated area by a factor of 1.7, which corresponds to the surface enlargement of a textured surface compared to a planar surface. The open circuit voltage of the solar cell is calculated [100] assuming additional recombination of 195.7 fA/cm^2 in the remaining parts of the solar cell, which results in common open circuit voltages around 650 mV [85,98]. In accordance with experimental data (Table 6), the total collected current in base and emitter is set to 39 mA/cm^2 . As is common for the experimental determination of dark saturation current densities further constant input parameters are a base doping

concentration of 10^{15} cm^{-3} and a bulk lifetime limitation due to Shockley-Read-Hall recombination of 1 ms. A schematic representation of the approach is depicted in Figure 21.

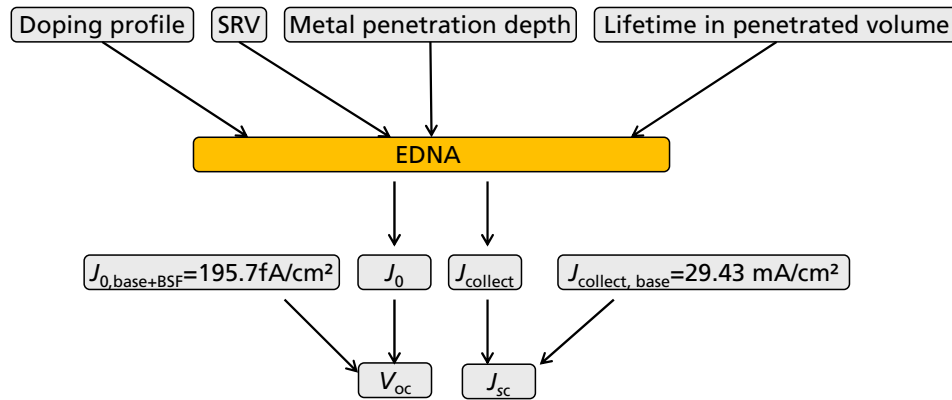


Figure 21: Schematics of input and output parameters used to investigate the influence of surface depletion on current voltage characteristics of a solar cell device.

3.4.3 Results

This section investigates the influence of surface depletion on solar cells with a full area boron emitter featuring screen printed metallization. First the dark saturation current densities and the short circuit current density are presented. Then, following the approach presented in Section 3.4.2., the effects on solar cell efficiency are shown.

Table 4: Calculated dark saturation current density J_0 and collected photocurrent J_{collect} for two boron doping profiles and their respective surface recombination velocity (SRV). The doping profile “no depletion” corresponds to the dashed curve in Figure 19 while “depletion” corresponds to the solid line. Calculated results are printed in bold.

doping profile	SRV [cm/s]	J_0 [fA/cm ²]	J_{collect} [mA/cm ²]
“no depletion”	2208	63	9.66
“depletion”	515	57	9.67

As expected from the qualitative considerations in Section 3.4.1, the value of J_0 is lower and J_{collect} is higher for the doping profile “depletion” compared to the profile “no depletion” (Table 4). A decrease in J_0 and an increase in J_{collect} increase cell efficiency, thus concerning recombination in the passivated area and current collection, the doping profile “depletion” is better suited for application in solar cell. Since about 5 % of a solar cells front side are

metalized, it is important to include the contribution from metalized parts of the boron emitter (Figure 22). The dark saturation current density in the metalized part J_{0met} resulting from the “depleted” doping profile is independent from the metal penetration depth, in accordance with the assumptions presented in Section 3.4.2. The value of J_{0met} resulting from the “non depleted” boron doping profile increases from $J_{0met} = 2100 \text{ fA/cm}^2$ to 2900 fA/cm^2 for an increase in the metal penetration depth from 6 nm to 300 nm. The difference in J_{0met} between the “non depleted” and the “depleted” boron doping profiles decreases for increasing metal penetration depth.

Since J_{0met} is not directly measurable it is of high interest how the changes in J_{0met} influence measurable quantities such as the open circuit voltage V_{oc} .

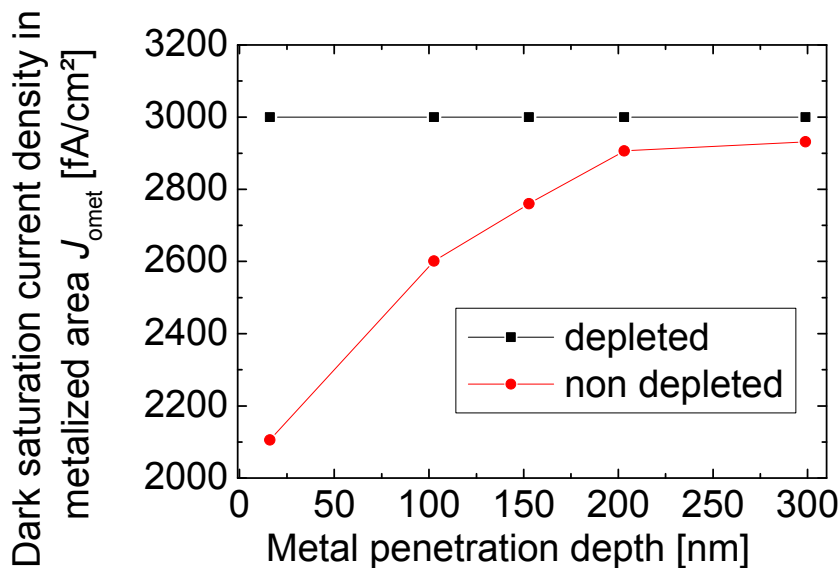


Figure 22: Calculated dark saturation current density in the metalized area J_{0met} over metal penetration depth for “depleted” and “non depleted” boron doping profile (Figure 19).

The open circuit voltage V_{oc} for a solar cell featuring a “depleted” and “non depleted” doping profile (Figure 19) as a function of metal penetration depth is displayed in Figure 23.

Due the approach presented in Section 3.4.2, the “depleted” doping profile results in a constant V_{oc} of 650.1 mV. Following the trend in J_{0met} the V_{oc} resulting from the “non depleted” doping profile decreases with increasing metal penetration depth from 652.8 to 650.0 mV. For metal penetration depths smaller than 200 nm the “non depleted” doping profile allows for a higher V_{oc} , while for larger depths the “depleted” profile results in a marginally higher V_{oc} . With respect to solar cells it is interesting which doping profile allows for the highest efficiency, considering both the effects on V_{oc} and the short circuit current.

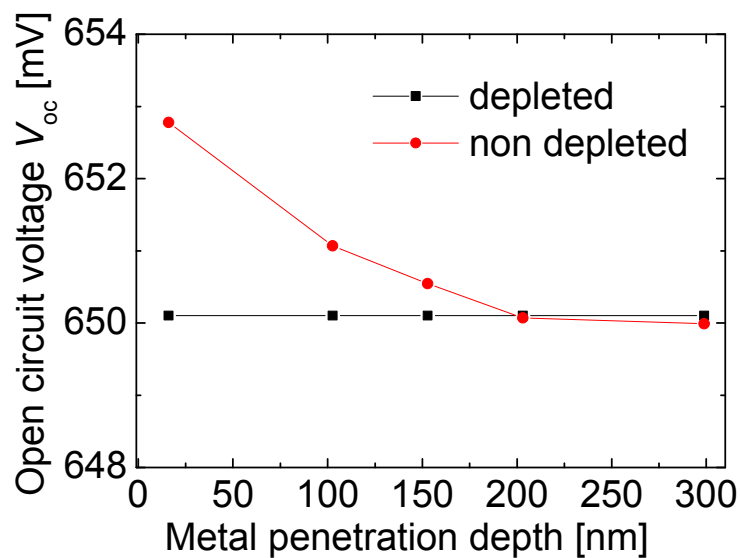


Figure 23: Calculated open circuit voltage V_{oc} for solar cell featuring a “depleted” and “non depleted” boron doping profile (Figure 19) as a function of metal penetration depth.

The relative differences $((X_{nondepleted} - X_{depleted}) / X_{nondepleted})$ for J_{sc} , V_{oc} and efficiency η resulting from the “depleted” and “non depleted” doping profile are depicted in Figure 24. For depths smaller than 180 nm the relative difference in η is positive, which means that the doping profile “no depletion” allows for higher cell efficiencies than the depleted one. Here the increase in V_{oc} overcompensates the decrease in J_{sc} . For depths larger than 180 nm the relative difference in η is negative. Here the magnitude of the relative decrease in J_{sc} is larger than the change in V_{oc} . Thus concerning the effects of surface depletion of the boron doping profile on V_{oc} and J_{sc} the optimum doping profile that allows for maximum efficiency depends on the metal penetration depth.

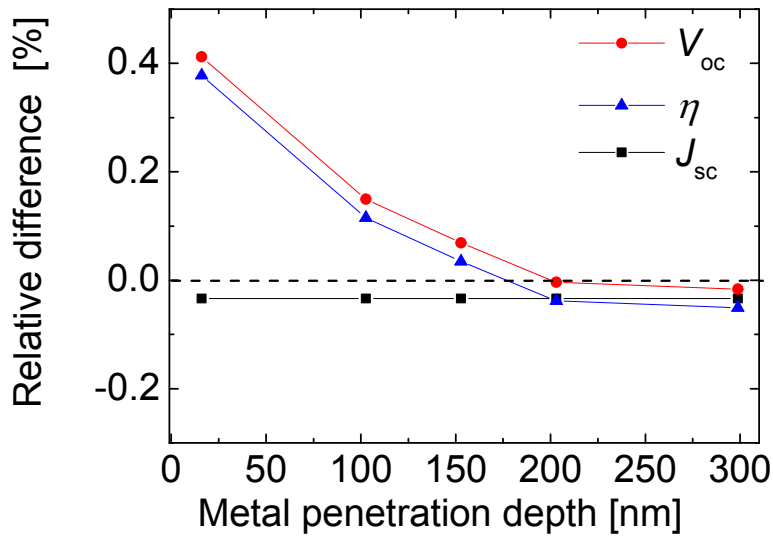


Figure 24: Relative difference in J_{sc} , V_{oc} , and cell efficiency η between “non depleted” and “depleted” doping profile over metal penetration depth.

3.4.4 Discussion

This paragraph shortly discusses the relevance of the results for the solar cells investigated in this thesis. As stated in Section 3.4.2, the approach used in the above section neglects the influence of the doping profile on series resistance and the corresponding IV-parameter FF . Since the doping concentration of the emitter without a depleted surface increases lateral conductivity and decrease specific contact resistance, there will be an additional increase in efficiency. This increase in efficiency is hard to determine quantitatively in the context of this thesis though, since it depends among other things on details of the front side screen printing process. With this additional effect in mind the relative difference in cell efficiency presented in Figure 24 may thus be interpreted as a lower estimate. Since this section predicts changes in the IV parameters, but does not investigate these experimentally, in the following it will be estimated in how far the predicted effects are detectable experimentally.

Regardless of any effects on the fill factor it would be interesting to experimentally investigate the predicted effects in V_{oc} and J_{sc} . According to the specifications of the IV measurements, relative changes in V_{oc} and J_{sc} larger than 0.05 % are measurable. When looking at IV measurements obtained in this thesis (e.g. Section 4.6) measurement accuracy is not limited by the accuracy of the detection method, but rather by the reproducibility of sample preparation. Based on the spread of experimental values in Figure 52 and Figure 53,

100 samples per doping profile lead to a statistical error in J_{sc} of 0.03 % and 10 samples to an error of 0.05 % in V_{oc} . Since a sample number of 10 is typical in a lab environment, depending on the metal penetration depth it might be experimentally possible to observe the predicted changes in V_{oc} . An observation of the predicted changes in J_{sc} requires sample numbers that are too large for a lab environment but are common in pilot line production of photovoltaics companies.

In summary: For application in solar cells the impact of surface depletion of the boron emitter greatly depends on the metal penetration depth of the screen printed metallization. The maximum relative decrease in efficiency for a “depleted” compared to a “non depleted” profile is 0.05 %_{rel}, while the maximum increase in efficiency is larger than 0.4 %_{rel}, which corresponds to an absolute change in efficiency of approximately (0.08 %_{abs}), assuming a cell conversion efficiency of 20 %.

3.5 Experimental and theoretical investigation SiO₂ layer growth at SiO_x/Si interface

In order to understand the impact of the oxygen concentration in the process atmosphere on the boron doping profile (Section 3.3) in more detail the growth of an intermediate SiO₂ layer at the Si/SiO_x interface is investigated experimentally and theoretically. The hypothesis developed in Section 3.3.4 is that during a high temperature step oxygen diffuses through the dielectric layers deposited by APCVD and forms an intermediate SiO₂ layer at the Si/SiO_x interface. In the first part of this section the growth of this layer is investigated experimentally. In the second part an iterative model is developed and then used to calculate the thickness of this oxide layer without the use of free parameters.

This topic was investigated in close collaboration with the diploma student Sebastian Meier. In the following an extract of the results corresponding to contribution of the author of this thesis is presented. For more details especially concerning the experimental part, please refer to Meier [101].

3.5.1 Course of experiment

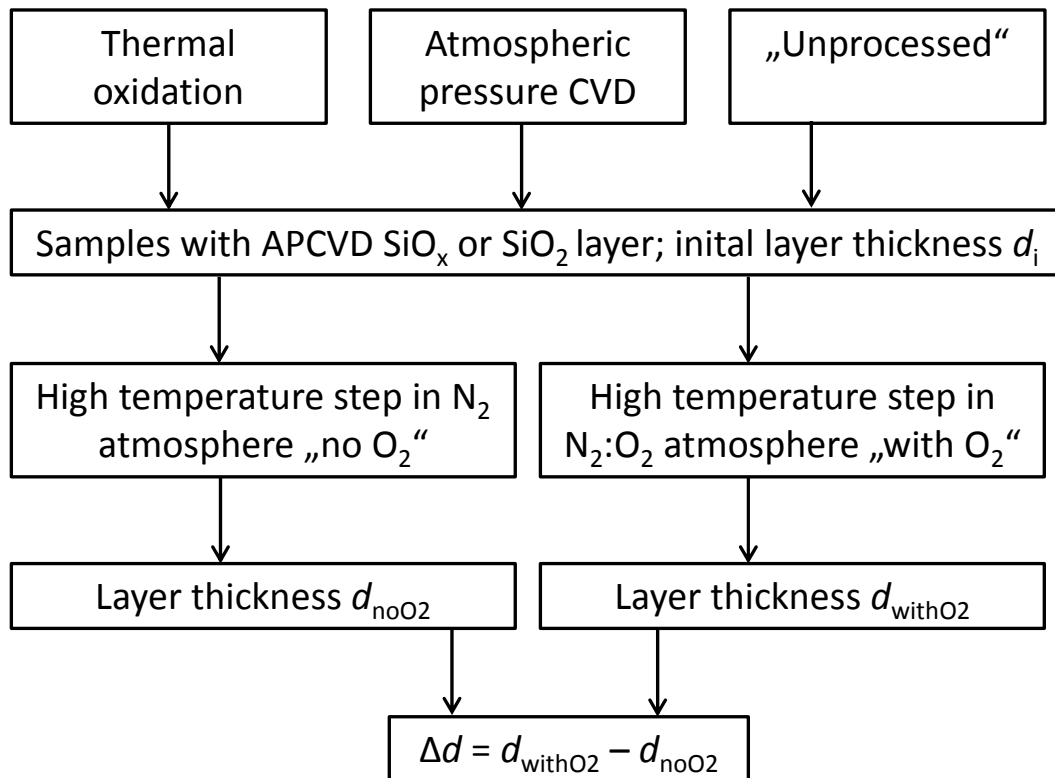


Figure 25: Schematic course of the experiment. A sample with an oxide layer that is either deposited by APCVD or thermally is subjected to two high temperature steps. Both temperature steps feature the same temperature profile but different oxygen concentrations in the process atmosphere. After each process the layer thickness d is extracted. As a final step Δd is calculated as $\Delta d = d_{\text{withO}_2} - d_{\text{noO}_2}$

The experiment is depicted in Figure 25. Shiny etched pseudosquare p-type float zone (FZ) silicon wafers with an edge length of 125 mm and a base resistivity of 1 Ωcm serve as starting material. A first group of wafers are treated by thermal oxidation steps that result in the growth of SiO₂ layers with different initial thicknesses d_i . A second group of wafers is subjected to different APCVD steps for the deposition of SiO_x layers with different initial thicknesses d_i . A third group of wafer remains unprocessed. Please note that for these wafers even without a thermal process a so called “native oxide” grows at the wafer surface due to the oxygen concentration in the ambient atmosphere. Please note that in the following data resulting from these “native oxide” is assigned to the group of “thermal oxide” layers for reasons of simplicity. The layer thicknesses are determined using laser ellipsometry for the SiO₂ layers and spectral ellipsometry for the SiO_x layers deposited by APCVD. In the following this layer thickness will be denoted as initial layer thickness d_i . All samples are then subjected

to a (second) high temperature step in a tube furnace. For each layer type and thickness one half of the wafers are subjected to a high temperature step in an atmosphere containing only N_2 , which is in the following denoted as “no O_2 ”. The second half is exposed to an atmosphere containing a mixture of N_2 and O_2 called “with O_2 ”. A schematic of the temperature time profile as well as the gas flows of the high temperature steps “no O_2 ” and “with O_2 ” is shown in Figure 26. After both high temperature steps the layer thicknesses d_{noO_2} and d_{withO_2} for each layer type and thickness are again determined using ellipsometry. Details of the underlying optical models are described by Meier [101]. The value Δd is now calculated as $\Delta d = d_{withO_2} - d_{noO_2}$.

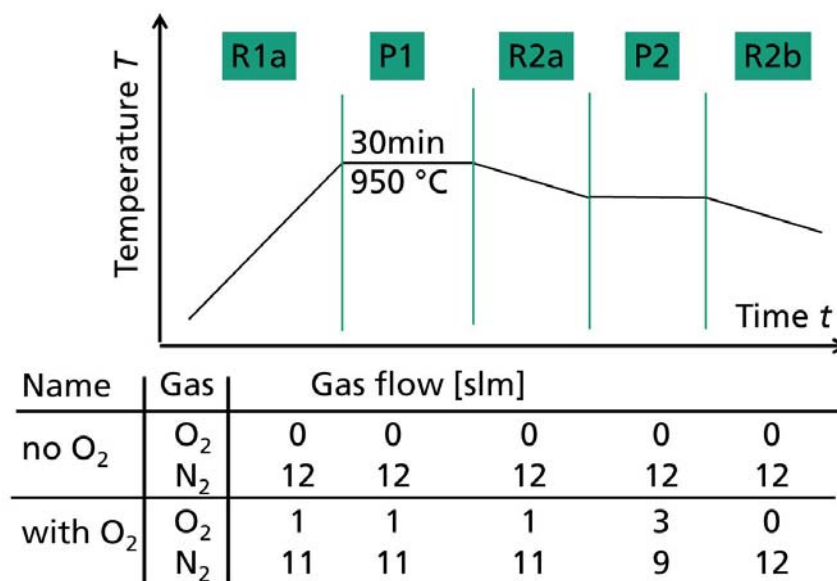


Figure 26: Schematic representation of the high temperature process used for investigating the interaction between oxygen in the process atmosphere and the layers deposited by APCVD.

The course of temperature which is the same for both processes is displayed at the top. After an increase to 950°C the temperature stays constant for 30 minutes. Then the temperature is lowered and the samples are annealed before cooling and unloading. Please note that for reasons of simplicity loading and unloading of the quartz boat are not shown in Figure 26. Both high temperature steps feature a constant total gas flow of 12 slm. For the process “no O_2 ”, this means a constant N_2 gas flow of 12 slm during the whole duration of the process. For the process “with O_2 ” the oxygen concentration is around 8% during most of the process and increases to 25 % during the second plateau of constant temperature “P2”. During the rest of the process (R2b) the oxygen gas flow is set to zero.

3.5.2 Results

Figure 27 shows the difference in layer thickness Δd after the high temperature steps “with O₂” and “no O₂” as a function of the initial layer thickness d_i . “APCVD SiO_x” denotes data where the initial layer before the (second) high temperature step is SiO_x deposited by APCVD while for “Thermal SiO₂” the initial layer is thermally grown SiO₂.

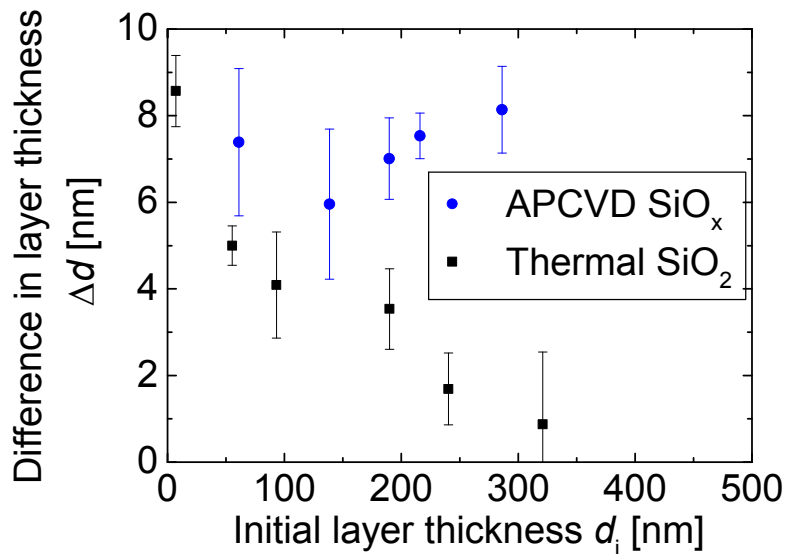


Figure 27: Difference in layer thickness Δd as a function of initial layer thickness d_i , the initial layers being SiO_x deposited by APCVD (round symbols) and thermally grown SiO₂ (square symbols). Error bars represent the standard deviation of the average value obtained from averaging 15-25 measurement points.

The maximum difference in layer thickness Δd is (8.6 ± 0.8) nm, measured for an initial layer thickness of 1 nm (native oxide). As expected for thermal SiO₂, an increase in d_i leads to a decrease in Δd until for $d_i = 320$ nm the minimum of $\Delta d = (0.9 \pm 1.7)$ nm is reached.

The change in layer thickness for the APCVD SiO_x layers shows a different trend. Here the maximum of $\Delta d = (8.1 \pm 1)$ nm is reached for $d_i = 286$ nm. For these layers an increase in d_i does not correspond to a decrease in Δd . Rather Δd fluctuates around a constant value. The minimum values of $\Delta d = (6.0 \pm 1.7)$ nm is situated at $d_i = 139$ nm.

For the APCVD SiO_x layers the thickness measured after the high temperature process “no O₂” is smaller than initial layer thickness, meaning the layer thickness decreases when subjected to a high temperature step in an atmosphere containing only N₂. A detailed discussion is given in reference [101].

In summary: While the absolute values of the maxima of Δd for thermally grown SiO_2 and SiO_x layers deposited by APCVD are the same within measurement accuracy, the position of the maxima, the dependence of Δd from d_i and the minimum values of Δd differ considerably.

3.5.3 Discussion

Since much more literature exists on influence of an oxidizing ambient on thermally grown SiO_2 layers compared to SiO_x layers this section is structured as follows. First Δd based on thermally grown SiO_2 layers is discussed and compared to results in literature in order to verify the validity of the experimental method. Afterwards Δd for SiO_x layers is discussed.

The decrease in Δd with increasing initial layer thickness of the thermally grown SiO_2 layer may be qualitatively explained by the underlying physical mechanism of the oxidation process. The growth of an oxide layer results from the diffusion of an oxidizing species through the already existing SiO_2 layer and the chemical reaction with silicon at the interface between Si and SiO_2 [12]. If the thickness of the thermally grown SiO_2 layer increases the flux of the oxidizing species (F) through this layer decreases according to Fick's law:

$$F = -D_{\text{eff}} (dC / dx), \quad (3.4)$$

with the effective diffusion coefficient D_{eff} and the concentration gradient of the oxidizing species in the oxide dC/dx . This decrease in flux decreases the oxidation rate dL_{DG}/dt :

$$\frac{dL_{\text{DG}}}{dt} = \frac{B}{(2L_{\text{DG}} + A)}, \quad (3.5)$$

where L_{DG} represents the layer thickness calculated according to the model by Deal and Grove and A and B are constant defined in Section 1.5. Thus based on the argumentation presented above the dependence of Δd from d_i for thermally grown SiO_2 layers may be qualitatively described by existing models.

In contrast to this, the dependence of Δd from d_i for SiO_x layers is less obvious. Here the initial layer thickness d_i does not influence Δd significantly, even though the thickness of SiO_x layers is in the same range as that of SiO_2 layers. In the following two hypotheses concerning the reason for the change in layer thickness of the SiO_x layers are discussed.

The, in the author's view, most probable hypothesis is that analogous to thermally grown SiO_2 layers the oxidizing species diffuses through the SiO_x layers with negligible interaction and forms a SiO_2 layer at the SiO_x/Si interface. This hypothesis is supported by data presented

in Figure 17, where the oxygen concentration in the process atmosphere influences diffusion processes in the silicon bulk. If the change in layer thickness is dominated by the formation of an intermediate SiO₂ layer, then the independence of Δd_{SiO_x} from d_i means that within measurement accuracy the APCVD SiO_x layers used in this thesis do not act as a diffusion barrier against the oxidizing species.

A second hypothesis is that the oxidizing species reacts with the SiO_x layer, which leads to an increase of the SiO_x layer thickness and also forms an intermediate SiO₂ layer at the interface. This hypothesis may be confuted based on experimental data [101].

To the author's knowledge this finding is reported for the first time. Furthermore is also extremely relevant for application. Since in some POCl₃ based diffusion processes (compare Section 3.2.2 and 3.2.3) high oxygen concentrations are needed to allow for suitable phosphorus diffusion, these processes might not be compatible with boron diffusion from layers deposited by APCVD. Assuming the diffusion of the oxidizing species through BSG to be similar to SiO_x, the high oxygen concentration will possibly form an intermediate SiO₂ layer at the BSG/silicon interface and decrease the boron concentration below a level that is currently required for suitable contact resistances of screen printed contacts.

An interesting experiment to confirm this hypothesis could be performed using radioactive oxygen isotopes using a similar experimental setup as Rosencher et al. [102].

Due to the high relevance of this topic a quantitative description of the observed experimental data (Figure 29) will be the topic of the next section.

3.5.4 Quantitative description of SiO₂ layer growth at SiO_x/Si interface

This section quantitatively investigates the growth of the intermediate SiO₂ layer at the SiO_x/Si interface in dependence of the process conditions, namely temperature and oxygen concentration. The aim is to reproduce the experimental data and develop a method that allows for predictive modelling of the growth of intermediate SiO₂ layers. Since to the author's knowledge no model for oxygen diffusion through CVD SiO_x layers exists, the theoretical investigation is based on models originally developed for the diffusion of oxygen through thermally grown SiO₂ layers by Deal and Grove [12], Massoud and Plummer [13] and Han and Helms [40]. These models describe the time dependent growth of a SiO₂ layer at a constant temperature in a process atmosphere containing O₂. Since during the high temperature processes under investigation in this thesis oxygen is present in the atmosphere during two plateaus of different temperatures as well during ramp up and ramp down at changing concentrations, these two models need to be adapted to more complex process

conditions. A third model by Han and Helms [40] is also investigated briefly. Unfortunately one of the terms describing the growth of the oxide layer $\frac{dL_{HH}}{dt} = \frac{B_1}{(2L)} + \dots$ diverges for small layer thickness L . As mentioned by Han and Helms [40] the presented parameterization is also only valid for thicknesses above 1 nm, which complicates modelling. Neglecting the contribution of this term for small layer thicknesses, the resulting oxide growth is smaller than the one predicted by the model by Deal and Grove, which makes this model less suited for the application in this thesis. Thus the following approach is chosen:

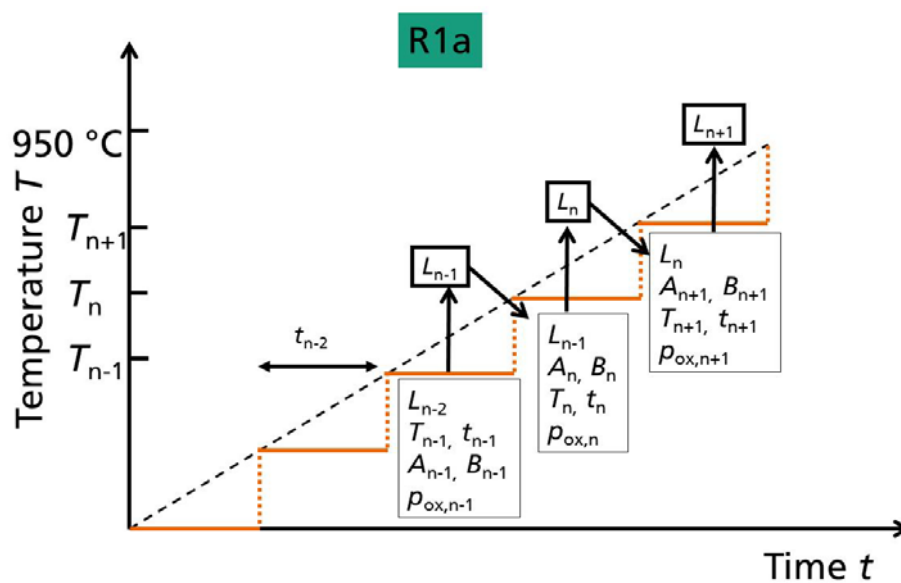


Figure 28: Simplified visualization of the iterative model based on the analytical description by Deal and Grove [12]. The temperature ramp R1a is approximated by $n+1$ intervals each at a constant temperature T_n with a time duration of t_n and a partial pressure of oxygen $p_{ox,n}$. For each interval the parameters A_n and B_n are calculated based on the analytical model by Deal and Grove. Using these parameters and the layer thickness resulting from the previous interval (L_{n-1}) the new layer thickness L_n is calculated.

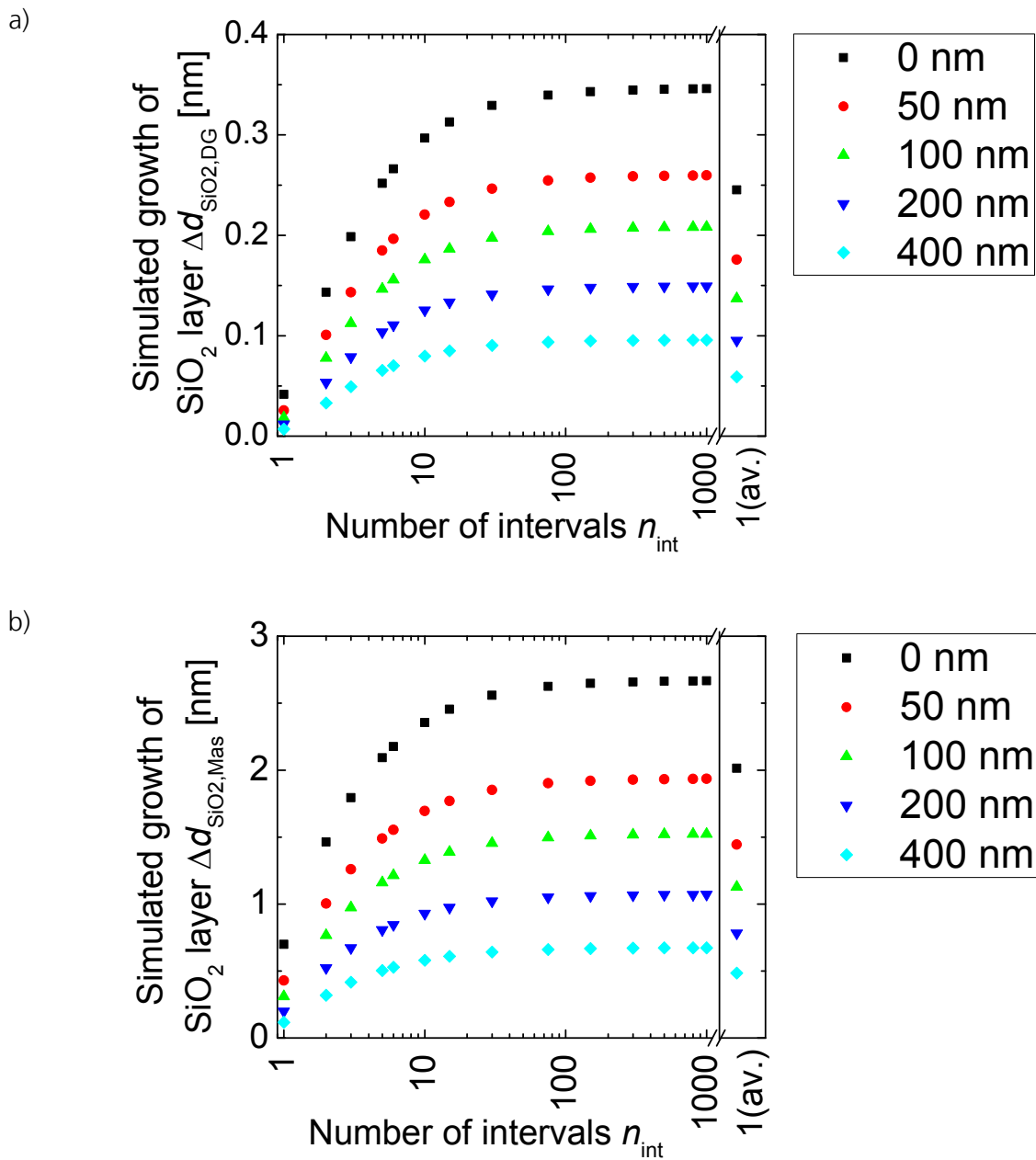


Figure 29: Simulated layer thickness over number of intervals n_{int} for the temperature ramp R1a (Figure 28) for different initial layer thicknesses d_i ranging from 0 to 400 nm using the iterative model. a) is based on the parameterization by Deal and Grove a) and b) on the one by Massoud and Plummer. The data point 1 (av.) denotes the simulated oxide thickness calculated using one interval at the average temperature.

Both the model by Deal and Grove and the one by Massoud and Plummer are first adapted for the description of high temperature processes with oxidation at different (non-constant) temperatures and different oxygen concentrations. The validity of these adapted models is then tested using data concerning the growth of an intermediate SiO₂ layer at the interface

between a thermally grown SiO₂ layer and silicon. As a third step the models are then adapted to describe the growth of an intermediate SiO₂ layer at the interface between SiO_x and silicon. The corresponding source code is attached in Appendix A.

As a first step these models are adapted for oxidation processes, with oxygen concentrations below 100%. For thermal oxidation an atmosphere diluted by nitrogen [103] oxygen concentrations below 100% may be incorporated by multiplying the coefficient B by the partial pressure of oxygen in the process atmosphere p_{ox} (in %) and the coefficient A with $p_{ox}^{0.5}$. Thus for the following calculations $B_i' = B_i p_{ox}$ and $A_i' = A_i p_{ox}^{0.5}$ are applied, with p_{ox} the oxygen concentration in the process atmosphere. For oxidation in an atmosphere diluted by argon B is again reported to be proportional to p_{ox} , while A is proportional to $p_{ox}^{0.2}$. The additional oxidation mechanisms represented by the constants K_1 and K_2 are reported to show a similar dependence on p_{ox} as B [13]. Thus in the following both the parameterization by Deal and Grove as well as Massoud and Plummer are investigated assuming B , respectively K_1 , and K_2 to be proportional to p_{ox} and A to be proportional to either $p_{ox}^{0.5}$ or $p_{ox}^{0.2}$.

In order to treat oxidation at different temperatures, the temperature profile of the oxidation process is divided in small time steps each of which is at a constant temperature T_n . A schematic representation of this principle is depicted in Figure 28. For each step the growth of the intermediate SiO₂ layer is calculated according to equations (1.8) and (1.11) using the temperature T_n , the time duration t_n , and the partial pressure of oxygen $p_{ox,n}$ as input parameters. For an increase in the number of intervals, the simulated temperature profile approaches the experimental profile represented by the dashed line in Figure 28. However it is unclear how many intervals or which minimum interval size needs to be chosen in order for the output (thickness of the intermediate SiO₂ layer) to converge. Thus in the following this convergence behavior in dependence of the number of intervals n_{int} is discussed.

Convergence of iterative modelling

Figure 29 presents the simulated growth of the intermediate SiO₂ layer in dependence of the number of intervals n_{int} . The results in Figure 29 a) are based on the parameterization by Deal and Grove while b) is based on the parameterization by Massoud and Plummer.

In the following first the results of Figure 29 a) are discussed. The simulated layer thickness increases with increasing number of intervals n_{int} for all initial layer thicknesses d_i . At first sight the results seem to converge roughly for $n_{int} \geq 150$. An increase of n_{int} from 150 to 1000 increases the simulated layer thickness by less than 0.5 %. Since it is unclear how far Δd

increases for $n_{\text{int}} > 1000$ the remainder term is estimated using the root criterion. To do so the value of

$$\max(\sqrt[n]{a_n}), \quad (3.6)$$

where a_n describe the n^{th} term of the series needs to be known. Since $\sqrt[n]{a_n}$ increases for increasing n from 0.3 ($n=2$), 0.4 ($n=3$), 0.5 ($n=6$), 0.98 ($n=1000$), all given for an initial layer thickness of 0 nm an exact mathematical description of $\max(\sqrt[n]{a_n})$ is not straight forward.

Using the value for $n=1000$ in order to estimate the remainder term yields a remainder term that is $< 0.005\%$ relative. Even though this is not mathematically strict, this value might serve as a rough estimate for the order of magnitude of the error.

The convergence behavior of the iterative model based on the parameterization by Massoud and Plummer, which is presented in Figure 29 b), is very similar to a). Also in this case the difference in layer thickness when using 150 instead of 1000 steps is less than 0.5 %. Based on the results presented in Figure 29 for the following simulations the temperature ramps are divided into small intervals with $\Delta T = 4/3^\circ\text{C}$. As a very rough rule of thumb this underestimates the layer thickness by about 0.5 %. After these theoretical considerations the simulated values will be compared to with experimental results in the next paragraph.

Comparison of calculated values and experiment

Figure 30 presents the simulated layer thickness of the intermediate SiO₂ layer calculated using the iterative model presented above. For comparison with the experiment the experimental data for dry oxidation of already existing thermally grown SiO₂ layers from Figure 27 is also shown.

The calculation based on the model by Deal and Grove (“Model DealGrove”) featuring $A \sim p_{\text{ox}}^{0.5}$ shows a decrease in Δd_{SiO_2} with increasing initial layer thickness d_i . For small values of d_i the calculated change in layer thickness Δd_{SiO_2} is slightly lower than the experimental values, but agrees with the experimental values within twice the standard deviation of the experimental data. This effect decreases for increasing d_i until agreement within the standard deviation between experimental and theoretical values is reached around $d_i = 200$ nm.

The model based on the parameterization by Massoud and Plummer (“Model Massoud”) featuring $A \sim p_{\text{ox}}^{0.5}$ results in values of Δd that are about 10 % higher compared to the model by Deal and Grove. Here experimental and theory agree within one standard deviation for 5 out of 6 data points. These results are obtained without the use of free parameters that are

specific to this experimental setup. Please note that there is no agreement in literature on the physical mechanism causing the additional oxidation mechanisms in the model by Massoud and Plummer. This means it is also not clear if these oxidation mechanisms are present for $d_i > 80$ nm.

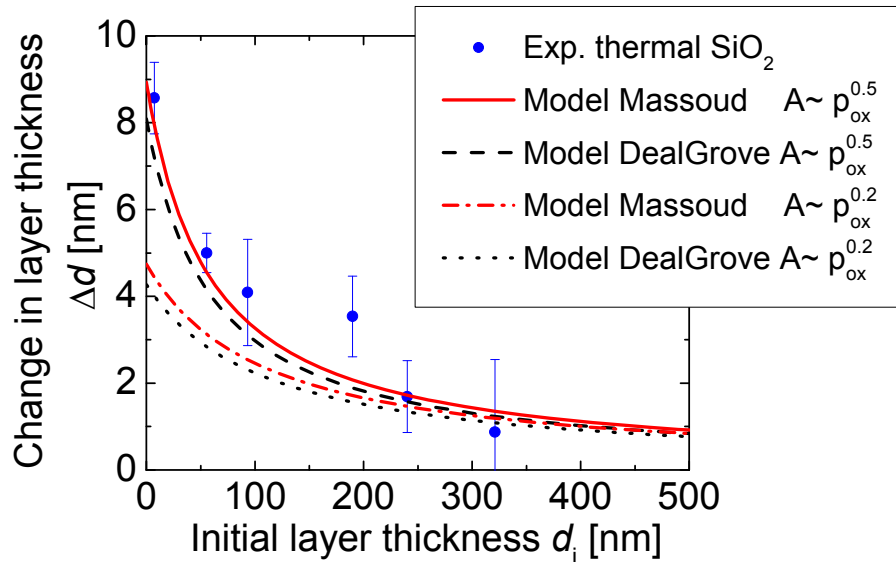


Figure 30: Change in layer thickness Δd over initial layer thickness d_i resulting from oxygen concentration in the process atmosphere (Figure 26). The round data points are experimental data for thermal SiO_2 (compare Figure 27), while the lines stem from the analytical models based on the parameterization by Massoud and Plummer and Deal and Grove respectively.

The assumption of $A \sim p_{\text{ox}}^{0.2}$ decreases the resulting values for Δd for both models. For an initial layer thickness of 0 nm this decrease is approximately a factor of two and leads to a significant discrepancy between experimental and calculated values. In summary, the use of relation $A \sim p_{\text{ox}}^{0.5}$ describes the data best, while both the parameterization “Massoud” and “DealGrove” describe the experimental data reasonably well. After discussing the change in layer thickness for thermal SiO_2 in the following the SiO_x layers deposited by APCVD are discussed.

As described in Figure 27 the change in layer thickness for SiO_x layers deposited by APCVD does not decrease with increasing d_i but stays approximately constant. In order to describe this behavior in the following a constant value of Δd is calculated assuming $d_i = 0$. The results are presented in Figure 31. The constant value calculated according to the parameterization of Massoud results in $\Delta d = 8.9$ nm, while the model by Deal and Grove yields 8.1 nm, both

using $A \sim p_{\text{ox}}^{0.5}$. The value calculated using the model by Deal and Grove fits the experimental data well, since 3 out of the 5 data points lie within one standard deviation of the curve and the other two points lie within twice the standard deviation, as expected from a Gaussian distribution of the measured value.

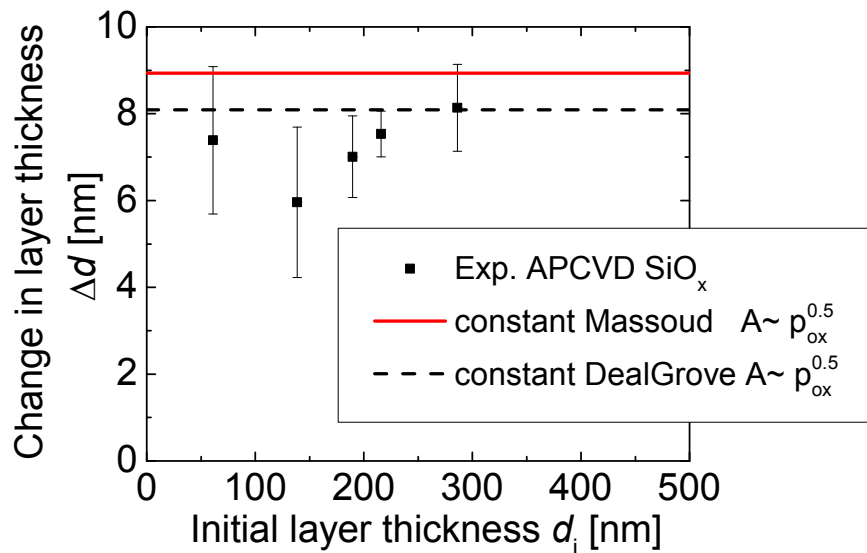


Figure 31: Change in layer thickness Δd over initial layer thickness d_i (Figure 27) resulting from oxygen concentration in the process atmosphere (Figure 26). The square data points are experimental data from APCVD SiO_x , while the constant (solid and dashed) lines are calculated from the analytical models based on the parameterization by Massoud and Plummer and Deal and Grove for $d_i=0$.

In summary, a model is established that allows for the calculation of the thickness of the intermediate SiO_2 layer from the boundary conditions of the experiment, for initial layers being either thermally grown SiO_2 or SiO_x , deposited by APCVD.

3.5.5 Application of the iterative model to quantify the influence of difference parts of the process

The model presented above also allows for extracting parameters that are not easily accessible using experiments. One example is presented in Figure 32. The pie chart presents the thickness of the intermediate SiO_2 layer grown during the high temperature step “with O_2 ” underneath a SiO_x layer deposited by APCVD calculated using the iterative model based on the parameterization by Deal and Grove. The division of a high temperature step in ramps and plateaus is depicted in Figure 26.

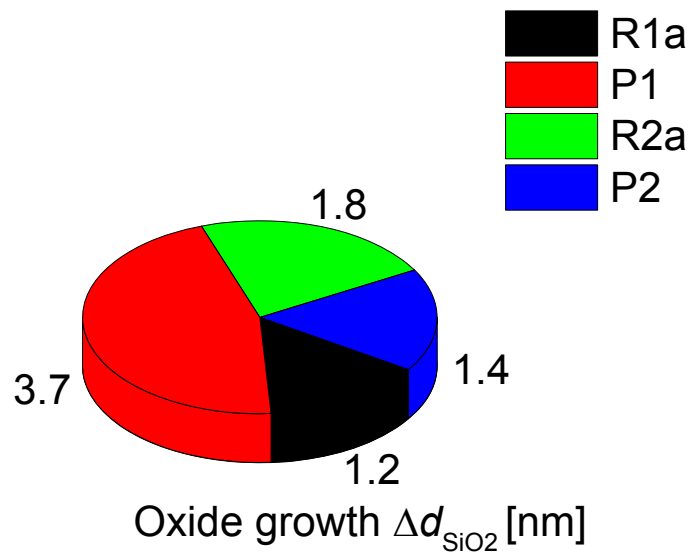


Figure 32: Oxide growth Δd_{SiO_2} calculated using the iterative model (model by Deal and Grove, $A \sim p_{\text{ox}}^{0.5}, d_i=0$) during different phases of the high temperature step “withO2” (Figure 26).

Taking only the oxide growth during the plateaus of constant temperature (“P1” and “P2”) into account amounts for 60% of the total growth in oxide thickness and illustrates the necessity for the iterative model, which allows for calculating the oxide growth during temperature ramps. The results presented in Figure 32 allow for a significantly deeper understanding of co-diffusion processes and substantially simplify their technical development. Concerning a deeper understand from Figure 32 it becomes clear that during all phases of the high temperature step and not only during the highest temperatures the silicon wafer is oxidized, which leads to the injection of Si self-interstitials [104] and influences boron diffusion [26]. With respect to the development of the co-diffusion process requirements for boron diffusion, PSG formation and phosphorus diffusion need to be balanced. Being able to quantify the contribution of p_{ox} to the growth of an intermediate SiO₂ layer during different phases of the high temperature step significantly facilitates this balancing process. The iterative model may be used for a wide range of other applications, e.g. in thermal oxidation processes that are used in the photovoltaic industry, where oxidation generally occurs during the ramp up in order to decrease the process time. A second application are POCl₃ based high temperature processes with two deposition phases, where the diffusion of the dopant during the second deposition phase depends critically on the thickness of the PSG layer grown before the second deposition phase (Section 3.2).

3.5.6 Application of the iterative model to boron diffusion from a borosilicate glass layer

This section briefly presents an application for the iterative model developed in the previous section. One major outcome of this thesis is the development of a co-diffusion process based on a pre-deposited BSG layer and a high temperature step in an atmosphere containing POCl₃. As discussed in Section 3.3.1 the oxygen concentration in the process atmosphere during this process has a large impact on the boron doping profile. Changes in the oxygen concentration smaller than 5 % absolute already induce relevant changes in the boron doping profile. According to the interpretation presented in Section 3.3.4, oxygen in the process atmosphere influences boron doping via the growth of an intermediate SiO₂ layer at the silicon surface. Using ellipsometry it is difficult to detect this layer though, since the intermediate SiO₂ layer is part of a layer stack consisting of a BSG layer with a thickness of around 60 nm and a SiO_x layer with a thickness of 200 to 400 nm. Thus the thickness of the SiO₂ layer comprises around 1 % of the total layer thickness. Additionally the high temperature step changes the density of the SiO_x layer and thus also its thickness. Since deposition conditions for the BSG layer are similar to those of the SiO_x layer, it is possible that also the BSG layer changes its thickness, but this has to the author's knowledge not been investigated yet. Thus in summary, experimentally it is necessary to measure changes in the total layer thickness of 1 % that are superimposed by effects with a similar or larger magnitude and other effects whose magnitude is not characterized yet. This makes this topic very suitable to be investigated by simulations.

The aim of this section is to find a connection between changes in the boron doping concentration and the intermediate SiO₂ layer thickness. To this end Figure 33 presents surface near carrier concentration profiles resulting from boron doping. These result from diffusion from the same BSG/SiO_x layer stack in different oxidizing ambient but featuring the same temperature [101]. Using the iterative model developed in the previous section allows for calculating the thickness of the intermediate SiO₂ layer for an initial layer thickness of 0 nm using the experimental boundary conditions (temperature, time and oxygen concentration in the process atmosphere) as input parameters. Please note that the resulting layer thickness is a representative value for the reaction of oxygen with the silicon wafer. Experimentally the growth of the SiO₂ layer could differ from the calculated values due to the surface texture, the doping concentration in the silicon and the presence of a BRL at the silicon/BSG interface.

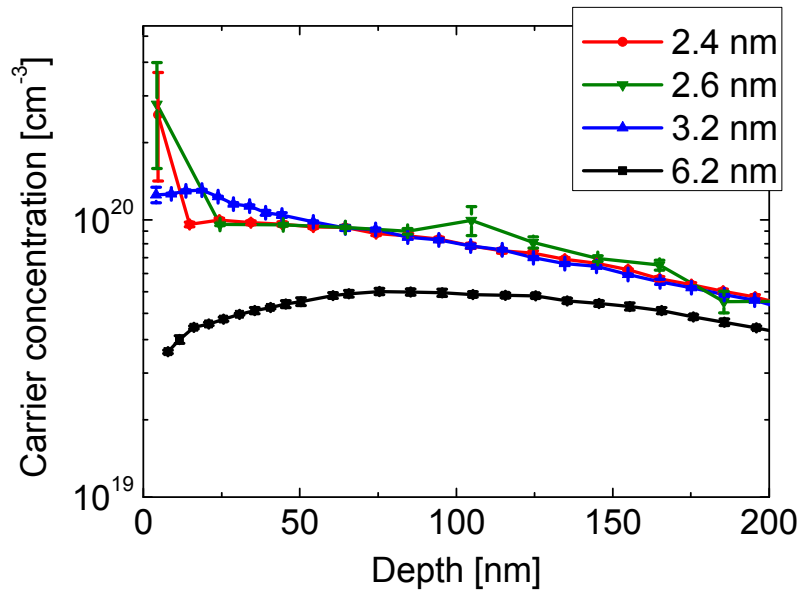


Figure 33: Carrier concentration profiles resulting from boron diffusion in an atmosphere containing different concentrations of oxygen measured by ECV. The error bars represent the measurement accuracy of a single ECV measurement. Each profile is named by the simulated thickness of the intermediate SiO_2 layer Δd_{SiO_2} calculated using the iterative model introduced in Section 3.5.4 (model: DealGrove, $A \sim p_{\text{ox}}^{0.5}, d_i = 0$).

Description of the data

An increase in thickness of the intermediate SiO_2 layer Δd_{SiO_2} correlates with a decrease in the surface near carrier concentration. While for $\Delta d_{\text{SiO}_2} \leq 2.6$ nm the surface concentration is $3 \times 10^{20} \text{cm}^{-3}$, for $\Delta d_{\text{SiO}_2} = 3.2$ nm the surface concentration decreases to 10^{20}cm^{-3} until reaching $4 \times 10^{19} \text{cm}^{-3}$ for $\Delta d_{\text{SiO}_2} = 6.2$ nm.

Discussion

Following the argumentation presented in Section 3.3.3 the two profiles for $\Delta d_{\text{SiO}_2} \leq 2.6$ nm exhibit a boron rich layer (BRL). Increasing the oxygen concentration in the process atmosphere increases Δd_{SiO_2} and oxidizes the BRL or prevents its formation. The absence of the BRL brings the intermediate SiO_2 layer in direct contact with the bulk silicon and reduces the boron doping concentration due to the higher solubility of boron in SiO_2 compared to silicon [76].

The oxidation of the silicon bulk also introduces stacking faults and thus Si self-interstitials [104] which enhances boron diffusion [26].

With respect to POCl₃ based co-diffusion processes this means that the oxygen concentration in the process atmosphere needs to be carefully controlled since changes in Δd_{SiO_2} in the order of only 1 nm already have a significant impact on the boron doping profile especially with regard to the surface doping concentration.

3.5.7 Summary

In this chapter the impact of the oxygen concentration in the process atmosphere p_{ox} on boron diffusion from a BSG/SiO_x layer stack deposited by APCVD is investigated. It is shown that changes in p_{ox} significantly influence the boron doping profile. For the BSG layers under investigation small values of p_{ox} lead to boron rich layer formation, which is for the first time detected using the ECV technique. An increase in p_{ox} oxidizes the boron rich layer or prevents its formation and decreases the surface doping concentration, which is favorable for the application in the solar cell process. This is due to an intermediate SiO₂ layer that forms at the silicon surface, which is detected using ellipsometric measurements. In order to confirm this measurement an iterative model is presented that allows for calculating the thickness of this intermediate layer without free parameters. In contrast to thermally grown SiO₂ layers the interaction between the oxidizing species and SiO_x layers deposited by APCVD is negligibly small. This finding that is to the author's knowledge reported for the first time has a considerable technological impact for co-diffusion processes. It means e.g. that using lowly doped BSG layers deposited by APCVD in combination with oxygen concentrations used in regular phosphorus diffusion might not allow for adequate boron emitter formation, due to the formation of an intermediate SiO₂ layer that prevents sufficient boron diffusion.

After discussing the influence of the oxygen concentration, the next chapter discusses the influence of POCl₃ on boron diffusion from a BSG/SiO_x stack deposited by APCVD.

3.6 Influence of POCl₃ on boron diffusion

3.6.1 Introduction

This chapter discusses the influence of POCl₃ in the process atmosphere on layers deposited by APCVD as well as the resulting boron doping. The experimental setting of the co-diffusion step is as follows: A layer stack consisting of a BSG and a SiO_x layer is deposited single sided on a wafer, which is then subjected to a high temperature process in an atmosphere containing N₂, O₂ and POCl₃. The desired "end product" is a wafer that is boron doped on one side and phosphorus doped on the other side. Since the diffusion is carried out in a gaseous atmosphere one risk is that the boron emitter is overcompensated by phosphorus.

Thus, for the application in solar cells simply speaking a setting, where no phosphorus diffuses through the SiO_x/BSG stack or more precisely no significant influence of POCl₃ on the boron induced carrier concentration profile takes place, is favored.

With respect to thermally grown SiO₂ layers this setting is investigated in references [70, 71]. It is found that POCl₃ reacts with the SiO₂ layer and forms a phosphosilicate glass (PSG) layer at the interface between the gaseous atmosphere and the SiO₂ layer. As the thickness of the PSG layer increases, the thickness of the remaining SiO₂ layer decreases. The growth of a PSG layer with the thickness $d_{PSG,calc}$ may be calculated according to

$$d_{PSG,calc} = (0.9032 \pm 0.0170) nm \cdot 10^6 \sqrt{C_p t / \text{min}} \exp\left(\frac{-0.815 eV}{kT}\right), \quad (3.7)$$

with the volume concentration of phosphorus in the process atmosphere C_p in "percent", the time t in minutes and the temperature T in °K. The rate determining mechanism for the formation of the oxide layer is proposed to be solid state diffusion of P₂O₅ [70]. With respect to the application in solar cells this experimental setting is briefly investigated for layers deposited by PECVD [105]. The research resulted in solar cells with a peak efficiency of 13.8 %. Since the publication focuses on the characterization of solar cells, only little information about specific process details is provided. From SIMS measurements it is followed that a boron rich layer is present at the surface. Also the temperature of the POCl₃ diffusion step of 850°C is given. But the data does not allow for testing the validity of equation (3.7).

The present work investigates for the first time the influence of POCl₃ on SiO_x layers deposited by means of APCVD, which usually feature a different morphology compared to thermally grown SiO₂ [106].

The aim of this section is twofold. From a technological point of view it will be tested if the high temperature processes developed in Section 3.2 allow for a suitable doping in interplay with layers deposited by APCVD or if e.g. the boron emitter is overcompensated by phosphorus from the process atmosphere. This topic is of high relevance, since layers deposited by APCVD are reported to exhibit a higher porosity than thermally grown oxide which are commonly used as "diffusion barriers" against POCl₃ diffusion [106-110]. Thus the diffusion of phosphorus through these layers might be large enough to (partly) overcompensate the boron emitter and have a detrimental effect on solar cell performance. One possibility is e.g. that that POCl₃ reacts directly with the silicon surface rather than the dielectric layers.

From a physical point of view it is interesting to investigate if the reaction of POCl₃ and the SiO_x layer also leads to the formation of a PSG layer. If this is the case it is of high interest to

examine if equation (3.7) is valid not only for thermally grown SiO₂ layers but also for SiO_x layers deposited by APCVD.

3.6.2 Experiment

Planar Float Zone (FZ)-Si wafers with a base resistivity of 0.5 Ωcm and an edge length of 125 mm are subjected to two different APCVD steps resulting in the single sided deposition of a BSG/ SiO_x layer stack. The thickness of the BSG layer is $d_{BSG}=(80\pm 3)$ nm with a refractive index of 1.462 ± 0.001 , both values are averages from 7 identically processed samples. For one sample the BSG is covered by SiO_x layer with a thickness of $d_{SiO_x}\approx(202.5\pm 0.1)$ nm and a refractive index of 1.442 ± 0.001 . A second sample features $d_{SiO_x}\approx(530.5\pm 0.1)$ nm and a refractive index of 1.444 ± 0.002 determined by spectral ellipsometry. The given uncertainties are the errors of the ellipsometric measurement. Please note that the SiO_x layers deposited by APCVD change their thickness during the high temperature step [101]. Thus with respect to the following investigation a relative uncertainty in the thickness of 10% relative is a more realistic estimate. These wafers are then exposed to high temperature processes with gaseous atmospheres featuring different concentrations of POCl₃, N₂, and O₂ (Figure 34 and Figure 10). After the high temperature process the concentration of boron, phosphorus, silicon and oxygen in the layer stack as well as in the region near the silicon surface is determined by SIMS measurements (Section 2.6). Please note that the depth of this measurement is calibrated using a reference sample of thermally grown SiO₂, which might feature a different sputter rate than the SiO_x layer, e.g. due to differences in the microscopic structure. The phosphorus and boron concentration are calibrated using reference samples with thermally grown silicon oxide, while the silicon and oxygen concentration is not calibrated. As mentioned in the experimental section this means that the absolute boron and phosphorus concentrations are only accurate if the matrix of the material under investigation is similar to SiO₂. After removal of the layer stack in a HF based solution, the majority carrier type of the doped silicon surface is determined by a so called "hot point probe", which is a voltmeter where one of the contacts is heated [111]. For other wafers the carrier concentration profile is determined by ECV.

With regard to the application in solar cells it is possible that the BSG/SiO_x layer stack is deposited on either planar or textured surfaces. In order to briefly cover this topic a BSG/SiO_x layer stack is deposited on a textured n-type wafer as well, which is then subjected to a POCl₃ based high temperature step. Afterwards the cross section is investigated by scanning electron microscopy (SEM).

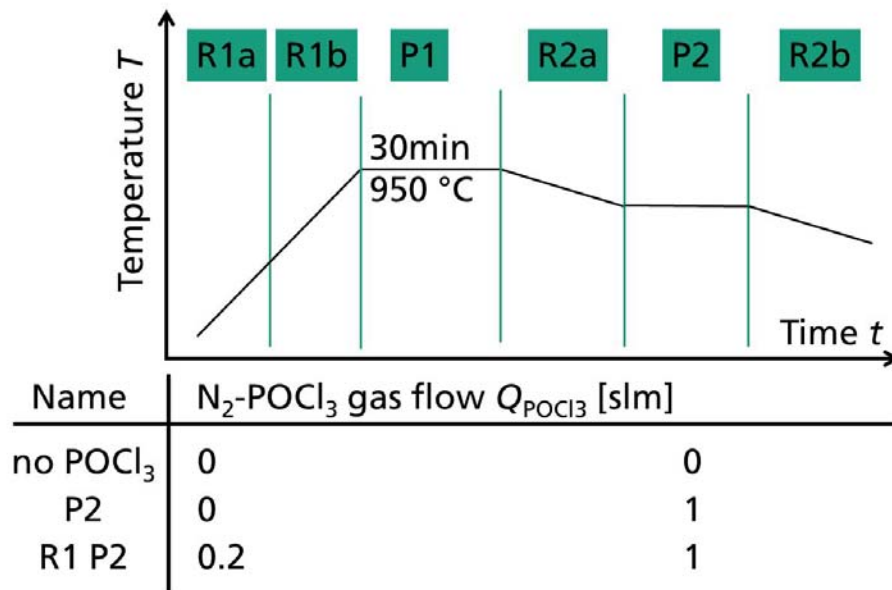


Figure 34: Schematic representation of the high temperature processes used for investigating the influence of POCl₃ in the process atmosphere on the layers deposited by APCVD as well as boron diffusion from these layers. Please note that only the gas flows differing between the processes are shown.

3.6.3 Results

For the high temperature processes using highly doped PSG sources and in-situ oxidation (Figure 10) the “hot point probe” measurements determined n-doping on both sides of the wafer. This is therefore also true for the side of the wafer that was previously covered by the BSG/SiO_x layer stack. This means that the majority carriers are electrons and not holes as one would expect from boron doping. Since a working solar cell requires a pn junction, these high temperature processes in combination with the used BSG/SiO_x layer stack are not relevant for solar cell manufacturing, because they result in a wafer that is n-doped on both sides. Since adjustments of the APCVD layers, like e.g. increasing the SiO_x layer thickness, are not technologically relevant, the high temperature processes based on “high concentration PSG sources” (Section 3.2.2) are not technologically relevant in this thesis and not characterized any further.

In the following, the influence of POCl₃ based high temperature processes (Figure 34) applying lowly concentrated phosphorus sources (Section 3.2.4) on the BSG/SiO_x layer stack and the resulting boron diffusion is investigated.

3.6 Influence of POCl₃ on boron diffusion

Figure 35 presents a SIMS measurement of the BSG/SiO_x ($d_{\text{SiO}_x} \approx 200$ nm) layer stack and the surface near region of the silicon wafer after the high temperature process without POCl₃ in the process atmosphere (Figure 34 “no POCl₃”).

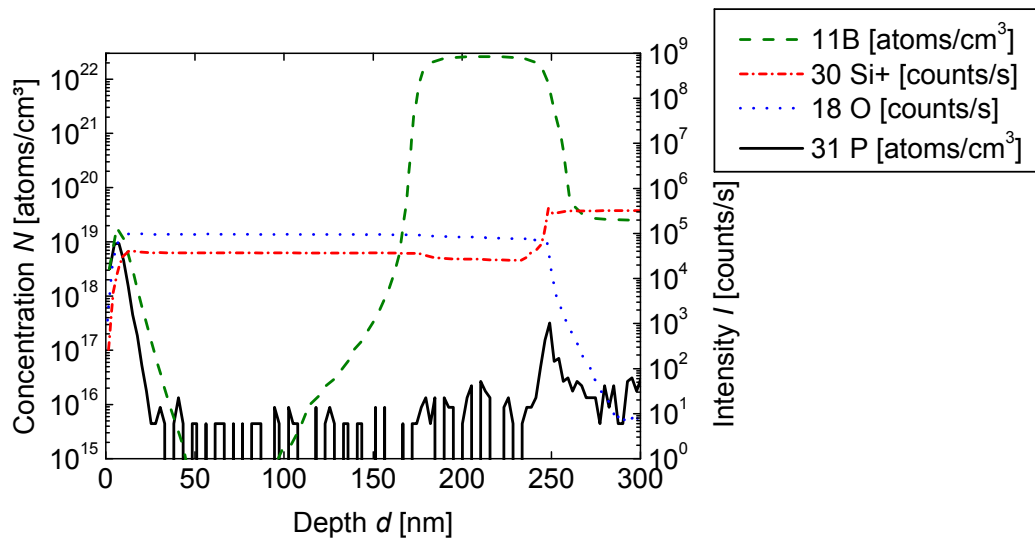


Figure 35: Secondary ion mass spectroscopy (SIMS) measurement of layers deposited by APCVD ($d_{\text{SiO}_x} \approx 200$ nm) after a co-diffusion process with no N₂-POCl₃ gas flow meaning $Q_{\text{POCl}_3} = 0$ for the whole duration of the high temperature step (Figure 34 “no POCl₃”).

The depth $d = 0$ nm corresponds to the SiO_x/air interface. With increasing depth, first the BSG layer and then the silicon wafer is analyzed.

In the following the dependence of the concentration for the different atoms on the depth d is described. After a steep increase for $d < 10$ nm the silicon concentration (30Si^+) stays constant at a value of 3.7×10^4 counts/s. After a depth of around 180 nm the silicon concentration decreases slightly to 2.6×10^4 counts/s. At a depth of around 245 nm second increase up to 3.2×10^5 counts/s is detected. The oxygen concentration (18O) also increases for $d < 10$ nm, stays constant until $d \approx 180$ nm and then decreases slightly until $d \approx 250$ nm. After $d \approx 250$ nm, a strong decrease is observed. Boron (11B) exhibits a concentration of around 10^{19} atoms/cm³ for $d \approx 6$ nm, decreases down to 10^{14} atoms/cm³, increases slightly for $75 < d < 165$ nm, increases sharply until $d \approx 185$ nm, and decreases again around $d \approx 240$ nm.

The phosphorus concentration (31P) follows the boron concentration for depths < 50 nm and then decreases below 4×10^{16} cm⁻³, which is the detection limit. At $d \approx 240$ nm, the P-

concentration increases again until reaching a peak value of $3 \times 10^{17} \text{cm}^{-3}$ at $d \approx 250 \text{ nm}$. Afterwards the concentration decreases down to a constant value, which is kept until $d = 300 \text{ nm}$.

Simultaneous changes in the concentration of multiple species are thus observed for $d < 10 \text{ nm}$ (boron and phosphorus), for $d \approx 180 \text{ nm}$ (boron, silicon, oxygen) and for $d \approx 250 \text{ nm}$ (boron, oxygen, phosphorus, silicon).

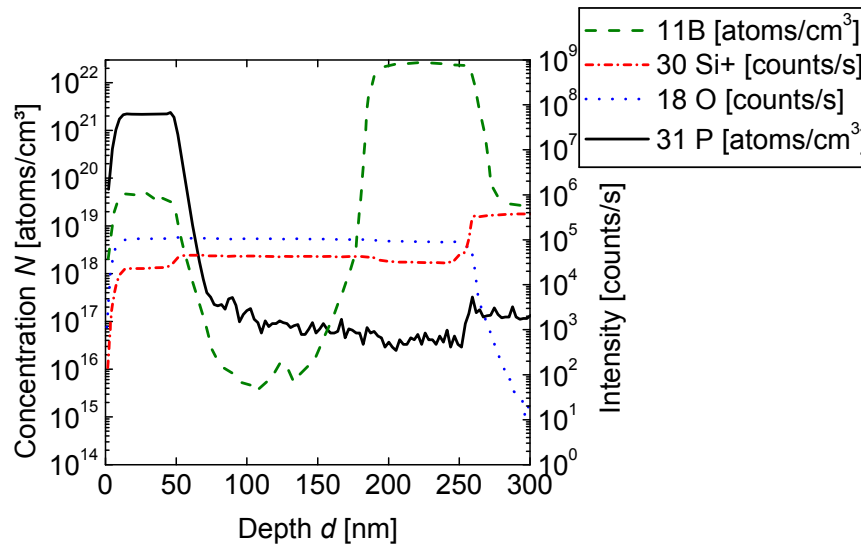


Figure 36: SIMS measurement of dielectric layer stack ($d_{\text{SiO}_x} \approx 200 \text{ nm}$) after co-diffusion process with $\text{N}_2\text{-POCl}_3$ gas flow in the first and second deposition phase (Figure 34 "R1 P2").

Figure 36 describes results based on the same BSG/SiO_x ($d_{\text{SiO}_x} \approx 200 \text{ nm}$) layer stack, but this time measured after a high temperature process with POCl₃ in the process atmosphere "R1P2" (Figure 34). In the following the trends in Figure 36 are described and compared to those of Figure 35. While the dependence of the oxygen concentration on d is similar in both figures, the trends for the other atoms differ considerably, especially for $d < 80 \text{ nm}$. Here the phosphorus and boron concentration reach maximum values of $2 \cdot 10^{21}$ and $5 \cdot 10^{19} \text{ atoms/cm}^3$, respectively. In case of the phosphorus concentration, this is 2 orders of magnitude higher than the phosphorus concentration resulting from the high temperature process without POCl₃ in the process atmosphere. In contrast to the high temperature process without POCl₃, these maximum values stay constant until $d \approx 50 \text{ nm}$ and then show a step decrease. At the same depth the silicon concentration changes as well.

A second major difference of the concentration profiles is that the simultaneous change in concentration of boron, silicon, and oxygen in Figure 36 is situated at $d \approx 190$ nm which is 10 nm larger than for the process without POCl₃ in the process atmosphere.

An additional difference in Figure 36 is observed for $80 < d < 250$ nm, where the phosphorus concentration is higher compared to Figure 35.

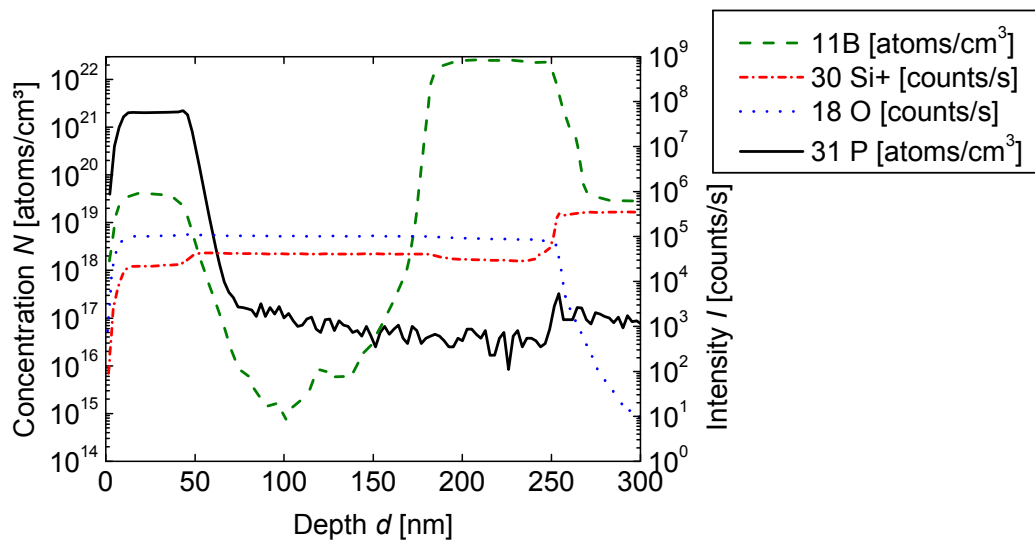


Figure 37: SIMS measurement of dielectric layer stack ($d_{\text{SiO}_2} \approx 200$ nm) after a co-diffusion process with non-zero N₂-POCl₃ gas flow in the second deposition phase (Figure 34 "P2").

Figure 37 presents the atomic distribution for a sample ($d_{\text{SiO}_2} \approx 200$ nm) after exposure to a high temperature step with POCl₃ in the second deposition phase (Figure 34 "P2"). The distribution of the atoms is very similar to the one presented in Figure 36. A slight difference is observed in the phosphorus concentration which starts decreasing from its maximum concentration of $2 \times 10^{21} \text{ cm}^{-3}$ at $d \approx 43$ nm and reaches a value of $2 \cdot 10^{17} \text{ atoms/cm}^3$ at $d \approx 74$ nm. These values of d are around 5 nm smaller than the ones for the high temperature process with POCl₃ in the first and second deposition phase. The values of the maximum concentration of boron and phosphorus are comparable.

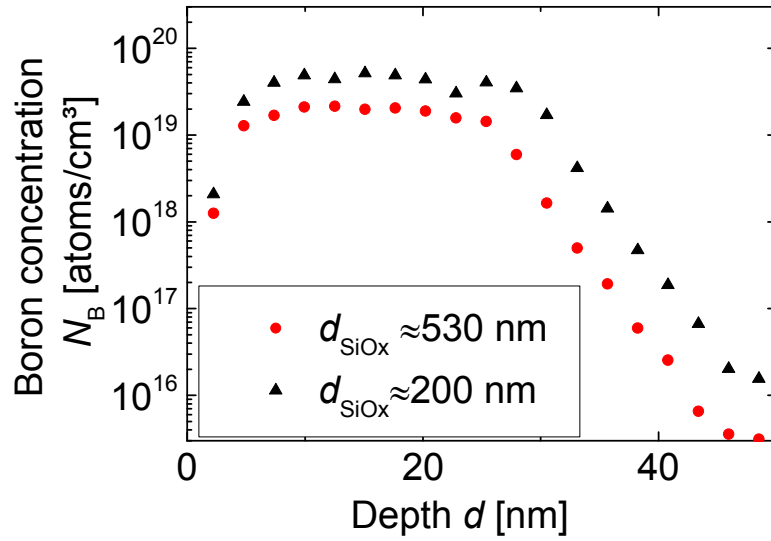


Figure 38: Boron concentration (isotope ^{11}B) from SIMS measurement of BSG/SiO_x layer stack ($d_{\text{SiO}_x} \approx 200$ nm and $d_{\text{SiO}_x} \approx 530$ nm) after a co-diffusion process with non-zero N₂-POCl₃ gas flow in the second deposition phase (Figure 34 "P2"). Each measurement is denoted by the thickness of the SiO_x layer.

The concentration of boron N_B in the surface near region is investigated in more detail in Figure 38. The boron concentration resulting from a layer stack with $d_{\text{SiO}_x} = 200$ nm features

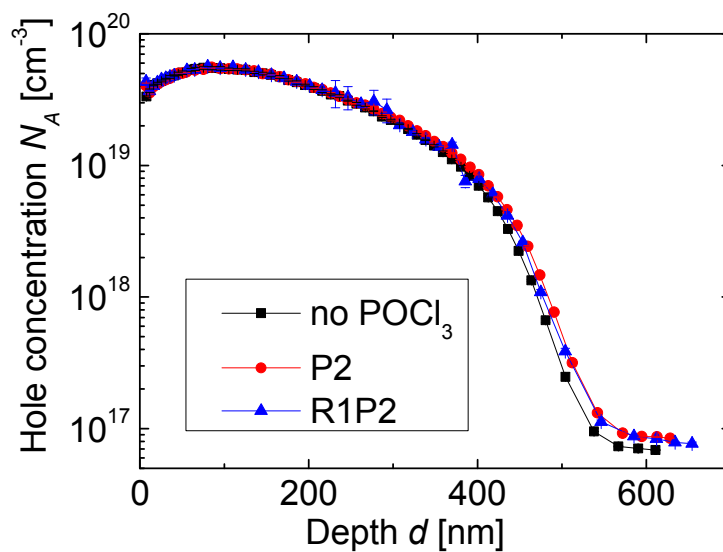


Figure 39: Hole concentration N_A over depth d for boron doping resulting from co-diffusion processes with different POCl₃ concentrations in the process atmosphere. These processes are depicted in Figure 34. The error bars represent the measurement accuracy of a single ECV measurement.

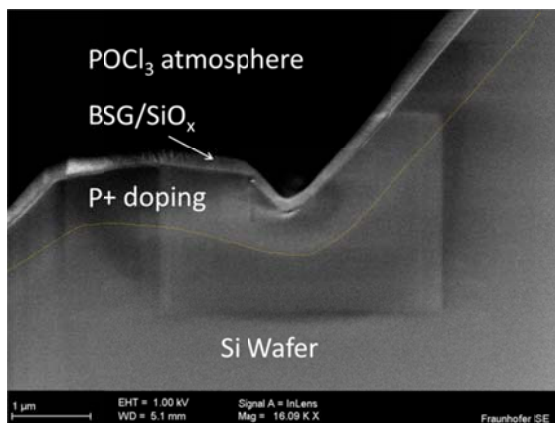
3.6 Influence of POCl₃ on boron diffusion

a maximum concentration of $5 \times 10^{19} \text{ cm}^{-3}$, while for $d_{\text{SiO}_x} \approx 530 \text{ nm}$ the maximum concentration is $2 \times 10^{19} \text{ cm}^{-3}$. The decreasing slopes for both values of d_{SiO_x} are approximately parallel. The depth $d=38 \text{ nm}$ corresponding to a doping concentration of $5 \times 10^{17} \text{ cm}^{-3}$ for $d_{\text{SiO}_x} \approx 200 \text{ nm}$, is 5 nm larger than the value for $d_{\text{SiO}_x} \approx 530 \text{ nm}$. The ratio of the integrated boron concentrations for $0 < d < 46 \text{ nm}$ for the two doping profiles in Figure 38 is 0.4. This is the same value as the inverse ratio of the corresponding layer thicknesses ($200/530=0.4$).

Figure 39 presents the carrier concentration at the silicon surface of the wafer that was originally covered by the BSG/SiO_x ($d_{\text{SiO}_x} \approx 200 \text{ nm}$) layer stack after different high temperature processes (Figure 34). The ECV measurements show that the dominating carriers are positively charged; the wafer surface is p-doped. The latter observation is expected at least for the process "no POCl₃", since B-diffusion is performed from BSG in an atmosphere without any dopant atoms.

The doping profiles presented in Figure 39 are identical within measurement accuracy. This means that different POCl₃ concentrations in the process atmosphere do not measurably change the boron doping profile.

a)



b)

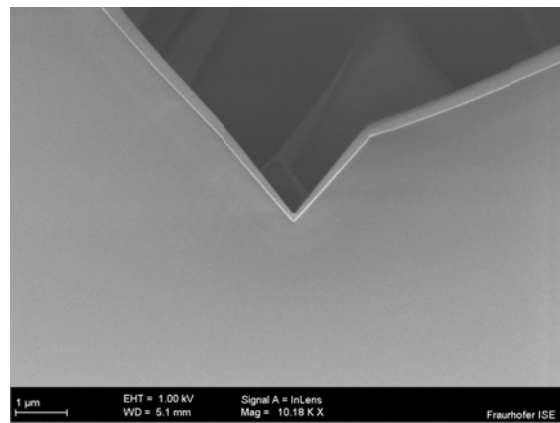


Figure 40: Scanning electron microscopy (SEM) images of the cross section of BSG/SiO_x layer stack on textured silicon wafer after POCl₃ based high temperature process. In a) the line representing the pn junction is marked with a yellow dashed line.

Figure 40 presents cross sectional SEM images of a textured wafer with a BSG/SiO_x layer stack after a high temperature step with POCl₃ in the diffusion atmosphere. In Figure 40 a) the location of the p⁺ doping diffused from BSG is highlighted. Two observables are of interest: One is the homogeneity of the p₊ doping and the layer stack. The second is a possible "lift

off" of the layer stack in the "valleys" of the pyramids, as was observed for layers deposited by PECVD (Seiffe unpublished) on textured surface and if this effect influences the formation of the p^+ doping.

In Figure 40 a) a slightly brighter area is observed starting from the silicon surface to a depth of around 700 nm. The BSG/SiO_x layer thickness varies roughly between 140 and 240 nm. In the central valley a little gap between the layer stack and the Si wafer is observed. The „bright line“, which represents the pn junction is not interrupted. Figure 40 b) shows a typical valley. Here again the layer thickness decreases towards the valley from roughly 300 nm to about 100 nm, but no "lift off" is observed. Again the bright line, representing the p-n junction, is continuous.

3.6.4 Discussion

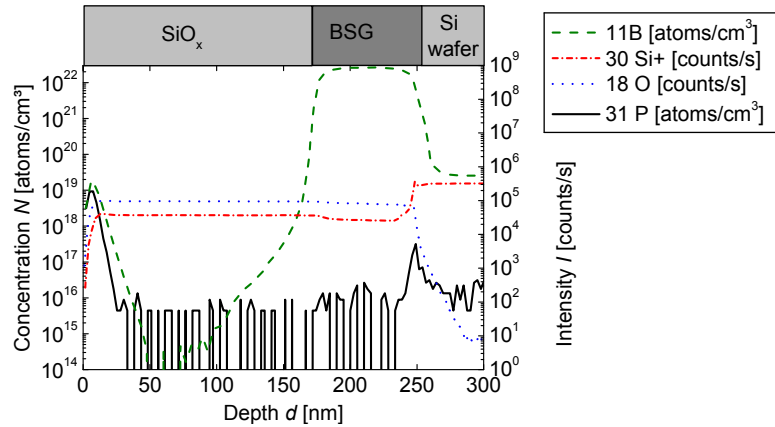
This section starts with discussing the results presented in Figure 35, Figure 36, and Figure 39. In order to facilitate discussion, the data from Figure 35 and Figure 36 in combination with the proposed layer stack is displayed in Figure 41.

The data in Figure 41 a) is compatible with the following layer stack: For $d > 250$ nm the detected signal stems from the bulk silicon wafer with a high boron concentration due to the boron doping from the BSG layer. The boundary to the BSG layer is characterized by a simultaneous change in boron, phosphorus, silicon and oxygen concentration. Next to the bulk silicon wafer, between 180 and 250 nm, the BSG layer which consists of boron, oxygen and silicon is located. For $d < 180$ nm a SiO_x layer is present, which originally consisted of silicon and oxygen. During the high temperature step boron from the BSG layer diffuses into the SiO_x layer leading to the tail in boron concentration for $100 < d < 150$ nm. Up to this point the results are exactly as expected and rather trivial. The phosphorus concentration for small values of d might be caused by the so called "P-outdiffusion" of phosphorus e.g. from the walls of the diffusion tube. The concept is that during a previous high temperature process a phosphorus containing species is deposited on the tube walls. During the following high temperature step this species detaches from e.g. the tube walls and increases the P-concentration in the process atmosphere. Recently this effect has also been suggested in literature [112].

Of high interest are the results for the process with POCl₃ in the process atmosphere (Figure 41 b). Here a layer with a high phosphorus concentration of $2 \cdot 10^{20}$ atoms/cm³, which is in the following referred to as "PSG layer", forms at the interface between SiO_x and the ambient. This behavior was also observed for the reaction between POCl₃ and thermally

grown SiO₂ layers [71]. Thus one finding is that, concerning the effect of PSG formation by POCl₃, SiO_x layers deposited by APCVD and SiO₂ are qualitatively similar.

a)



b)

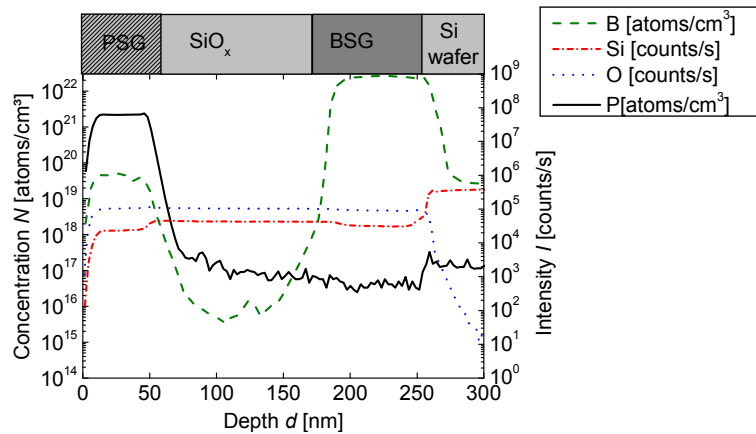


Figure 41: SIMS measurements of BSG/SiO_x layer stack after a high temperature step without a) and with b) POCl₃ in the atmosphere taken from Figure 35 and Figure 36. Above the top x-axis the proposed sample structure is shown

Using equation (3.7), which describes the growth of a PSG layer in thermal SiO₂ to calculate the thickness of the PSG layer yields $d_{\text{PSG,calc}}=59$ nm. This value lies within the decreasing flank of the phosphorus concentration corresponding to a concentration of 10^{19} atoms/cm³. At a first glance, equation (3.7), describing the PSG-growth on thermally grown SiO₂, is also valid for SiO_x layers deposited by APCVD.

An estimate how accurately equation (3.7) describes the growth of the PSG layer in SiO_x is more complicated though. Equation (3.7) is in part deduced empirically from experimental data obtained by etch rate studies [71]. In this study, the PSG layer thickness is defined as the thickness for which the etch rate is higher than around 1 Å/s. This means the boundary of

the PSG layer is set at a P₂O₅ concentration of around 2-3 mol%, which corresponds to a phosphorus concentration of around $1\text{-}2\cdot 10^{21}$ atoms/cm³. For the data concerning SiO_x layers this concentration is reached for $d=(47\pm 1)$ nm. But also the experimentally obtained values of d need some interpretation. These values of d are based on a calibration using a reference sample with an undoped thermally grown SiO₂ layer. Comparing the data in Figure 37 with measurements by ellipsometry yields that this underestimates the total layer thickness by roughly 10 %. Assuming the sputter rate of the PSG layer to be the same as for the SiO_x layer means that the thickness of the PSG layer is underestimated by around 10 %, which yields a corrected experimental value of $d=(52\pm 1)$ nm at a concentration of $1\text{-}2\cdot 10^{21}$ atoms/cm³. By comparison with this value the PSG thickness $d_{\text{PSG,calc}}=59$ nm deviates by about 10 % from the experimental data. Considering further uncertainties in e.g. the experimental determination of the absolute phosphorus concentration it is concluded that, within measurement accuracy, equation (3.7) allows for a quantitative description of the growth of a PSG layer in SiO_x layers deposited by APCVD. With regard to application this means that the possible parameter range of the POCl₃ based high temperature process is limited, depending on the diffusivity of POCl₃ through the dielectric layer (stack) that is used as a doping source. This finding is very important when considering the use of different doping sources, such as layers deposited by PECVD.

A second aspect that is of fundamental interest is the increased boron concentration in the PSG layers in Figure 36 and Figure 37 compared to the boron concentration in the SiO_x layers. This effect is to the author's knowledge observed for the first time. A possible explanation is that the solubility of boron in the PSG layer is higher compared to the SiO_x layer. A second possibility is that the difference in the measured signal is due to the different matrixes of the PSG and SiO_x layer that cause a change in ion yield. Due to their atomic structure the author expects that the ion yield in PSG and SiO_x differs by less than the ion yield of SiO_x and bulk silicon. Since ion yields of the latter materials differ by three orders of magnitude at most the author expect that the different matrix structures of PSG and SiO_x may only partially explain the increase of 4 orders of magnitude of the boron from the SiO_x to the PSG layer.

The next paragraph presents a possible explanation for the observed change in boron concentration with SiO_x layer thickness (Figure 38). There it was observed that increasing the thickness of the SiO_x layer decreases the dose of boron in the PSG layer. The presented explanation assumes diffusion of boron from the BSG through the SiO_x into the PSG layer. Possible diffusion from the PSG layer into the gaseous ambient is neglected. The following

discussion is similar to the model for thermal oxidation proposed by Deal and Grove [12]. The concept includes the following stages (Figure 42). A species containing boron is transported across the BSG/SiO_x interface with a flux F_1 , then diffuses through the SiO_x layer (flux F_2) and finally into the PSG layer (flux F_3), where the solubility of this species is assumed to be higher than in SiO_x. F_1 is expected to be a function of the boron concentration in the BSG layer C_{BSG} , the concentration of boron in the SiO_x layer at the SiO_x/BSG interface C_0 and the segregation coefficient for the BSG/SiO_x system m_{BSG/SiO_x} . The flux through the SiO_x layer F_2 is a function of C_0 , C_1 , the diffusivity D of the relevant species in SiO_x and the thickness of the SiO_x layer d_{SiO_x} . In analogy to F_1 , the flux F_3 through the SiO_x/PSG interface is a function of C_1 , the boron concentration in the PSG layer and the segregation coefficient for the SiO_x/PSG system.

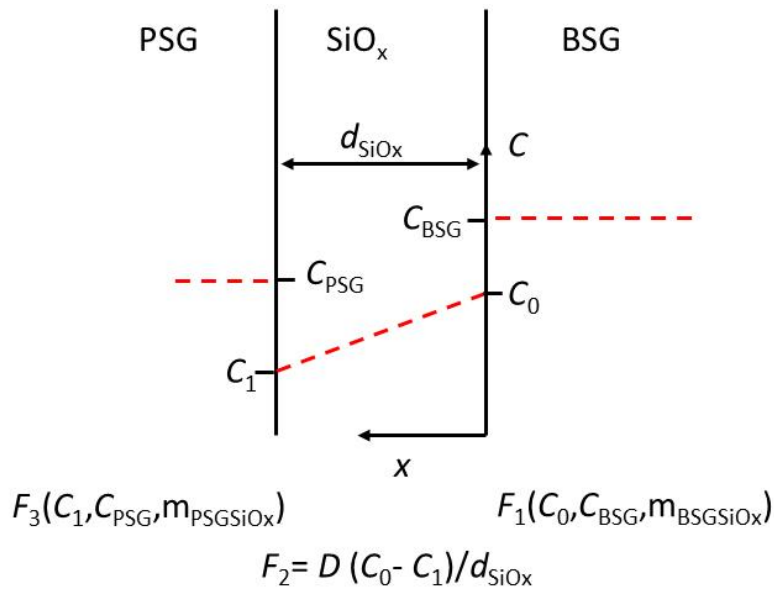


Figure 42: Model for boron diffusion from BSG into PSG layer loosely based on reference [12].

The following discussion is based on steady state conditions, which means that the fluxes in the three above mentioned steps (F_1 , F_2 , and F_3) are equal. In order to test the validity of this assumption a hypothetical event that causes a deviation from steady state conditions is examined. If the time needed to return to steady state conditions $t_{transient}$ is considerably smaller than the total process time $t_{process}$ the assumption of steady state conditions is confirmed [12]. As a hypothetical deviation from steady state conditions in the following an instantaneous decrease of the concentration of the diffusing species in the SiO_x layer to zero is considered. Please beware that for the following discussion similar ion yields of boron in SiO_x and PSG are assumed. Since the diffusion species is unknown, in the following the

“diffusing species containing boron” is denoted simply as “boron”. A possible condition for the steady state assumption is

$$\frac{\text{amount of boron needed to return to steady state conditions}}{\text{boron flux}} \approx t_{\text{transient}} \ll t_{\text{process}}. \quad (3.8)$$

The boron flux may be roughly approximated as follows: The integrated concentration (dose) of boron in the PSG layer $C_{\text{PSG},\text{total}}$ is

$$C_{\text{PSG},\text{total}} = \int_0^{d_{\text{PSG}}} C_{\text{PSG}}(x)dx = \int_0^{t_{\text{process}}} F_3(t)dt, \quad (3.9)$$

with the thickness of the PSG layer d_{PSG} , the boron concentration in the PSG layer C_{PSG} , and the boron flux into the PSG layer F_3 . The amount of boron needed to return to steady state conditions is approximated as the thickness of the SiO_x layer times a typical concentration of 10^{16}cm^{-3} . Using $C_{\text{PSG},\text{total}}$ divided by t_{process} as an averaged boron flux as yields

$$\frac{10^{16}\text{cm}^{-3} \times 500\text{nm}}{4 \times 10^{20}\text{cm}^{-3} \times \text{nm} / t_{\text{process}}} = 5 / 400 \times t_{\text{process}} \approx t_{\text{transient}} \ll t_{\text{process}}, \quad (3.10)$$

which may serve as a rough approximation that steady state conditions are valid. As mentioned above the central implication resulting from steady state conditions is that the fluxes F_1 , F_2 , and F_3 are equal. This means that

$$C_{\text{PSG},\text{total}} = \int_0^{t_{\text{process}}} F_3(t)dt \approx 1/d_{\text{SiO}_x} \int_0^{t_{\text{process}}} D \times (C_0 - C_1)dt, \quad (3.11)$$

with the diffusivity D of boron in SiO_x and the concentration of boron in SiO_x at the SiO_x/BSG and SiO_x/PSG interface C_0 and C_1 . From equation (3.11) it follows that $C_{\text{PSG},\text{total}}$ is inversely proportional to d_{SiO_x} , neglecting the time dependent reduction of d_{SiO_x} due to e.g. the formation of the PSG layer. This results in

$$\frac{C_{\text{PSG},\text{total}}(d_{\text{SiO}_x} = 530\text{nm})}{C_{\text{PSG},\text{total}}(d_{\text{SiO}_x} = 200\text{nm})} \approx \frac{200\text{nm}}{530\text{nm}} \approx 0.38. \quad (3.12)$$

The thus derived ratio of 0.38 ± 0.04 in equation (3.12) agrees with the experimentally obtained value of 0.396. (The error in the experimental value results from uncertainties in the

layer thickness). The agreement of experimental data with the theoretical prediction supports the model that the boron concentration in the PSG layer results from diffusion of a species containing boron from the BSG layer through the SiO_x layer into the PSG layer.

A third aspect of major importance is the independence of the boron doping profiles from the POCl₃ concentration in the process atmosphere presented in Figure 39. As discussed, this independence means that, within measurement accuracy, POCl₃ does not diffuse through the layer deposited by APCVD and compensates the boron doping. Please note that this result is obtained on a planar surface. The results also show that different phosphorus doping profiles on the other side of the wafer do not influence the boron doping profile as would be theoretically possible through the injection of point defects [113-115]. This seemingly marginal result is probably one of the most important results in this thesis. It signifies that the high temperature processes based on lowly doped PSG sources in combination with the introduced layer stack allows for creating different phosphorus doping profiles while leaving the boron doping unchanged. This means that it is possible to study the influence of the back surface field (phosphorus doping) on cell efficiency without the need to account for changes in the emitter (boron doping).

With respect to the technical application in solar cells, the results presented in Section 3.6 signify that POCl₃ in the process atmosphere may lead to the formation of a PSG layer which is separated from the BSG layer and, thus, also from the wafer surface. This means that no relevant diffusion of phosphorus into the boron emitter is expected. This is confirmed by the ECV measurements presented in Figure 39, which show the independence of the doping profile of the boron emitter from the POCl₃ concentration in the process atmosphere. In other words: for the high temperature processes based on lowly doped PSG sources and the layer stack under investigation global overcompensation of the boron emitter by phosphorus on planar surfaces is not supported by the experiment. Due to the well-known porosity of dielectric layers deposited by APCVD [106] this is an unexpected result. For the application in solar cells, these results mean that the layer stack in combination with POCl₃ based high temperature steps allows for forming a pn junction, which is an essential prerequisite for a working solar cell device. The results presented above do not rule out local overcompensation of the boron emitter though. Such an effect could theoretically be possible due to an inhomogeneous deposition of the layer stack on textured surfaces. Spots of local overcompensation were not found in the SEM analysis though. A second possibility to detect these spots are investigations of solar cells under reverse bias. Even though the thickness of the layer stack varies by around a factor of 2, no gap in the pn junction could be observed.

Thus, based on the data presented in this section, the layer stack deposited by APCVD is suitable for the application in a POCl₃ based co-diffusion process.

4 Back surface fields in bifacial n-type solar cells

4.1 Introduction

The back surface field (BSF) is an integral part of a bifacial solar cell and has been shown to have a large influence on solar cell efficiency. Nevertheless very little systematic investigations on the influence of BSF doping profile on cell efficiency exist. Historically especially the description of the BSF has often been very rudimental. Reference [116] shows that quote "lighter doping" of the BSF increases the open circuit voltage V_{oc} and the short circuit current J_{sc} . The 3 doping profiles under investigation are denoted "BSF 1-3". Unfortunately no further characterization of the BSFs is published. Edler [85] performs more extensive characterization. Here an influence of the BSF on V_{oc} , J_{sc} as well as FF is observed. The trend in FF is explained qualitatively by the change in specific contact resistance, while the trends in V_{oc} and J_{sc} are discussed concerning plausibility. In this case the doping profiles of the BSFs are characterized by their sheet resistance. Since the sheet resistance is an integral value, this indication is still ambiguous though. Unfortunately very little details about the process sequence, or the actual parameters that are varied are published, thus it is not clear if changes in cell parameters result only from changes in the doping profile of the BSF or if e.g. emitter doping is affected, too. Furthermore no quantitative investigations that link properties of the BSF and cell efficiency have been published so far.

In the following a comprehensive quantitative experimental investigation of the influence of BSF properties on solar cell efficiency is presented with the aim to fill these gaps. The experimental investigation is enhanced using analytical modelling that connects properties of the BSF with features of the solar cell. For this investigation the co-diffusion process developed in Chapter 3 is of major importance, since it allows for a directed manipulation of phosphorus doping profiles without influencing the boron doped emitter.

In order to achieve a description that is both meaningful and as unambiguous as possible the BSFs, or rather their respective doping profiles, are characterized by their carrier concentration profiles, dark saturation current density J_0 , specific contact resistance ρ_c and sheet resistance R_{sh} . The results from Chapter 3 that allow for a directed independent

manipulation of the phosphorus doping profile, enable a quantitative investigation of the influence of BSF doping concentration on the efficiency of bifacial solar cells. At the end of the chapter an analytical model for simulating the influence of BSF properties on cell efficiency is applied to bifacial solar cells. The following results and discussion are in part published [86, 117].

4.2 Experiment

The experiment is structured as follows. By variation of the N_2 - $POCl_3$ gas flow in the second deposition phase Q_{POCl_3} , back surface fields (BSFs) featuring different surface near doping concentrations are created. The N_2 - $POCl_3$ gas flow in the first deposition phase is constant at 410 sccm. Using test structures the doping profiles are evaluated concerning their dark saturation current density in the passivated part $J_{0pass,BSF}$, specific contact resistance ρ_C and sheet resistance R_{sh} . Based on the results from the test structures and an analytical model, Q_{POCl_3} associated with the high temperature process that allows for the fabrication of solar cells with the highest efficiencies is identified.

The high temperature process is then used for the fabrication of bifacial solar cells and evaluated concerning the IV-parameters η , V_{oc} , J_{sc} and FF .

4.2.1 Test structures for the characterization of the back surface fields

In order to characterize the properties of the BSF, test structures are fabricate according to the process flow depicted in Figure 43. Each test structure allows for the extraction of one or two characteristic properties of the BSF.

The doping profile of the BSF is determined on wafers with planar surfaces and an edge length of 156 mm using the electrochemical capacitance voltage method (ECV). The dark saturation current density J_0 as well as the specific contact resistance ρ_C are characterized on 156 mm wafers with alkaline textured surfaces, whereas the sheet resistance is determined on both planar and textured surfaces by inductive measurements.

All types of test structures are subjected to the same high temperature processes (Figure 44) in an industrial quartz tube furnace. Then the sheet resistance is determined inductively on 66 spots distributed over the surface of wafers with an edge length of 156 mm. Afterwards the phosphosilicateglass (PSG) layer is removed in an HF-based solution.

Samples for determining the contact resistivity are coated by a SiN_x -layer using plasma enhanced chemical vapor deposition (PECVD) before printing a commercially available Ag-paste by screen printing. After contact firing in a belt furnace the specific contact resistance is

determined using the transmission line method (TLM) [61] at four spots distributed evenly over the wafer.

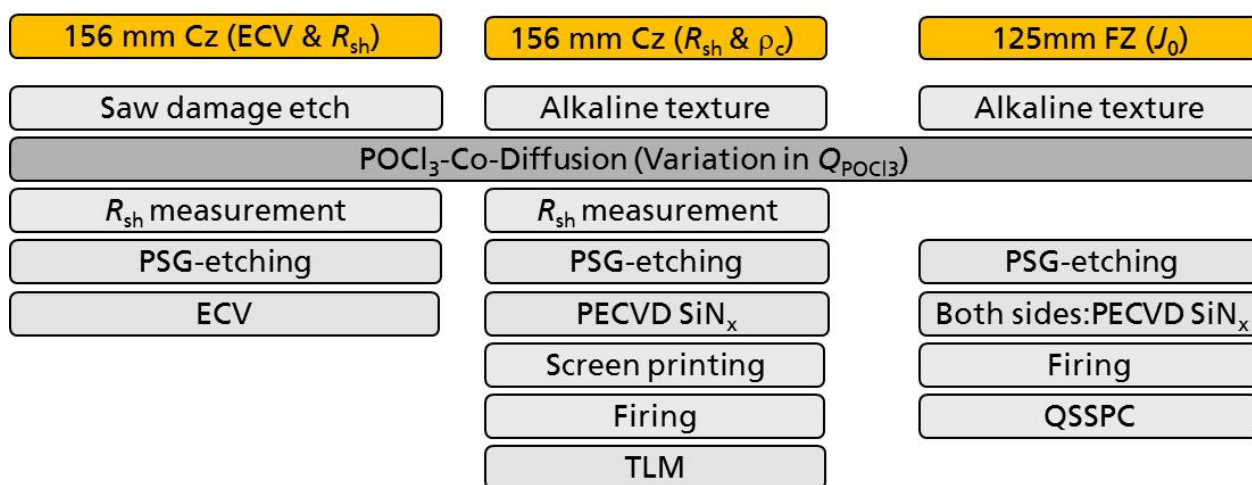


Figure 43: Process flow for the fabrication of test structures used to characterize different properties of phosphorus doped back surface fields (BSFs).

The symmetrical n^+pn^+ carrier lifetimes samples are fabricated using 250 μm thick p-type Float Zone (FZ) silicon wafers with a base resistivity of 1 Ωcm with an edge length of 125 mm. After removal of the PSG layer these wafers are passivated by a SiO_xN_z/SiN_y stack or a SiN_x antireflection coating and then subjected to a firing step simulating contact firing. The lifetime tester Sinton WCT 120 is used for quasi-steady-state photoconductance (QSSPC) measurements yielding the dark saturation current density in low level injection [118]. The measurement is performed in the center of the wafer. Auger recombination is described using the parameterization by Richter et al. [119] and optical factors (f_{abs}) of 1.1 for the SiN_x antireflection coating and 1.05 for the samples passivated by a SiO_xN_z/SiN_x stack. Two symmetrical samples per variation in gas flow are used to determine the dark saturation current density.

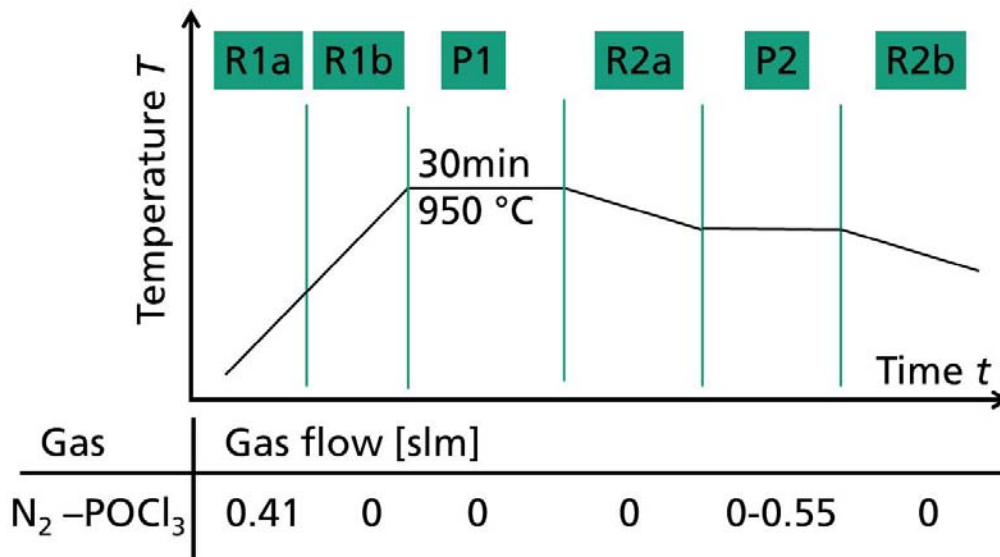


Figure 44: Evolution of temperature and gas flows for high temperature processes characterized in Chapter 4.

4.2.2 Analytical modelling of bifacial solar cells

In order to thoroughly understand the influence of the high temperature processes on the device performance, an analytical model is developed and then used to predict which high temperature process allows for the highest cell efficiency. This analytical model is based on the software tool Gridmaster [120], which was originally developed for the description of p-type Al-BSF solar cells. In this work the model is adapted in order to describe bifacial n-type solar cells (Figure 45 b). The assumptions and adaptations made to the model are discussed in the following. More technical details are given in Appendix B.

This model uses properties of the BSF, namely the doping profile, ρ_C , R_{sh} , and $J_{0pass,BSF}$ as input parameters. For the simulation only illumination from the front side is considered. This allows for neglecting a loss in the short circuit current density J_{sc} due to recombination in the BSF, since most of the energy is absorbed close to the solar cell's front side. Furthermore for illumination from the front side optical shading of the rear grid is irrelevant. Since no analytical model for the spreading resistance for a base and a full area BSF exists, vertical current flow in the base and lateral current flow through a parallel circuit of BSF and base is assumed. For a detailed explanation of this assumption please refer to Appendix C. For the parameters that are not known from experiment e.g. the dark saturation current density of the boron emitter, values that are consistent with own measurements or if these do not exist with literature are chosen. The most important input parameters used for Section 4.5 are

depicted in Table 5. A complete list is provided in Appendix B, **Fehler! Verweisquelle konnte nicht gefunden werden.** The complete list for the simulation parameters used for section 4.8 is displayed in **Fehler! Verweisquelle konnte nicht gefunden werden.**

The metallized boron emitter is assumed to feature a cumulated J_0 of 180 fA/cm². This comprises a contribution from the metallization and from the passivated boron emitter. Recombination in the base material is neglected. The contribution of the front side metallization and boron emitter to series resistance is estimated to be 0.35 Ωcm^2 .

Table 5: Input parameters used for the analytical model describing the impact of the BSF properties on cell efficiency. (For the complete list of input parameters please refer to Appendix B.)

Variable parameters describing the BSF			
$J_{0\text{pass,BSF}}$	$J_{0\text{met,BSF}}$	ρ_c	R_{sh}
[fA/cm ²]	[fA/cm ²]	[m Ωcm^2]	[Ω/sq]
157-529	365-1334	2-11	43-108

Constant parameters describing base and emitter				
Base resistivity	Base thickness	J_{0e}	J_{sc}	J_{02}
[Ωcm]	[μm]	[fA/cm ²]	[mA/cm ²]	[nA/cm ²]
3	180	180	39	20

The dark saturation current density below the contacts on the BSF $J_{0\text{met,BSF}}$ is not easily accessible experimentally, since it depends on screen printing paste, firing conditions and doping profile. As a rough estimate for the value of $J_{0\text{met,BSF}}$ the recombination is calculated using the doping profiles as input parameters for the software "EDNA" [95], assuming a surface recombination velocity of 10⁷ cm/s and multiplying the resulting value with a factor of 1.7 for a textured surface. If the resulting value of $J_{0\text{met,BSF}}$ is smaller than the measured value of the dark saturation current density in the passivated area of the BSF, $J_{0\text{met,BSF}} = J_{0\text{pass,BSF}}$ is assumed. For each doping profile resulting from the high temperature processes the rear side pitch, meaning the distance between the contact fingers is adapted to allow for maximum cell efficiency, if not otherwise stated.

4.2.3 Fabrication of bifacial n-type solar cells

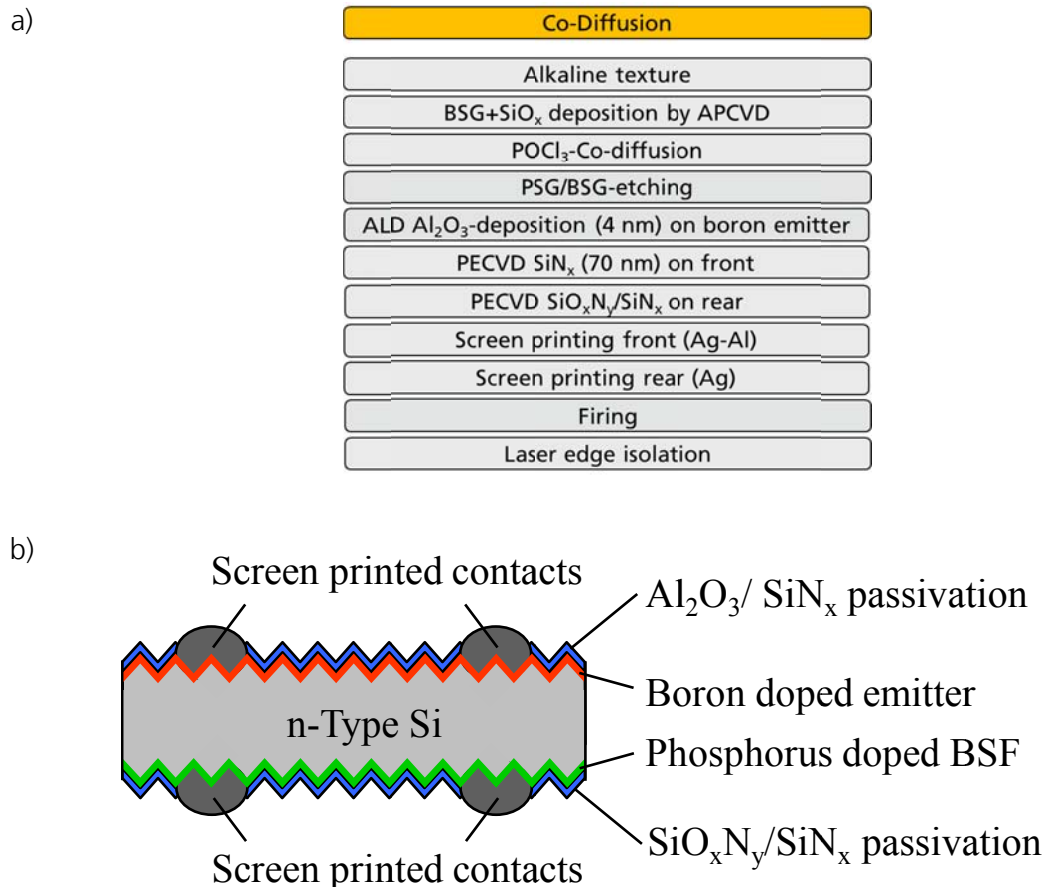


Figure 45: a) Process sequence for the fabrication of bifacial solar cells using a co-diffusion process b) Schematic cross section of bifacial solar cell.

Bifacial n-type solar cells (Figure 45 b) are fabricated according to the process sequence depicted in Figure 45 a). The deposition of the BSG/SiO_x layer stack is performed using an industrial inline tool by SCHMID Group. The other process steps are based on industrial equipment at the pilot line PV-TEC at Fraunhofer ISE. The cells are based on 156 mm × 156 mm pseudosquare n-type Cz-Si wafers with a base resistivity of 1-3 Ωcm. After alkaline texturing a BSG layer covered by a SiO_x capping layer is deposited by APCVD on one side of the wafers in one deposition process. Then wafers are subjected to a POCl₃ based co-diffusion process. The resulting PSG layer as well as the BSG and SiO_x capping layer are removed in a hydrofluoric acid based (HF) solution. Now the boron emitter is passivated by a

stack consisting of 4 nm of Al_2O_3 covered by 70 nm of SiN_x [121] and the phosphorus BSF by a $\text{SiO}_x\text{N}_y/\text{SiN}_x$ stack [121]. The Al_2O_3 layer is deposited by atomic layer deposition (ALD) using an inline tool, the SiN_x layers by PECVD. An H-Grid is printed on both sides of the wafer using screen printing applying single print on both sides. While the paste on the phosphorus doped BSF is a commercially available silver based paste, the paste contacting the boron emitter contains silver and aluminum. After contact formation in a belt furnace a laser edge isolation is performed. An industrial IV tester measures the IV parameters (η , V_{oc} , J_{sc} , FF) after laser edge isolation. As mentioned in Section 2.7, this cell process features 2-3 process steps less, than state of the art processing using sequential diffusion.

In order to verify the absolute values of the IV data and facilitate the comparison of the results with other research groups, selected solar cells are also measured externally at CalLab PVCells at Fraunhofer ISE using two different measurement chucks. The “black” chuck is non-conductive and features a black surface. The “golden” chuck is conductive and features a reflective coating. Compared to the “black chuck”, this increases light reflection on the rear side, which increases J_{sc} and increases conductivity which increases FF [122]. These two measurement principles are necessary, since currently no standard measurement technique for bifacial solar cells exists. The structure of the next sections is as follows: First results of the test structures concerning the electrical characterization of the BSF are presented. Then the change in cell efficiency caused by the different high temperature steps is calculated using an analytical model. The following section then investigates the influence of a few selected high temperature steps on cell efficiency experimentally. The chapter finishes with a quantitative model for the description of the influence of the phosphorus doped BSF on the efficiency of bifacial n-type solar cells, discussing further optimization potential.

4.3 Electrical properties of phosphorus doped BSF

The next sections describes the dependence of the carrier concentration, R_{sh} , ρ_c , and J_0 on the $\text{N}_2\text{-POCl}_3$ gas flow Q_{POCl_3} . The aim is the characterization of high temperature processes that are suitable for co-diffusion. This means that the high temperature steps must create both an adequate phosphorus and boron doping profile, meaning e.g. as little recombination as possible and specific contact resistances well below $100 \text{ m}\Omega\text{cm}^2$.

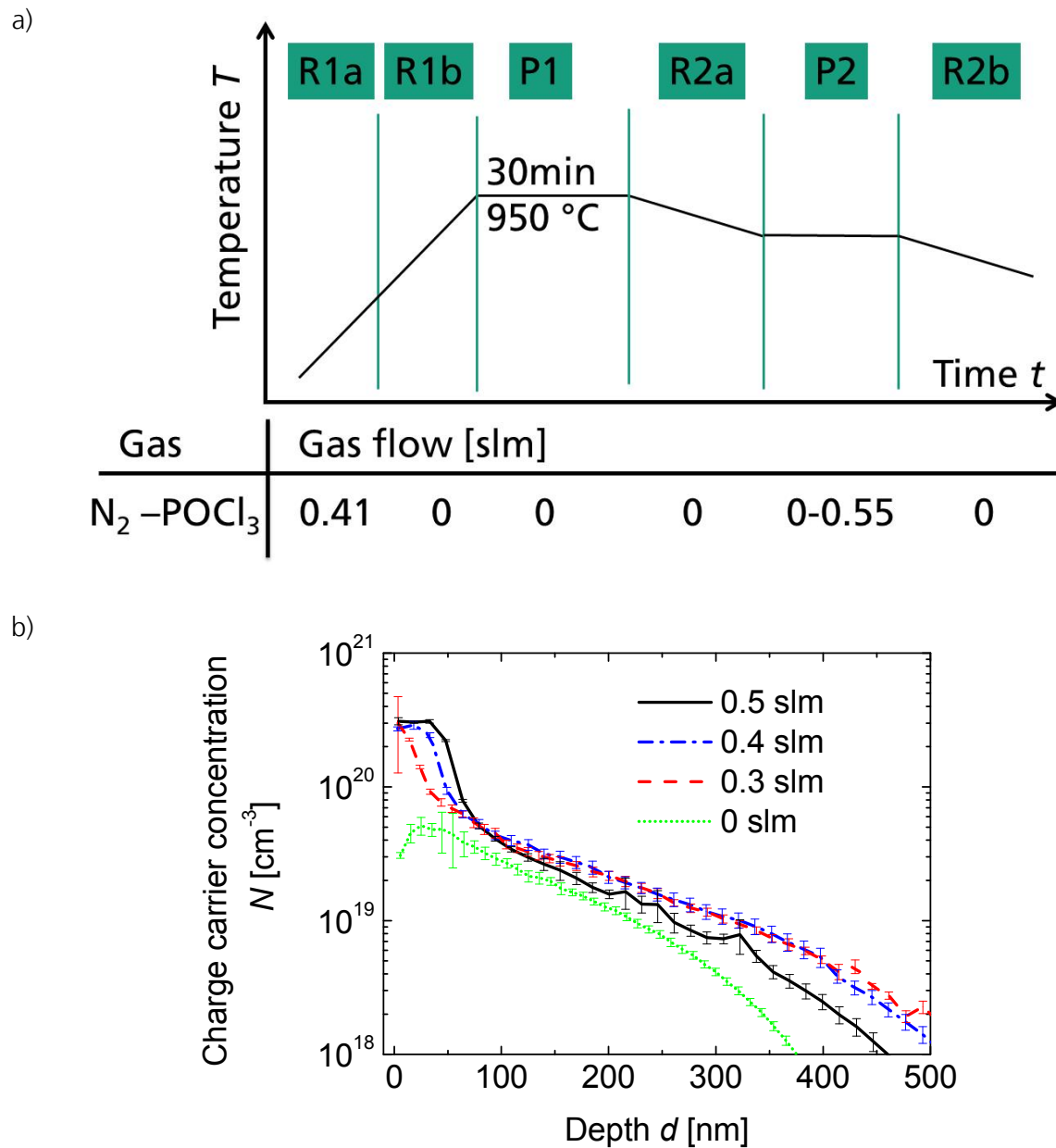


Figure 46: a) Evolution of temperature and gas flows for high temperature processes characterized in this chapter. b) Carrier concentration over depth resulting from phosphorus diffusion) measured by ECV at the center of the wafer. The different high temperature processes are denominated by the N_2 - $POCl_3$ gas flow Q_{POCl_3} during the second (P2) deposition phase (Figure 46 a). The error bars represent the measurement accuracy of a single ECV measurement.

In order to reach suitable phosphorus concentrations at high temperatures “low concentration PSG sources” as introduced in Section 3.2.4 are used. Based on the results in

3.3 the oxygen concentration in the process atmosphere is comparatively low with the aim to allow a sufficiently high boron concentration to result from the co-diffusion process.

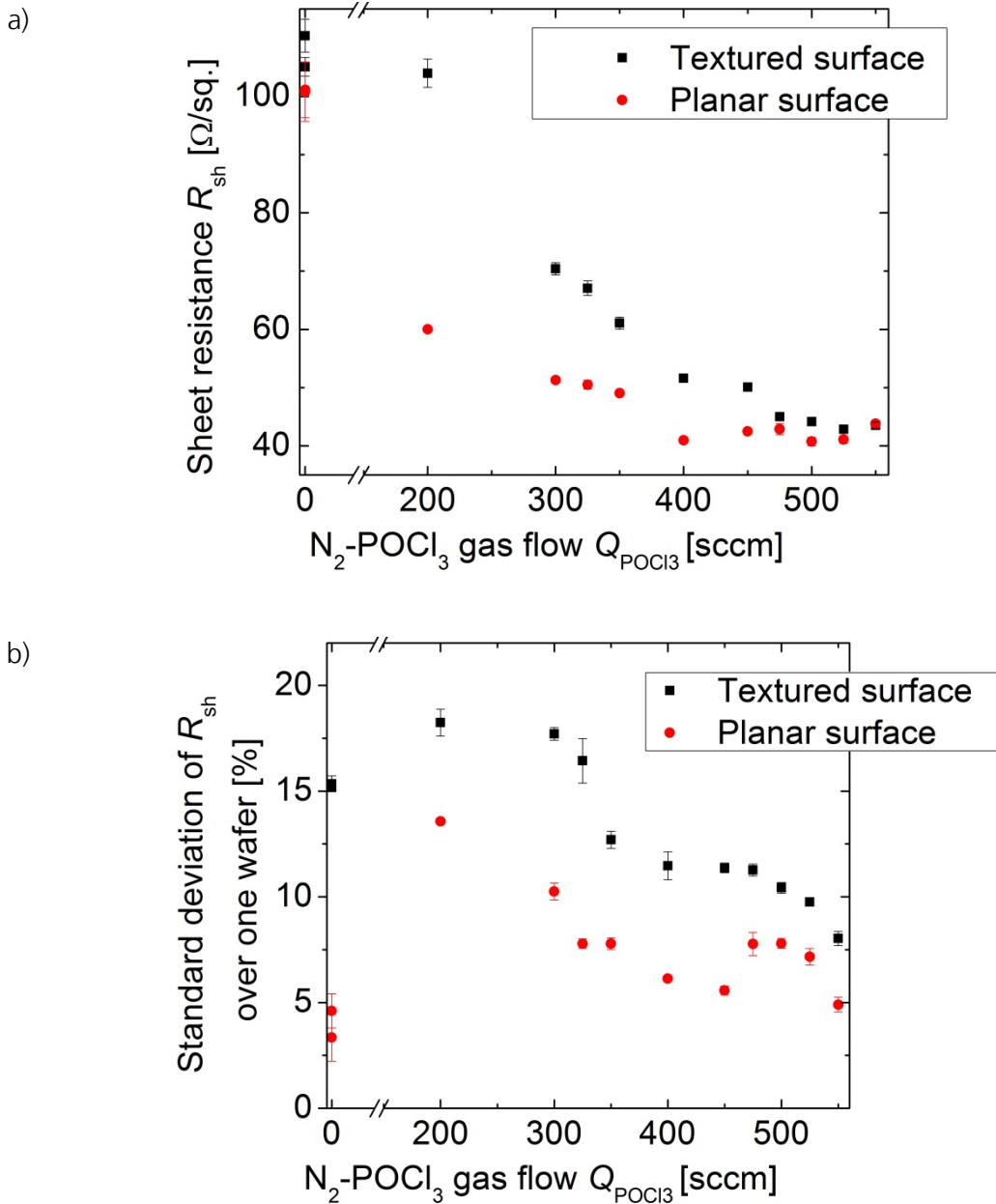


Figure 47:a) Influence of $\text{N}_2\text{-POCl}_3$ gas flow Q_{POCl_3} on averaged sheet resistance R_{sh} of one wafer. b) Influence of $\text{N}_2\text{-POCl}_3$ gas flow Q_{POCl_3} on standard deviation of the sheet resistance over one wafer normalized to the average sheet resistance. Error bars represent the standard deviation of the average value obtained from 3 samples per data point.

4.3.1 Carrier concentration and sheet resistance

Figure 46 a) and b) present process parameters and the resulting carrier concentration for the POCl_3 based high temperature processes characterized in this chapter.

From Figure 46 b) it becomes clear that the integral carrier concentration increases with increasing Q_{POCl_3} . For $Q_{\text{POCl}_3} = 0$ slm the maximum carrier concentration is $5 \times 10^{19} \text{ cm}^{-3}$, while for the other high temperature processes the maximum carrier concentration is $3 \times 10^{20} \text{ cm}^{-3}$ which is the activation limit of phosphorus in silicon for the applied diffusion temperature [30]. Please also note that the absolute difference between carrier concentration profiles for $Q_{\text{POCl}_3} \geq 0.3$ slm is largest for the surface near doping concentration, while variations in the depth are close to measurement accuracy.

Figure 47 presents inductive measurements of the sheet resistance and its standard deviation over one wafer for textured and planar surfaces as a function of the N_2 - POCl_3 gas flow Q_{POCl_3} during the second deposition phase of the co-diffusion process. Please note that during the first deposition phase a PSG layer is deposited on the wafer surface resulting in a sheet resistance of roughly $100 \text{ } \Omega/\text{sq}$ on a planar surface. During the second deposition phase (P2) POCl_3 is added to the process atmosphere increasing the thickness of the already existing PSG layer.

Each data point results from averaging the results of 3 wafers. The two pairs of data points for $Q_{\text{POCl}_3} = 0$ sccm represent results from a high temperature process that was repeated once. The resulting sheet resistances vary by less than 5 %. This point is mentioned at the beginning of the section, since recently the out-diffusion of phosphorus from tube walls has been reported to affect process reproducibility especially for temperatures above 900°C [112].

Concerning the dependence of the sheet resistance on Q_{POCl_3} a clear trend is visible: For both textured and planar surfaces the sheet resistance decreases with increasing Q_{POCl_3} from roughly $100 \text{ } \Omega/\text{sq}$ to about $40 \text{ } \Omega/\text{sq}$ for $Q_{\text{POCl}_3} \sim 450$ sccm. For $Q_{\text{POCl}_3} > 475$ sccm the sheet resistance stays constant within a margin of $1 \text{ } \Omega/\text{sq}$. The standard deviation of the sheet resistance over the wafer is higher for textured than for planar surfaces and exhibits a maximum around $Q_{\text{POCl}_3} = 200$ sccm.

4.3.2 Carrier recombination

Figure 48 shows the dark saturation current density for a textured surface as a function of the N_2 - POCl_3 gas flow Q_{POCl_3} determined on symmetrical lifetime samples. For passivation by SiN_x there is a minimum of J_0 of $160 \text{ fA}/\text{cm}^2$ at $Q_{\text{POCl}_3} = 300$ sccm. For an increase in Q_{POCl_3} the dark saturation current density increases roughly linearly to $530 \text{ fA}/\text{cm}^2$, while for decreasing

Q_{POCl_3} to 0 sccm J_0 increases to 210 fA/cm². For Q_{POCl_3} =200 sccm, the use of an advanced SiO_xN_y/SiN_x passivation stack reduces J_0 to 127 fA/cm², which is 20 % lower compared to SiN_x based passivation for the same value of Q_{POCl_3} .

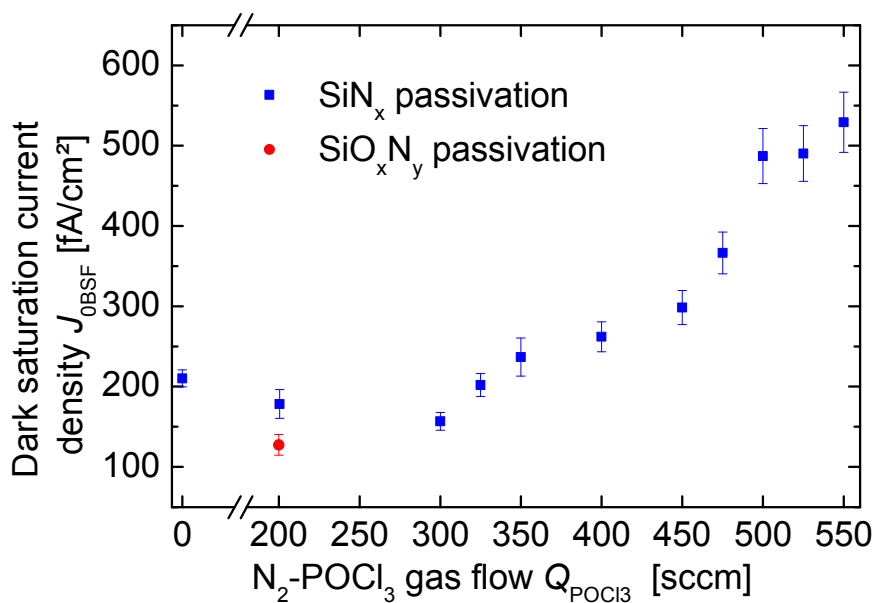


Figure 48: Dark saturation current density over N_2 - POCl_3 gas flow Q_{POCl_3} measured in the wafer center. The error bars are calculated by dividing the measurement uncertainty of a single measurement (10% relative) by the square root of the number of samples per data point.

4.3.3 Specific contact resistance

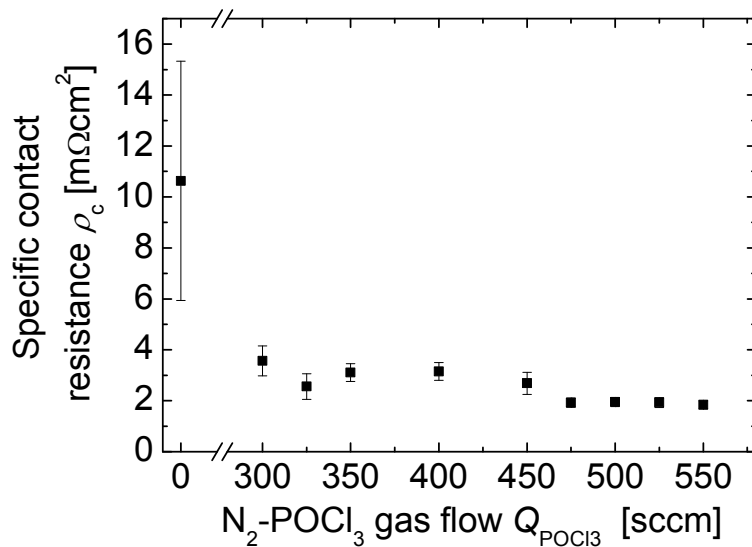


Figure 49: Average specific contact resistance ρ_c as a function of the $\text{N}_2\text{-POCl}_3$ gas flow Q_{POCl_3} determined from four measurement locations. The error bars represent the standard deviation of the specific contact resistance over one wafer.

Figure 49 presents the specific contact resistance of screen printed silver based contacts ρ_c as a function of Q_{POCl_3} . ρ_c decreases with increasing Q_{POCl_3} . The variation of the specific contact resistance over the wafer surface is highest for $Q_{\text{POCl}_3} = 0$ sccm. The change of ρ_c over the wafer correlates with a change in R_{sh} for all Q_{POCl_3} . Low contact resistances are observed at the wafer edges, where the sheet resistance is low, while high contact resistances are measured in the center of the wafer corresponding to high R_{sh} .

4.4 Discussion of electrical properties of phosphorus doped BSF

This section discusses and explains the trends in the carrier concentration profiles, R_{sh} , J_0 and ρ_c observed in Figure 46, Figure 47, Figure 48 and Figure 49.

4.4.1 Carrier concentration and sheet resistance

The doping profile resulting from $Q_{\text{POCl}_3} = 0$ slm features the lowest doping concentration and a maximum carrier concentration of $5 \cdot 10^{19} \text{ cm}^{-3}$ indicating the absence of inactive phosphorus. The doping profile resulting from $Q_{\text{POCl}_3} = 0.3$ slm features a maximum carrier

concentration of $3 \times 10^{20} \text{ cm}^{-3}$, which is the activation limit of phosphorus in silicon [30]. For this doping profile it is not clear if inactive phosphorus is present or not. The other doping profiles, resulting from a further increase in Q_{POCl_3} feature a plateau of constant charge carrier concentration close to the surface. Such a plateau has been observed frequently and involves the presence of inactive phosphorus [123]. Corresponding with an increase in Q_{POCl_3} from 0.3 over 0.4 to 0.5 slm the length of the plateau increases from <6 nm over 38 nm to 51 nm indicating a simultaneous increase in the total concentration of inactive phosphorus. The increase in the concentration of inactive phosphorus with an increase in Q_{POCl_3} , is well known and has e.g. been observed by Negrini et al. [124].

Concerning the dependence of the sheet resistance on Q_{POCl_3} (Figure 47) for both textured and planar surfaces the sheet resistance decreases with increasing Q_{POCl_3} up to $Q_{\text{POCl}_3} \sim 450 \text{ sccm}$, while for $Q_{\text{POCl}_3} > 475 \text{ sccm}$ the sheet resistance stays relatively constant. One explanation for this dependence is that for $Q_{\text{POCl}_3} < 450 \text{ sccm}$ the PSG layer acts as a finite diffusion source. By increasing Q_{POCl_3} , layer thickness and phosphorus concentration in the PSG layer are increased and thus more dopant is deposited onto the wafer [125], decreasing the sheet resistance. For $Q_{\text{POCl}_3} > 450 \text{ sccm}$ the PSG layer acts as a nearly infinite diffusion source at least with regard to the mobile phosphorus. Thus depositing more dopant on the wafer surface changes the sheet resistance only within measurement accuracy. The fact that for $Q_{\text{POCl}_3} > 450 \text{ sccm}$ sheet resistance on textured and planar wafers is similar supports the assumption of an infinite diffusion source.

When comparing sheet resistance on textured and planar surfaces, it becomes clear that these may differ. Following geometrical considerations the same doping profile on textured and planar wafers would cause the same sheet resistance. Thus one may conclude that not only the sheet resistance, but also the doping profile are different for planar and textured surfaces.

4.4.2 Carrier recombination

With reference to J_0 (Figure 48) there is a minimum of J_0 at $Q_{\text{POCl}_3} = 300 \text{ sccm}$ for SiN_x based passivation. For higher and lower Q_{POCl_3} , the dark saturation current density increases roughly linearly with increasing respectively decreasing Q_{POCl_3} . The increase in J_0 for $Q_{\text{POCl}_3} \geq 300 \text{ sccm}$ is attributed to enhanced recombination due to an increase in the near surface concentration of (partly inactive) phosphorus [123]. This is supported by sheet resistance and ECV measurements in Figure 46 and Figure 47. Thus even though the PSG layer acts as an infinite diffusion source concerning the mobile phosphorus, with regard to the immobile phosphorus the PSG layer may not be described as an infinite diffusion source. Thus an increase in Q_{POCl_3}

beyond 450 sccm increases the amount of inactive phosphorus which promotes precipitate formation [126]. For Q_{POCl_3} smaller than 300 sccm there is a slight increase in J_0 , which is attributed to an increasing contribution of surface recombination due to reduced shielding. Consistently, the use of an advanced $\text{SiO}_x\text{N}_y/\text{SiN}_x$ passivation stack reduces J_0 to $\sim 127 \text{ fA/cm}^2$, 20 % lower compared to SiN_x based passivation. Qualitatively the effect of decreased surface shielding is reproduced using the software tool “EDNA” [95]. Using the respective doping profiles and the parameterization of the surface recombination velocity for planar surfaces after Kimmerle et al. [31] and multiplying the resulting values by 1.7 to account for textured surfaces, results in values of $J_0=111 \text{ fA/cm}^2$ and 160 fA/cm^2 for the doping profiles resulting from $Q_{\text{POCl}_3}=300 \text{ sccm}$ and 0 sccm respectively. The absolute values differ by 49 fA/cm^2 compared to the experimentally obtained difference of 33 fA/cm^2 . These values agree well, considering, that the surface recombination velocity and doping profile are determined on planar surfaces, while the experimentally determined value of J_0 stems from a textured surface.

For $Q_{\text{POCl}_3} > 475 \text{ sccm}$ the sheet resistance stays approximately constant while carrier recombination increases linearly (Figure 47 and Figure 48). Thus there is no direct link between sheet resistance and recombination activity. A possible explanation for this effect is an increase in the concentration of inactive phosphorus which leads to an increase in carrier recombination while leaving the sheet resistance nearly unaffected. From this one can deduct that the very common approach to characterize phosphorus doped areas by sheet resistance may be misleading, since it only correlates with conductivity, but may not be an appropriate measure for other electrical properties, such as the dark saturation current density. Thus especially for high concentrations of inactive phosphorus a comprehensive characterization requires spatially resolved J_0 measurements over the wafer surface.

Figure 48 also provides some insight into design of phosphorus doped BSFs and emitters. A common approach for decreasing carrier recombination in phosphorus doped emitters is to increase the sheet resistance. As can be seen by comparing Figure 47 and Figure 48 this approach is only successful for high values of J_0 , where the effects of Auger and defect recombination in the bulk emitter dominate.

4.4.3 Specific contact resistance

With regard to specific contact resistance ρ_c the following trends are observed:

The variation of the specific contact resistance over the wafer surface is highest for $Q_{\text{POCl}_3}=0 \text{ sccm}$. Low specific contact resistances are observed at the wafer edges, where the sheet resistance is low, while high specific contact resistances are measured in the center of

the wafer corresponding to high R_{sh} . As a general trend the specific contact resistance decreases with increasing Q_{POCl_3} .

A common view that links properties of the phosphorus doped areas to contact resistance is that more inactive phosphorus, represented by a higher area coverage of SiP precipitates leads to lower contact resistance [127]. Since a clear increase in recombination is observed for $Q_{POCl_3} > 300$ sccm (Figure 48), which is explained by an increase in inactive phosphorus concentration a corresponding decrease in contact resistance is to be expected. It is surprising though that the contact resistance seems to saturate for $Q_{POCl_3} > 475$ sccm indicating that there might be a threshold concentration above which the addition of inactive phosphorus does not decrease the specific contact resistance any further. A quantitative investigation concerning the microstructure of these contacts will be performed in Chapter 5. After characterizing different properties of phosphorus diffused areas with regard to their application as phosphorus BSFs, the next section evaluates which phosphorus doping profile allows for the highest efficiency when applied for the fabrication of bifacial n-type solar cells.

4.5 Selection of high temperature processes for cell fabrication

The aim of this section is to understand the influence of properties of the BSF on solar cell efficiency and to identify which high temperature process characterized in Section 4.3 allows for the highest efficiency when used for the fabrication of bifacial solar cells. This will be done quantitatively using an analytical model introduced in Section 4.2.2, since a qualitative discussion of the data presented in Section 4.3 remains inconclusive. For each high temperature process, which is denoted by the N_2 - $POCl_3$ gas flow Q_{POCl_3} , a parameter set consisting of R_{sh} , ρ_C , $J_{0pass,BSF}$ and $J_{0met,BSF}$ is used to calculate the fill factor FF and the open circuit voltage. Since J_{sc} is assumed to be independent from the doping profile of the BSF, the cell efficiency is proportional to the product of FF and V_{oc} . For all Q_{POCl_3} the same rear side grid is used

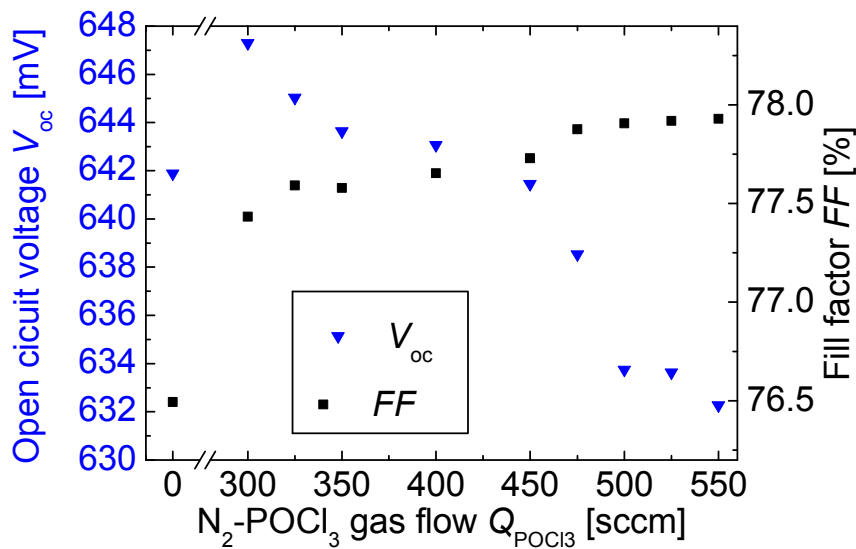


Figure 50: Calculated open circuit voltage V_{oc} and fill factor FF based on experimental data from Figure 47, Figure 48 and Figure 49 calculated using the analytical model described in Section 4.2.2.

Figure 50 presents the calculated open circuit voltage V_{oc} and the fill factor FF . From $Q_{\text{POCl}_3}=0$ to $Q_{\text{POCl}_3}=300$ sccm both V_{oc} and FF increase. For $Q_{\text{POCl}_3}>300$ sccm V_{oc} decreases while FF increases. Since a decrease in V_{oc} decreases cell efficiency, while the increase in FF increases cell efficiency this trade-off needs to be examined quantitatively to identify the process that allows for maximum cell efficiency. Before calculating the efficiency the results in Figure 50 are briefly checked for plausibility.

The open circuit voltage V_{oc} is influenced by the parameters $J_{0\text{met,BSF}}$ and $J_{0\text{pass,BSF}}$. Since the area coverage of the metallization is 8% for all Q_{POCl_3} the influence of $J_{0\text{pass,BSF}}$ on V_{oc} is at least 12 times larger than the influence of $J_{0\text{met,BSF}}$. While $J_{0\text{pass,BSF}}$ changes by roughly 400 fA/cm² $J_{0\text{met,BSF}}$ changes by about 1000 fA/cm² from their respective minimum to maximum values. Thus the trend in V_{oc} (Figure 50) is expected to follow the trend in $J_{0\text{pass,BSF}}$ (Figure 48), which is the case. Thus the trend in V_{oc} is plausible.

Both a decrease in sheet resistance R_{sh} and a decrease in specific contact resistance ρ_c decrease resistive losses and thus increase the fill factor FF . Since both R_{sh} (Figure 47) and ρ_c (Figure 49) show a decreasing trend with increasing Q_{POCl_3} , also the increase in FF with increasing Q_{POCl_3} is plausible.

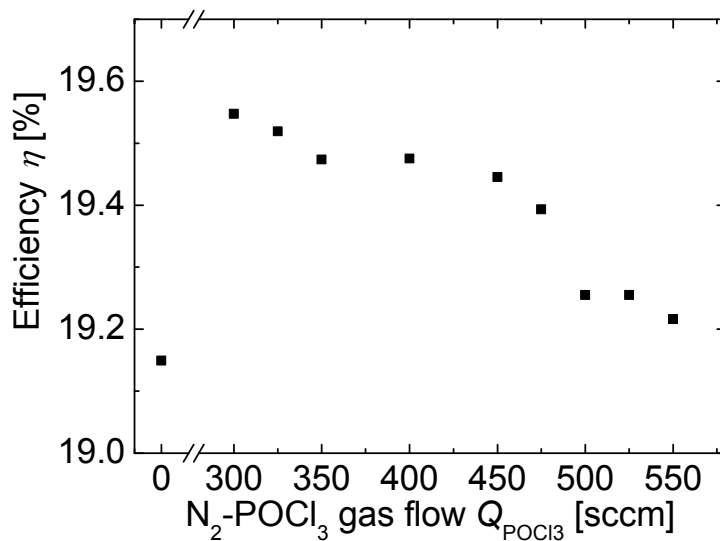


Figure 51: Cell efficiency over Q_{POCl_3} resulting from calculated IV parameters in Figure 50 assuming a constant value of J_{sc} .

The cell efficiency (Figure 51) is calculated as the product of V_{oc} , FF (Figure 50) and a constant value of $J_{\text{sc}}=39 \text{ mA/cm}^2$, which is chosen according to results in Section 4.6. This is divided by the incident power during standard test conditions of 1000 W/m^2 . The maximum in cell efficiency is reached at $Q_{\text{POCl}_3}=300 \text{ sccm}$ for the $\text{N}_2\text{-POCl}_3$ gas flows under investigation. Qualitatively the trend in efficiency follows the trend in V_{oc} and is due to the fact that the relative changes in V_{oc} are larger than the relative changes in FF (Figure 50). Thus the process featuring $Q_{\text{POCl}_3}=300 \text{ sccm}$ will be chosen for the fabrication of bifacial n-type solar cells in the next section.

The relative change in efficiency in the investigated range of $\text{N}_2\text{-POCl}_3$ gas flows is about 2 %. With regard to the application this increase is significant. The following remark might help the reader, who is unfamiliar with efficiencies of industrial solar cells: The development of a selective emitter for p-type solar cells, which was a major topic of research for around one decade, yielded a similar gain in efficiency.

4.6 Influence of phosphorus doped BSFs on solar cells (experimental results)

This paragraph presents IV measurements of bifacial n-type solar cells (Figure 45 b) fabricated according to the process sequence depicted in Figure 45 a). Each data point results from

averaging the results of 4-10 identically processed solar cells. The error bars represent the random errors, since for this investigation the relative differences between the values are of importance. For an overview of the absolute errors, please refer to Section 2.5.

The dependence of V_{oc} and FF for $Q_{POCl_3}=0, 200$ and 300 sccm is depicted in Figure 52. As in Section 4.3 Q_{POCl_3} denotes the N_2 - $POCl_3$ gas flow during the second deposition phase of the high temperature process.

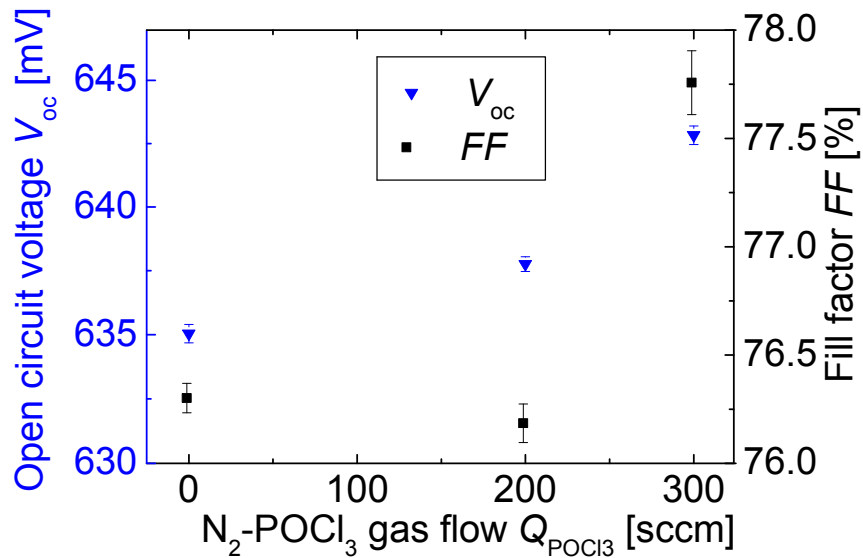


Figure 52: Open circuit voltage V_{oc} and fill factor FF of bifacial n-type solar cells over the N_2 - $POCl_3$ gas flow in the second deposition phase Q_{POCl_3} . Error bars represent the standard deviation of the average value obtained from averaging 5 samples per data point.

V_{oc} increases with increasing Q_{POCl_3} from 635 to 643 mV. This increase of (1.2 ± 0.1) % relative corresponds to a change in J_0 of $-(116 \pm 13)$ fA/cm². The fill factor FF remains constant within measurement accuracy for $Q_{POCl_3}=0$ and 200 sccm and then increases from 76.3 to 77.8 %. This corresponds to a relative increase of (2.0 ± 0.2) %.

Figure 53 presents J_{sc} and efficiency η for bifacial n-type solar cells as a function of the N_2 - $POCl_3$ gas flow Q_{POCl_3} during the second deposition phase of the co-diffusion process. J_{sc} increases with increasing Q_{POCl_3} from 38.5 mA/cm² to 38.7 mA/cm², which is a relative increase of (0.6 ± 0.3) %. This increase is smaller than the change in V_{oc} and FF by a factor of approximately 2 respectively 3 and was neglected in the analytical model.

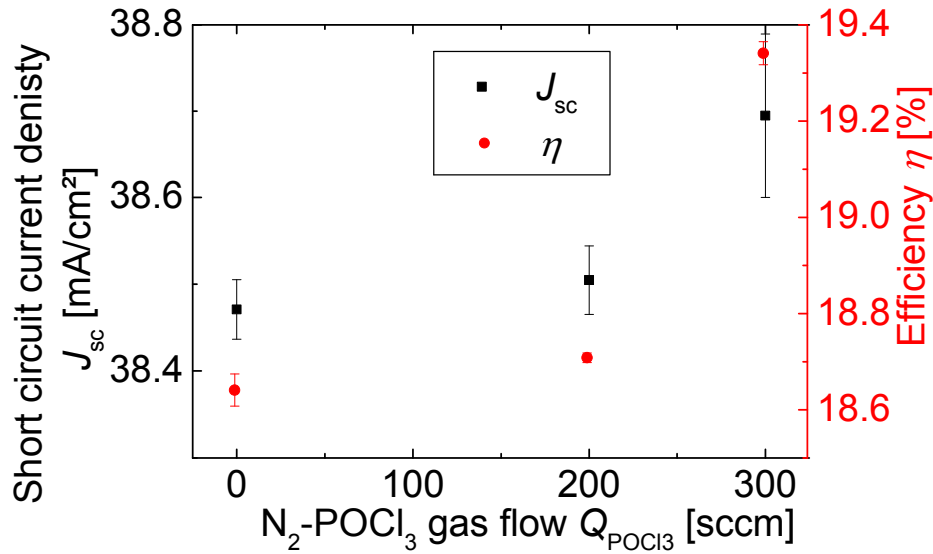


Figure 53: Short circuit current density J_{sc} and efficiency η of bifacial n-type solar cells over the $\text{N}_2\text{-POCl}_3$ gas flow in the second deposition phase Q_{POCl_3} . Error bars represent the standard deviation of the average value obtained from averaging 5 samples per data point.

Following the trend in J_{sc} , V_{oc} and FF the efficiency increases from $Q_{\text{POCl}_3}=0$ sccm to 300 sccm from 18.6 to 19.3 % which is a relative increase by $(3.6 \pm 0.2)\%$

Table 6: IV parameters of bifacial solar cell measured at Fraunhofer ISE Callab PVCells. The parallel resistance is determined using the industrial cell tester.

Measurement	J_{sc} [mA/cm ²]	V_{oc} [mV]	FF [%]	η [%]	R_{p} [k Ω cm ²]
Callab: black non conductive chuck	38.8±1.0	642±3	77.6±0.8	19.3±0.6	11.0±0.1
Callab: gold coated conductive chuck	39.2±1.0	641±3	77.7±0.8	19.5±0.6	11.0±0.1
Industrial cell tester	39.1±1.0	641±5	77.9±0.8	19.5±0.6	11.0±0.1

In order to allow for (future) comparison of the results with those obtained by other research groups one solar cell is measured by the certified calibration laboratory Fraunhofer ISE Callab. Table 6 also shows IV data obtained using the same industrial IV tester that provided the results presented in Figure 52 and Figure 53. All results presented in Table 6 agree within the given absolute measurement accuracy, which is twice the standard deviation. The difference

in J_{sc} and FF introduced by using different measurement chucks are of the same magnitude as observed by Boscke et al. [122]. Recently improvements of the metallization process, especially double print on the solar cell's front and rear side resulted in co-diffused bifacial n-type solar cells with a peak efficiency of 19.9 %. More details will be published elsewhere.

4.7 Discussion: Influence of phosphorus doped BSFs on solar cells

This paragraph discusses the impact of the N_2 - $POCl_3$ gas flow Q_{POCl_3} , which influences the doping profile of the back surface field (Section 3.2), on the IV parameters and the efficiency of bifacial solar cells.

As qualitatively predicted by the simulations presented in Figure 50 for an increase in Q_{POCl_3} from $Q_{POCl_3}=0$ to 300 sccm the efficiency η rises. This rise is caused by an increase of V_{oc} and FF and J_{sc} . Since η is proportional to the product of V_{oc} , J_{sc} , and FF and the relative increases are small, the change in efficiency is approximately equal to the sum of the relative increases of the IV-parameters. The increase in FF thus amounts for about 51 % of the rise in efficiency, while the increase in V_{oc} causes 33 % and in J_{sc} contributes 15 % to the rise in efficiency.

This increase in IV parameters for higher Q_{POCl_3} correlates with an increase in doping concentration (compare Figure 46 a). While the increase in FF due to higher doping concentrations is expected and has been reported frequently in literature [85,127], the increase in V_{oc} is unexpected for the following reason: To this point one successful approach for increasing the open circuit voltage was the development of so called "higher ohmic" emitters. This refers to decreasing the phosphorus doping concentration. Thus decreasing the doping concentration increased V_{oc} and thus cell efficiency. For screen printed contacts this decrease in phosphorus concentration was limited by an abrupt increase in specific contact resistance though, if the doping concentration fell below a certain threshold. Thus one major area of research was the development of screen printing pastes, which allow for low specific contact resistances on lowly phosphorus doped surfaces. The results presented in Sections 4.3- 4.6 implicate that this approach is only successful for doping profiles with relevant concentrations of inactive phosphorus. A further decrease in doping concentration reduces Auger recombination, but also decreases shielding, e.g. of the metal contacts as well as the passivation (compare Section 4.4.2) and thus causes a decrease in V_{oc} . With respect to the development of screen printing pastes, the results presented above suggest that the aim

for the development of new screen printing pastes needs to be not only low specific contact resistances, but also low surface recombination at the metal contacts.

The increase in J_{sc} corresponding to a change in Q_{POCl_3} from 0 to 300 sccm cannot be explained by a change in free carrier absorption, since the higher doping concentration results in higher J_{sc} . One possible cause for the increase in J_{sc} is the increase in V_{oc} , which is amongst others caused by a reduction in $J_{0pass,BSF}$. Including the effect of free carrier absorption and using the change in V_{oc} and the respective doping profiles as input parameters for the software PC1D [128, 129] a relative increase in J_{sc} of 0.2% is calculated. This is close to the experimentally obtained increase of (0.6 ± 0.3) %. One possible reason for the remaining difference between experimental and calculated data, is the use of values that are spatially averaged over the wafer. Thus non-linear effects are neglected. Also the doping profiles used as input parameters are determined on planar surfaces, while the cell features textured surfaces.

In the following the results from the model introduced in Section 4.2.2 are compared to experimental data. When comparing experimental results with predictions of the theoretical model, the theoretical model underestimates the changes in FF and η , while the results for V_{oc} describe the experimental data better. The experimental data shows an increase in V_{oc} from $Q_{POCl_3}=0$ to 300 of (7.8 ± 0.5) mV. The model predicts a change of 7 mV, which agrees well with theory. A further increase in the accuracy of the model could be achieved by directly measuring $J_{0met,BSF}$, instead of calculating this value from the doping profile.

Also the experimentally determined relative change in FF of (1.5 ± 0.2) % is underestimated by the theoretically predicted value of 0.9 %. This underestimation might have multiple causes. One possible cause is that the experimental values that determine FF are distributed very inhomogeneously over the wafer surface. For $Q_{POCl_3}=0$ sccm the specific contact resistance varies between 6 and 38 $m\Omega cm^2$ over the wafer. This variation in the specific contact resistance leads to "local" fill factors from 73.5% to 77.0%. For the simulation an average value of ρ_c , which results from 4 measurement spots, of 11 $m\Omega cm^2$ is used and results in a fill factor of 76.5%. Since the influence of ρ_c on the fill factor is nonlinear, but for the averaging of the sheet resistance each value was weighted equally, a discrepancy in the results may be expected. Nonlinear effects of the contact resistance on the fill factor were also observed by Greulich et al. [130].

An uncertainty based in the model is the assumption of lateral current conduction in the base, which was used, since no analytical model exists. The error of this assumption increases with decreasing sheet resistance, but also in this case a quantitative estimate of the error is

difficult (compare Appendix C). Thus it is assumed that discrepancies concerning the fill factor between the model and the experimental data are due to uncertainties in the input data, rather than the model itself.

4.8 Modelling the impact of the phosphorus doped BSF on cell efficiency

One main aim of this section is to connect single electric properties of the BSF (R_{sh} , $J_{0pass,BSF}$, $J_{0met,BSF}$, ρ_c) with cell efficiency. For this purpose, simulations are necessary, because experimentally changing only one of these parameters while leaving the others unchanged is extremely difficult. In the following cell efficiency is plotted as a function of two of the four parameters R_{sh} , $J_{0pass,BSF}$, $J_{0met,BSF}$, and ρ_c . As an example how the respective x and y coordinates

Table 7: Input parameters for the model calculation in Section 4.8. For the following figures one parameter is varied while the other two are kept at the displayed value. A complete list of input parameters is provided in Appendix B.

$J_{0met,BSF}$ [fA/cm ²]	ρ_c [m Ω cm ²]	R_{sh} [Ω /sq]
706	3.6	70.4

may be linked experimentally the data pairs resulting from a variation in Q_{POCl_3} (Section 4.3) are added to the graphs. The aim is to suggest some rough approximations that might help the researcher when tuning high temperature processes for the formation of phosphorus doped BSFs. Based on the discussion presented in Section 4.7, the error margin of these rules of thumb are expected to be between 10 and 50 %. Nevertheless, in the author's opinion, the current absence of any quantitative estimates justifies even very rough approximation.

Analytical calculations are performed using the model and assumptions introduced in Section 4.2.2. In the following figures calculated values for cell efficiency and rear side finger pitch are presented. These values are plotted over the dark saturation current density of the passivated part of the BSF $J_{0pass,BSF}$ and one of the following three parameters: the dark saturation current density of the metalized part of the BSF $J_{0met,BSF}$, the specific contact resistance of screen printed contacts on the BSF ρ_c or the sheet resistance of the BSF R_{sh} . If any of the parameters is constant, the values depicted in Table 7 are used. Since a common property to characterize a BSF is its sheet resistance, Figure 54 presents the influence of sheet resistance R_{sh} and dark saturation current density in the passivated area $J_{0pass,BSF}$ on the

efficiency of a bifacial n-type solar cell (Figure 45 b). For each data pair of R_{sh} and $J_{0pass,BSF}$ the rear side finger pitch is adapted for maximum efficiency.

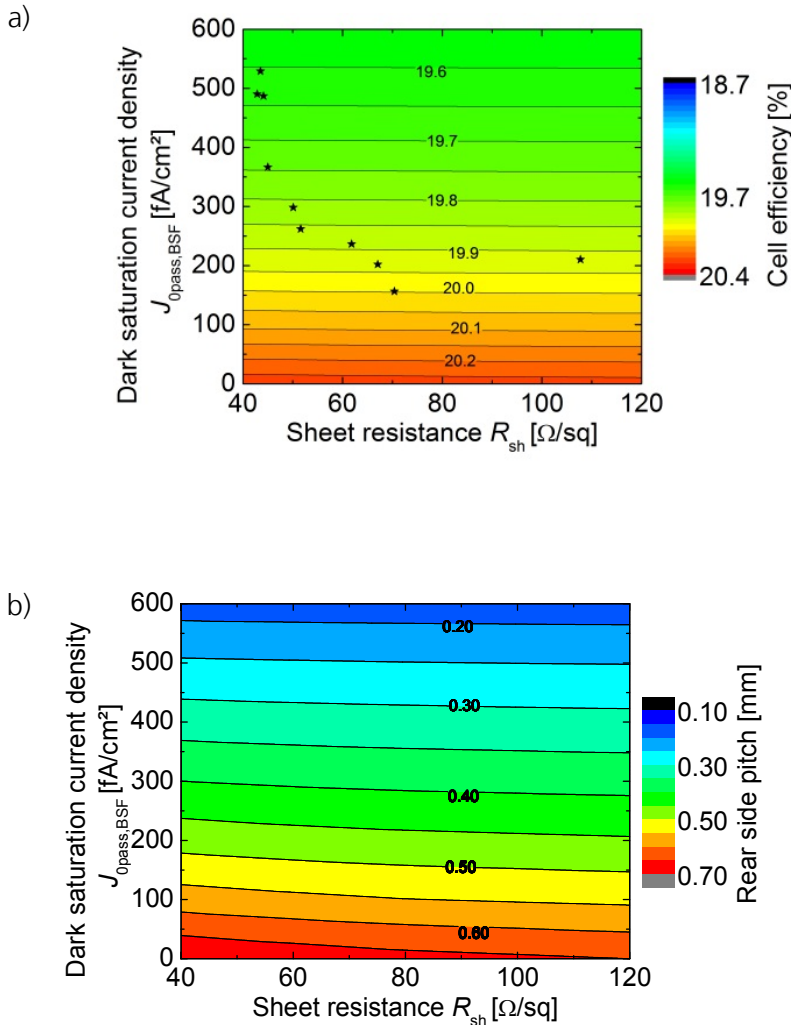


Figure 54: Simulated cell efficiency over $J_{0pass,BSF}$ and R_{sh} for constant $J_{0met,BSF}$ and ρ_C . The rear side finger pitch is adjusted for maximum efficiency. Symbols represent experimental data. b) Optimum rear side finger pitch over $J_{0pass,BSF}$ and R_{sh} for constant $J_{0met,BSF}$ and ρ_C . Please note that the scale in Figure 54 a), Figure 55, and Figure 56 is chosen identically in order to simplify comparison of the data.

Figure 54 a) points out that while a change in $J_{0pass,BSF}$ has a large influence on cell efficiency the influence of sheet resistance on cell efficiency is comparatively small. In order to understand the small influence of R_{sh} on efficiency Figure 54 b) shows the corresponding finger pitch of the screen printed metallization on the BSF. For an increase in R_{sh} the pitch decreases and thus compensates the loss in conductivity. Thus as long as silver consumption is not an issue, no light is incident on the cells' rear side and base resistivity is sufficiently low

4.8 Modelling the impact of the phosphorus doped BSF on cell efficiency

(in this case $1.5 \Omega\text{cm}$), the high temperature process should be optimized for minimum $J_{0\text{pass,BSF}}$ without considering the change in sheet resistance. One way to decrease $J_{0\text{pass,BSF}}$ is to decrease BSF doping thus reducing surface and Auger recombination. Unfortunately this decreases surface shielding and increases the dark saturation current density $J_{0\text{met,BSF}}$ of the metalized area. To quantify the trade-off between decreased recombination in passivated areas and increased recombination under the metal contacts Figure 55 presents the influence of $J_{0\text{pass,BSF}}$ and $J_{0\text{met,BSF}}$ on cell efficiency.

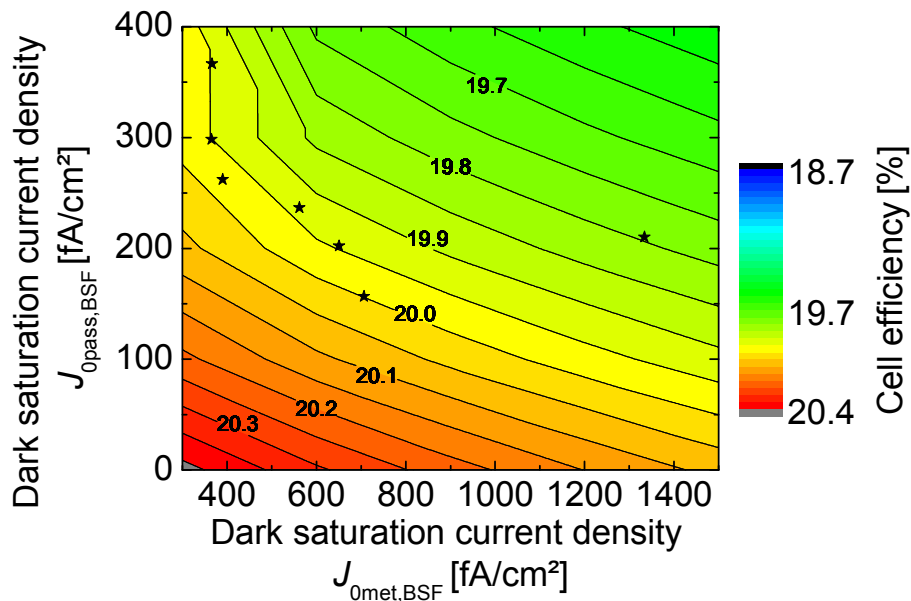


Figure 55: Calculated cell efficiency over $J_{0\text{met,BSF}}$ and $J_{0\text{pass,BSF}}$. Symbols represent experimental data.

For the theoretical case of $J_{0\text{pass,BSF}} > J_{0\text{met,BSF}}$ (upper left corner of Figure 55) the efficiency is only dependent on $J_{0\text{met,BSF}}$, since the whole rear side is metalized. Beyond this area both a decrease in $J_{0\text{pass,BSF}}$ and $J_{0\text{met,BSF}}$ increases efficiency. In this case the lines of constant efficiency allows for quantification when a change in the dark saturation current density in the passivated area ($\Delta J_{0\text{pass,BSF}}$) is compensated by an increase in the dark saturation current density in the metalized area ($\Delta J_{0\text{met,BSF}}$). More concretely, for $6 \times \Delta J_{0\text{pass,BSF}} \approx -\Delta J_{0\text{met,BSF}}$ cell efficiency stays constant. When taking a look at the experimental values in Figure 55, it seems that in general $|6 \times \Delta J_{0\text{pass,BSF}}| \gg |\Delta J_{0\text{met,BSF}}|$ holds. Thus the influence of $J_{0\text{pass,BSF}}$ dominates over the influence of $J_{0\text{met,BSF}}$ and a decrease in $J_{0\text{pass,BSF}}$ leads to an increase in cell efficiency. So again $J_{0\text{pass,BSF}}$ is the parameter of choice for increasing cell efficiency.

The next paragraph discusses the trade-off between recombination and specific contact resistance. Qualitatively this trade-off is simple. A decrease in (surface) doping concentration generally decreases recombination and increases contact resistance, which increases V_{oc} and decreases FF . A quantitative understanding of this relation is more complex though.

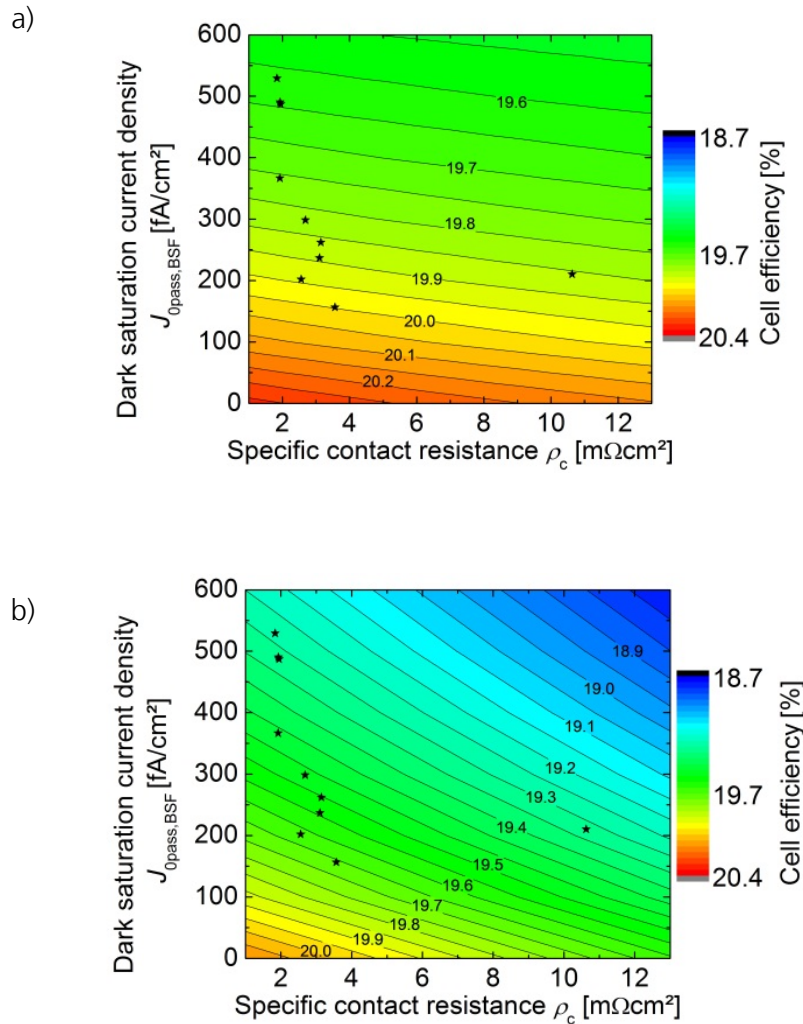


Figure 56: a) Cell efficiency over $J_{0pass,BSF}$ and ρ_c for constant R_{sh} and $J_{0met,BSF}$. Please note that the rear side finger pitch is different for each combination of $J_{0pass,BSF}$ and ρ_c . Symbols represent experimental data. b) Cell efficiency over $J_{0pass,BSF}$ and ρ_c for constant R_{sh} , $J_{0met,BSF}$ and a constant pitch of 1.9 mm. Symbols represent experimental data from Section 4.3.

Figure 56 a) presents cell efficiency over $J_{0pass,BSF}$ and ρ_c . As expected a decrease in both $J_{0pass,BSF}$ and ρ_c increases cell efficiency. Quantitatively the lines of constant efficiency are

characterized by $\Delta J_{0\text{pass,BSF}}/(fA/cm^2) \approx -6.5 \Delta \rho_c / (m\Omega cm^2)$. Please note that this relation only holds if the rear side finger pitch is adapted for maximum efficiency. More specific, the finger pitch applied in Figure 56 a) varies between 0.1 and 0.8 mm, which is not an option in industrial production. If cost is important, the finger pitch cannot be varied at will, but needs to be as high as possible to minimize silver consumption. In order to factor this in, Figure 56b) shows cell efficiency calculated from the same input parameters as used in Figure 56 a).

The difference is that the finger pitch in Figure 56 b) is set at a constant value of 1.9 mm, which is comparable to front side metallization of p-type solar cells. When comparing Figure 56 a) and b) it becomes clear that for low $J_{0\text{pass,BSF}}$ and ρ_c the difference in efficiency is $\sim 0.2\%$ absolute while for high $J_{0\text{pass,BSF}}$ and ρ_c the difference in efficiency of $\sim 0.8\%$ absolute is larger. This means that for high efficiencies the optimum rear side finger pitch of bifacial solar cells approaches the front side finger pitch of a p-type solar cell.

These figures may also serve for comparing cell efficiencies. As a very rough rule of thumb one may assume a maximum loss in efficiency of 0.2-0.3 % absolute for solar cells with efficiencies around 20 % when changing from a rear side grid that is optimized for maximum cell efficiency to a rear side grid that is similar to the front side grid of a p-type cell. A third interesting fact is that the slope of the lines of constant efficiency in Figure 56 b) is different from those in Figure 56 a). For high efficiencies the lines of constant efficiency in Figure 56 b) may be described by $\Delta J_{0\text{pass,BSF}}/(fA/cm^2) \approx -18 \Delta \rho_c / (m\Omega cm^2)$. Thus for a fixed finger pitch of 1.9 mm the slope changes roughly by a factor of 3 compared to Fig. 7 with a variable pitch. When looking at the experimental data it follows again that a reduction in $J_{0\text{pass,BSF}}$ in general leads to an increase in cell efficiency. The only exception being the data point at $J_{0\text{pass,BSF}} \approx 200 fA/cm^2$ and $\rho_c \approx 11 m\Omega cm^2$. Combining the findings from all figures it follows that a promising approach for a further increase in cell efficiency is the reduction of $J_{0\text{pass,BSF}}$.

4.9 Relevance of obtained cell efficiencies

This section briefly gives an overview of (recent) results concerning co-diffused bifacial solar cells and shows the relevance of the present work. In 2011, two weeks after the beginning of this thesis, results for bifacial n-type solar cells with maximum efficiencies of 13.8 % fabricated by a $POCl_3$ based co-diffusion were published by Bazer-Bachi et al. [105], which served as a proof-of-concept for $POCl_3$ based co-diffusion. The solar cells were produced using a $POCl_3$ based co-diffusion process and a BSG layer deposited by plasma enhanced chemical vapor deposition. In 2014 Frey et al. reached efficiencies of 19.7 % for bifacial solar

cells produced by co-diffusion, but providing little details about the used process sequence [131]. Recently cell efficiencies of 19.7 % were reached also using a BSG layer deposited by PECVD in a POCl_3 based co-diffusion process [132]. Concerning the number of process steps the process sequence is comparable to the process sequence developed in this thesis. Recently bifacial solar cells with a rear side boron emitter and peak efficiencies of 18.8 % were presented using co-diffusion from a POCl_3 based atmosphere and a BSG layer deposited by APCVD [133]. To the author's knowledge the peak efficiency of 19.9% reached in this thesis is currently the highest efficiency reached for a bifacial n-type solar cell produced using a POCl_3 based co-diffusion process and doped layers deposited by APCVD. Concerning device performance this result proves that doped layer deposition by APCVD is a feasible alternative to PECVD based layers for co-diffusion processes.

In order to further assess the relevance of this work, in the following results concerning economic aspects of the cell process developed in this thesis are briefly presented. Internal cost calculations using the tool SCost [134], show that the process sequence developed in this thesis decreases the cost of the cell process for each wafer by approximately 17 % compared to "state of the art" sequential diffusion using PECVD based diffusion barriers. The absolute cost of the developed cell process is comparable to p-type passivated emitter and rear cell (PERC) technology. Since bifacial n-type solar cells have a higher monofacial efficiency potential (about 1% absolute) and additionally allow for a higher energy yield due to bifaciality this cell concept in combination with the process sequence developed in this thesis is from the author's point of view potentially superior to current technology. Before the industrial implementation of co-diffused bifacial solar cells two problems need to be solved though: One is the high wafer price of n-type wafers compared to p-type wafers, which is mainly due to economies of scale. The second possible hurdle are high currents under reverse bias, which were observed in this thesis and also for other process sequences [17]. For conventional module integration using bypass diodes the measured currents of 5 mA/cm² at a reverse bias of -12 V are more than an order of magnitude too large. Depending on the local distribution of these reverse currents, they might allow for the use of modules without bypass diodes. Such a substitution of bypass diodes was e.g. proposed for metal wrap through solar cells [135, 136]. In how far the solar cells developed in this thesis fulfill the requirements for module integration is a topic which is still under investigation.

4.10 Summary

This chapter investigates the influence of Q_{POCl_3} on the electrical parameters of the BSF. Based on this investigated bifacial solar cells with peak efficiencies of 19.9 % are fabricated, using

an industrially feasible process sequence. This signifies a reduction of 2-3 process steps compared to state of the art processing, while maintaining the same efficiency, which makes these results extremely relevant for application. It was also demonstrated for the first time that co-diffusion processes with doped layers deposited by APCVD allow for the fabrication bifacial solar cells. A quantitative investigation of the influence of the BSF on cell efficiency reveals that decreasing the surface doping concentration only increases cell efficiency for doping profiles with relevant quantities of inactive phosphorus. Concerning future improvements in cell efficiency $J_{0\text{pass,BSF}}$ is identified as the parameter that allows for the largest increase in efficiency.

5 Impact of surface near doping concentration on specific contact resistance

5.1 Introduction

Screen printed silver based thick film metallization is the most widespread technique for contacting phosphorus-doped surfaces of industrial silicon solar cells. Even though screen printed metallization has been used for many decades in the photovoltaic industry, neither the mechanism of current conduction nor contact formation between the silver fingers and busbars and the doped silicon is understood completely. Concerning current conduction various models exist, of which the following two are currently proposed to be the most relevant: One model assumes direct current flow from the doped region via silver crystallites into the bulk finger [137, 138], whereas the second model suggests a multi-step tunnelling process through an insulating glass layer that separates the silicon surface from the bulk contact finger [139, 140]. According to the second model small silver colloids embedded in the glass film mediate current conduction through this glassy layer. Regarding contact formation, most research has traditionally been focused on the influence of paste composition and sintering parameters on the microstructure of the contacts [141, 142]. Recently, the interaction of the phosphorus-doped areas and the metallization has moved into the center of attention. Several authors [32, 143, 144] published that a decrease in the inactive phosphorus concentration leads to an increase in specific contact resistance. By comparison little research has been performed on contact formation on textured surfaces for phosphorus doping levels below 10^{20}cm^{-3} , since historically it has been difficult to achieve specific contact resistances that are suitable for the application in solar cells [143]. According to Kulushich et al. [144] contact formation in the absence of inactive phosphorus does not allow for a contact resistance that is appropriate for solar cell application, since no crystallites form at the silicon surface. In contrast Schubert [143] reported crystallite formation on planar surfaces without inactive phosphorus and recently crystallite formation has been reported on textured silicon surfaces “without P doping” [32], but in this case it is unclear to which extent the contact resistance is affected. This paragraph investigates the influence of the surface

doping concentration on the specific contact resistance. Directed manipulation of the doping profile is achieved using the high temperature processes developed in Chapter 3. A shortened version of this chapter was recently submitted for publication [145].

5.2 Experiment

As substrate material for the characterization of the contacts phosphorus doped $156 \times 156 \text{ mm}^2$ Czochralski (Cz) grown silicon wafers with a base resistivity of $3 \Omega\text{m}$ are used. After an alkaline texturing process the wafers are subjected to a POCl_3 based high temperature process in a tube furnace that allows for a controlled manipulation of the doping concentration by using two deposition phases[78][78]. As in Chapter 4 the N_2 - POCl_3 gas flow in the second deposition phase is varied. The phosphosilicate glass layer resulting from the high temperature process is removed in diluted hydrofluoric acid. In order to simulate a conventional solar cell process, the surface is subsequently passivated by a SiN_x layer deposited by plasma enhanced chemical vapor deposition. The contact grid is screen printed onto the SiN_x layer. The paste is a commercially available screen printing paste (Sol9610A by Heraeus Precious Metals GmbH & Co. KG), which is fired in an inline conveyor belt furnace for contact formation. All samples are fired at the same set point peak firing temperature and belt speed. Contact properties are observed by transfer length method (TLM) measurements on 3-5 wafers per N_2 - POCl_3 gas flow. Furthermore the contacts are investigated using scanning electron microscopy (SEM) after wet chemical removal of i) the bulk silver finger in HNO_3 -based solution (69 %) for 10 minutes at 90°C and ii) the glassy layer in diluted hydrofluoric acid (5 %) for 1 min at room temperature. From these SEM pictures the area coverage of imprints is extracted in the following manner. Imprints are selected by visual inspection according to two criteria. The first one is contrast, this means that the imprints are "darker" than the surrounding silicon. The second criterion is that imprints feature a certain structure, which is caused by the previous presence of silver crystallites. The area coverage of imprints is calculated as the total number of pixels associated with imprints divided by the total number of pixels in the SEM picture. Electrochemical capacitance voltage (ECV) measurements extract the active doping concentration of the phosphorus doped area in the center position of planar saw damage etched $156 \times 156 \text{ mm}^2$ wafers.

5.3 Results

Figure 57 presents selected ECV measurements of the surface near doping concentration. The change in doping concentration is reached by varying the N_2 - $POCl_3$ gas flow Q_{POCl_3} during the second deposition phase, while leaving the N_2 - $POCl_3$ gas flow during the first deposition phase constant.

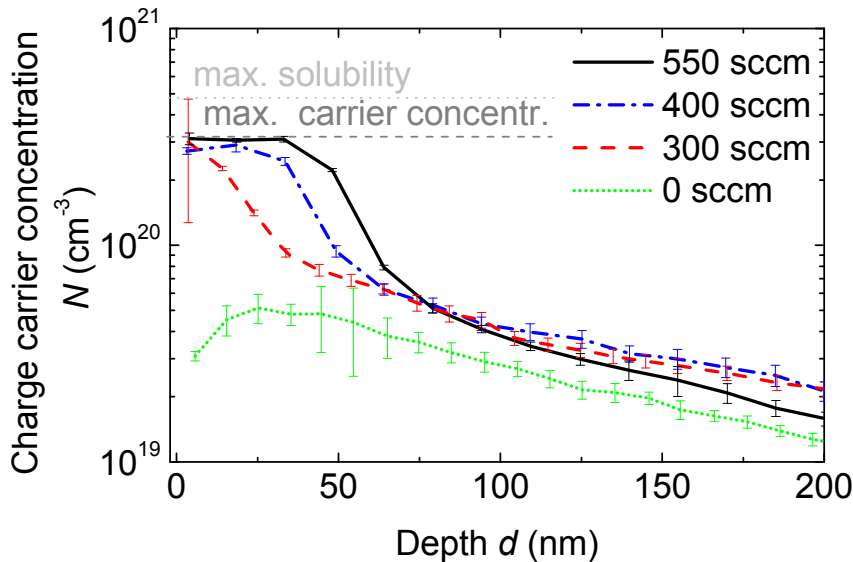


Figure 57: Surface near charge carrier concentration determined by ECV denominated by their N_2 - $POCl_3$ gas flow Q_{POCl_3} during the second deposition phase measured on planar reference samples. The error bars represent the measurement accuracy of a single ECV measurement. Maximum solubility of phosphorus in silicon and maximum carrier concentration are determined according to reference [30].

The doping profile for $Q_{POCl_3}=0$ sccm features a maximum carrier concentration of $5 \times 10^{19} \text{ cm}^{-3}$ indicating the absence of inactive phosphorus. An increase in Q_{POCl_3} to 300 sccm leads to the doping profile with a maximum carrier concentration of $3 \times 10^{20} \text{ cm}^{-3}$, which is the maximum active carrier concentration resulting from phosphorus doping in silicon for the applied temperature after Solmi et al. [30]. The remaining doping profiles, resulting from a further increase in Q_{POCl_3} feature a plateau of constant charge carrier concentration close to the surface with a concentration that agrees well with the activation limit [30]. Corresponding to the increase in Q_{POCl_3} from 300 over 400 to 550 sccm the length of the plateau increases from < 7 nm over 38 to 51 nm.

Figure 58 presents representative SEM images of contacted areas. For the following SEM measurements, first the bulk silver finger and thus also crystallites in direct contact with the

bulk silver finger are removed. Subsequently the glassy layer is also removed. Imprints stemming from crystallites in direct contact are thus uncovered[146], while imprints from crystallites without direct contact are still covered by crystallites. Any remaining crystallites were originally separated from the bulk silver finger by a glassy layer. Each SEM picture is denoted by the respective Q_{POCl_3} of the high temperature process and the specific contact resistance of the contact finger under investigation, as well as the position of the sample on the wafer. The specific contact resistance of $37 \text{ m}\Omega\text{cm}^2$ depicted in (a) belongs to the doping profile with a maximum surface concentration of $5 \cdot 10^{19} \text{ cm}^{-3}$, while $\rho_c = 1.6 \text{ m}\Omega\text{cm}^2$ depicted in (d) belongs to the doping profile with an active surface doping concentration of $3 \cdot 10^{20} \text{ cm}^{-3}$ (Figure 57). Please note that the specific contact resistance is not averaged over the wafer but extracted from two neighboring fingers around the finger that is investigated by SEM. Of major interest are the area coverage and the position of imprints and silver crystallites.

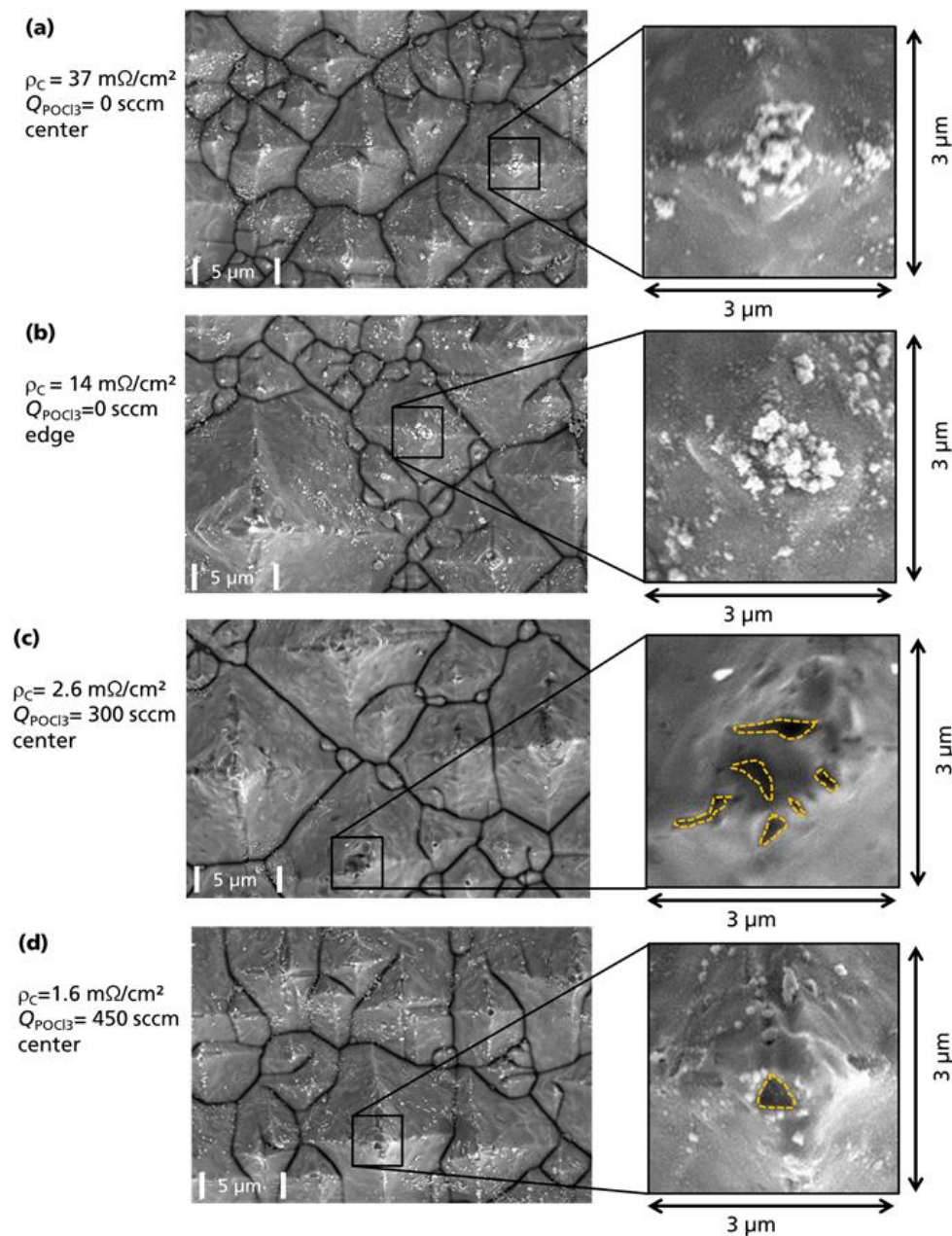


Figure 58: Scanning electron microscopy (SEM) images of screen printed and fired silver contacts on alkaline textured silicon surfaces after removal of the bulk silver and subsequently of the remaining glassy layer. The areas regarded as “imprints” are encircled by a dashed yellow line. The pictures are denominated by their specific contact resistance, the $\text{N}_2\text{-POCl}_3$ gas flow Q_{POCl_3} of the underlying high temperature process and the position of the sample on the wafer.

For $Q_{\text{POCl}_3} = 0 \text{ sccm}$ the highest specific contact resistances of $37 \text{ m}\Omega\text{cm}^2$ (a) and $14 \text{ m}\Omega\text{cm}^2$ (b) are observed. At both positions the pyramid tips as well as the faces are covered with

silver crystallites, while only very few imprints are observed. In contrast, the two samples with $Q_{\text{POCl}_3} = 300$ sccm (c) and $Q_{\text{POCl}_3} = 450$ sccm (d) exhibit a lower specific contact resistance of $2.6 \text{ m}\Omega\text{cm}^2$ and $1.6 \text{ m}\Omega\text{cm}^2$, respectively. The corresponding SEM images reveal more imprints mainly located at pyramid tips, but a similar amount of crystallites at the pyramid faces. Qualitatively, a high coverage of imprints correlates with a low specific contact resistance. The SEM images also show that the doping profile without inactive phosphorus ($Q_{\text{POCl}_3} = 0$ sccm) still allows for crystallite formation. However, for the doping profile without inactive phosphorus ($Q_{\text{POCl}_3} = 0$ sccm) fewer imprints are observed compared to doping profiles with inactive phosphorus e.g. $Q_{\text{POCl}_3} = 450$ sccm.

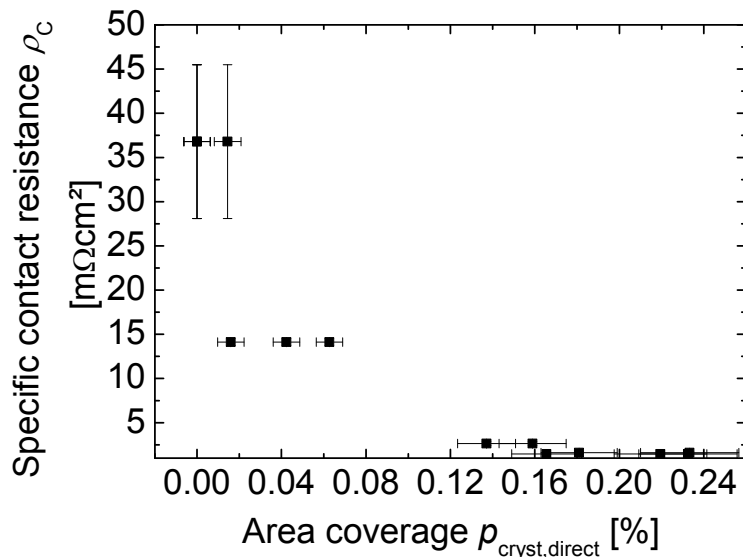


Figure 59: Specific contact resistance ρ_c over area coverage of imprints $p_{\text{cryst,direct}}$ extracted from SEM images (Figure 58). The errors bars of the specific contact resistance ρ_c represent the errors of a single TLM measurement. The errors in the area coverage result from the experimental uncertainty in the extraction of $p_{\text{cryst,direct}}$.

A quantitative evaluation of the SEM images allows for a correlation between the area coverage of imprints $p_{\text{cryst,direct}}$ and the specific contact resistance (Figure 59). The error in ρ_c results from uncertainties in the TLM measurement, while the error in $p_{\text{cryst,direct}}$ results from uncertainties in the manual extraction of the imprint area coverage. As observed in Figure 59 a decrease in ρ_c correlates with an increase in the area coverage of imprints $p_{\text{cryst,direct}}$. Specific contact resistances between 37 and $1 \text{ m}\Omega\text{cm}^2$ are associated with values of $p_{\text{cryst,direct}}$ between 0 and 0.24% .

5.4 Discussion and Modelling

This section first discusses the carrier concentration and then the SEM images presented in Section 5.3. For further discussion it is important, which Q_{POCl_3} results in doping profiles that feature a nonzero concentration of inactive phosphorus (Figure 57). Here it is important to know that doping profiles are generally determined on planar surfaces, while contact formation is investigated on textured surfaces. According to Wagner et al. [147], doping profiles on planar and textured surfaces resulting from the same high temperature process do not necessarily need to be same, one reason being the local variation in the doping profiles on textured surfaces, where the highest concentrations are at the pyramid tips.

With regard to the doping profile resulting from a high temperature process with $Q_{\text{POCl}_3}=0$ sccm no inactive phosphorus is present on planar surfaces since the carrier concentration is well below its maximum value. With regard to textured surfaces, even when considering an inhomogeneous distribution of the dopant [147], no inactive phosphorus is expected to be present at the pyramid tips.

For the doping profile resulting from $Q_{\text{POCl}_3}= 300$ sccm, it is not clear if inactive phosphorus is present or not. Inactive phosphorus consists of mobile phosphorus for concentrations of $3 - 5 \times 10^{20} \text{cm}^{-3}$ and immobile SiP precipitates for concentrations larger than $5 \times 10^{20} \text{cm}^{-3}$ [30]. This means that for $Q_{\text{POCl}_3}= 300$ sccm no precipitates but only mobile inactive phosphorus is present for planar surfaces. The sheet resistance of the textured sample is higher than on the planar surface by a factor of roughly 1.5. Thus if the doping concentration of the textured wafer was homogeneous no inactive phosphorus would be expected. Since the local doping concentration on pyramid tips may be higher compared to planar surfaces [147], precipitate formation on pyramid tips may be neither excluded nor confirmed. For the high temperature processes resulting from Q_{POCl_3} larger than 300 sccm a plateau of constant carrier concentration forms. Such a plateau has been observed frequently and involves the presence of inactive phosphorus [31]. It is well known that an increase in Q_{POCl_3} not only increases the active phosphorus concentration, which is presented in Figure 57, but also the concentration of inactive phosphorus [124]. Since similar for $Q_{\text{POCl}_3}= 550$ sccm the sheet resistance on planar and textured surfaces is (Figure 47) at least at the pyramid tips inactive phosphorus is present. In summary, an increase in Q_{POCl_3} leads to an increase in the concentration of inactive phosphorus for both planar and textured surfaces. For $Q_{\text{POCl}_3}=0$ sccm the inactive phosphorus concentration on both surfaces is expected to be zero while for 550 sccm the concentration is nonzero.

The imprints observed in Figure 58 are comparable in size and location to those observed by Cabrera et al [137] and Kontermann et al. [148] and are attributed to crystallites that have been in direct contact with the bulk silver finger. Thus, in order to facilitate a discussion of the microstructure, in the following we refer to “imprints” as “crystallites in direct contact with the bulk finger” and denote their area coverage as $p_{\text{cryst,direct}}$. The observed decrease in the specific contact resistance with $p_{\text{cryst,direct}}$ has been observed before and was proposed by Ballif et al. [138]. As discussed above the increase in $p_{\text{cryst,direct}}$ correlates with an increase in Q_{POCl_3} , which correlates with an increase in the concentration of inactive phosphorus. A possible explanation is that a reduction of structural defects caused by a reduction of the inactive phosphorus concentration decreases crystallite size [32], which increases the probability that crystallites are separated from the bulk finger by a glassy layer.

The observation of imprints on surfaces without inactive phosphorus (Figure 58) is in contrast to results for lower doping concentrations obtained by Kulushich et al. [144], but in line with results by Cabrera et al. [32]. One possible reason might be the use of paste with different compositions. A conclusive argumentation is difficult, since for both publications the names of the used pastes are not given. Thus, in summary the observations in Section 5.3 are qualitatively in line with other publications.

In the following paragraph the data from Figure 59 is discussed quantitatively. To simplify the discussion Figure 60 presents the inverse of the specific contact resistance ρ_c^{-1} as a function of the area coverage of crystallites in direct contact with the bulk finger $p_{\text{cryst,direct}}$. Each data point results from averaging 2-4 samples. As discussed above, an increase in $p_{\text{cryst,direct}}$ correlates with a decrease in ρ_c meaning an increase in ρ_c^{-1} . In the following a quantitative description of the data is presented assuming different models for current conduction, based on the common assumption that both the conductivity of the bulk silver finger and the crystallite both do not contribute relevantly to the specific contact resistance [137]. Additionally a possible influence of the active doping concentration on the specific contact resistance of a single crystallite [62] is neglected. One reason is that during the firing process the silicon melts and then recrystallizes with an unknown doping concentration. The second reason is that even if the newly formed concentration of the dopant was known, it is still unclear how the current flows from the contact into the silicon wafer, especially at which depth.

If current conduction occurs only directly and vertical current flow towards the contact is assumed, ρ_c and $p_{\text{cryst,direct}}$ are expected to be inversely proportional:

$$\rho_C^{-1} = p_{cryst,direct} / \rho_{C,crystal} \quad (5.1)$$

where the parameter $\rho_{C,crystal}$ represents the specific contact resistance of a single crystallite.

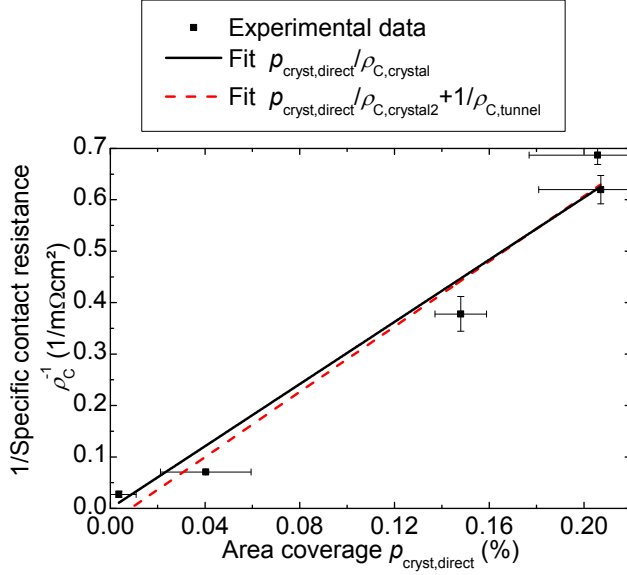


Figure 60: Inverse of specific contact resistance ρ_C^{-1} as a function of area coverage of crystallites in direct contact with the silver finger $\rho_{cryst,direct}$. The errors bars of the specific contact resistance ρ_C represent the errors of a single TLM measurement. The errors in the area coverage represent the standard deviation of the average value extracted from 2-3 measurement locations.

Assuming an additional conduction mechanism characterized by $\rho_{C,2}$ that is independent from both $\rho_{cryst,direct}$ and the underlying change in the phosphorus doping profile, e.g. electron tunneling from the doped area through a glassy layer characterized by $\rho_{C,tunnel}$, means that both current paths form a parallel circuit. This results in

$$\rho_{C,total}^{-1} = \rho_{C,1}^{-1} + \rho_{C,2}^{-1} = p_{cryst,direct} / \rho_{C,crystal2} + 1 / \rho_{C,tunnel} \quad (5.2)$$

Fitting this relation to the data displayed in Figure 60 results in the solid line and yields $\rho_{C,crystal2} = (3.3 \pm 0.3) \mu\Omega cm^2$ and $\rho_{C,tunnel} = (-3 \pm 40) 10^5 \mu\Omega cm^2$ with a corrected R^2 of 0.92. Since $\rho_{C,tunnel}$ is negative this cannot be interpreted as a second conduction mechanism, since the contribution of a second conduction mechanism should be positive. Also the error of $\rho_{C,tunnel}$ is one order of magnitude larger than its absolute value. With regard to solar cells, where specific contact resistances around $1 m\Omega cm^2$ are common, $\rho_{C,tunnel} \leq 10^4 \mu\Omega cm^2$ would

measurably decrease the total contact resistance. Since $\rho_{C,1} \ll \rho_{C,2}$ equation (5.1) is also fitted to the data. This results in the dashed line in Figure 60 and yields $\rho_{C,cystal} = (3.3 \pm 0.2) \mu\Omega\text{cm}^2$ with a corrected coefficient of determination R^2 of 0.92. Thus a model where conduction only occurs via crystallites in direct contact with the bulk finger explains the data well. The extracted specific contact resistance of a single crystallite of $(3.3 \pm 0.2) \mu\Omega\text{cm}^2$ is in the wide range of contact resistance extracted by other authors, which are summarized in reference [149] and agrees well with their theoretically expected values of 3 – 5 $\mu\Omega\text{cm}^2$ [149]. Since the composition of screen printing pastes differs considerably, the contribution of tunneling and direct current conduction might differ for different screen printing pastes. The author believe that the model describing parallel conduction channels (equation (5.2)) and the approach presented above may be broadly applied for quantitatively separating the contributions of tunneling and direct current conduction for different pastes, thus indicating their dominant conduction mechanism.

An important point for future investigation of the imprint coverage is an increase in measurement accuracy. This could be achieved by different approaches. One possible approach is to remove only part of the silver finger, which would allow for detecting the location of crystallites in direct contact with the silicon and the bulk silver. Then these crystallites and the glassy layer could be removed wet chemically exposing the imprints. This could increase the accuracy associating areas with crystallites in direct contact with the bulk silver. This approach is not straight forward though, since the bulk silver finger, does not feature a homogeneous thickness, thus realistically many etching steps would probably be required. A second possibility to increase measurement accuracy could be achieved by extracting the area of one imprint by using a mathematical algorithm which is based on contrast and structure. A third possibility for increasing measurement accuracy would be to characterize imprints not only by their area determined from a top down view, as done in this thesis, but to also consider the orientation of the areas which belong to one imprint.

5.5 Summary

The surface near phosphorus doping level of $3 \cdot 10^{20} \text{cm}^{-3}$ with only a few nm plateau length and thus a low quantity of inactive phosphorus already favors the formation of large crystallites in direct contact with the bulk finger. This is verified by imprints detected in the SEM analysis. From a quantitative relation between the imprint area coverage of these crystallites and the specific contact resistance of the bulk finger the specific contact resistance of a single crystallite of $(3.3 \pm 0.2) \mu\Omega\text{cm}^2$ is extracted. This value agrees well with values predicted by theory. Furthermore we present an approach assuming parallel conduction

paths that allows for quantitatively separating the influence of direct and indirect current conduction. Under the assumption of vertical current flow, a model based on current conduction via crystallites in direct contact with the bulk silver finger allows for an adequate description of the experimental data. In the absence of inactive phosphorus, at doping levels of $5 \cdot 10^{19} \text{cm}^{-3}$ very few imprints but a similar amount of small crystallites is detected that are not in direct contact with the bulk finger.

6 Summary and Outlook

This chapter first gives a brief summary of the main results of this thesis, followed by an outlook concerning further developments of selected aspects.

Summary

This thesis presents the development and characterization of a co-diffusion process from a borosilicate glass (BSG) layer and an atmosphere containing POCl_3 and its application for the fabrication of bifacial n-type silicon solar cells.

Chapter 3 discusses the formation of boron and phosphorus doping profiles in one high temperature step that are adequate for the application in photovoltaics.

Section 3.2 introduces a new method that allows for a controlled manipulation of phosphorus doping profiles, especially the independent manipulation of the surface doping concentration and the depth of the doping profile with unprecedented degrees of freedom. In previously used high temperature processes, changes in surface doping concentration and depth were linked due to Fick's law of diffusion. This link is overcome by the introduction of a second deposition phase.

The influence of the oxygen concentration in the process atmosphere on boron diffusion from a BSG layer deposited by atmospheric pressure chemical vapor deposition is discussed in Section 3.3. The influence of the oxygen concentration in the process atmosphere on boron diffusion is explained by the formation of an intermediate SiO_2 layer that forms at the Si/BSG interface and is confirmed by ellipsometry. The growth of this intermediate layer may be described quantitatively based on an iterative model that uses the parameterization by Massoud et al. [13]. In contrast to thermally grown SiO_2 layers for SiO_x layers deposited by APCVD the growth rate of the intermediate layer is not limited by diffusion of the oxidizing species through the SiO_x layer, but reaction limited independent of the SiO_x layer thickness.

The influence of the atmosphere containing POCl_3 on layers deposited by APCVD is discussed in Section 3.6. Secondary ion mass spectroscopy (SIMS) measurements show that the interaction between POCl_3 and SiO_x layers lead to the formation of a phosphosilicate glass (PSG) layer at the SiO_x /air interface. This behavior is similar to thermally grown SiO_2 layers.

Within measurement accuracy the growth of a PSG layer in SiO_x may be described quantitatively by an existing model.

Chapter 4 treats bifacial n-type solar cells fabricated using co-diffusion.

The high temperature processes developed in Chapter 3 allow for the fabrication of bifacial n-type solar cells with peak efficiencies of 19.9 %. Compared to the previously published peak efficiencies of 13.4 % this is a significant increase in efficiency by 6.5 % absolute. The developed process sequence reduces the process steps for solar cell fabrication and simultaneously decreases production cost by around 17 % compared to sequential diffusion. This reduces the cost of this cell process to a point where it is comparable in cost and efficiency with established technology for p-type passivated emitter and rear cells.

For the first time a detailed electrical characterization clarifies the influence of a process parameter (the $\text{N}_2\text{-POCl}_3$ gas flow) on the electrical properties of the back surface field (BSF) and on bifacial n-type solar cells. We show that a reduction in the doping concentration of the BSF increases cell conversion efficiency as long as inactive phosphorus is present. For textured surfaces passivated by SiN_x layers doping profiles without inactive phosphorus, a reduction in doping concentration decreases Auger recombination which is compensated by an increase in surface recombination resulting in a decrease of cell efficiency.

Chapter 5 investigates the influence of the phosphorus doping concentration on the specific contact resistance of screen printed contacts. Here the use of the high temperature processes developed in Section 3.2 allows for a controlled manipulation of the surface near doping concentration. The influence of the doping profile on contact formation is investigated using scanning electron microscopy and TLM measurements.

In accordance to literature it is found that the area coverage of crystallites that are in direct contact with the bulk finger correlates with the specific contact resistance. For the first time this correlation is investigated quantitatively yielding the specific contact resistance of a single crystallite of $(3.3 \pm 0.2) \mu\Omega\text{cm}^2$. This value agrees within measurement accuracy with theoretically expected values, while previously published values deviated by up to 4 orders of magnitude.

The introduction of a new method allows for the first time for quantitatively separating the influence of direct and indirect current conduction. For the screen printing paste under investigation the assumption of exclusively direct current conduction allows for an adequate description of the experimental data.

Outlook

Since photovoltaics is a very broad area of research the techniques developed in this thesis may be used for the investigation of other solar cell concepts and materials. For example the directed manipulation of phosphorus doping profiles may be used for the formation of phosphorus emitters in p-type solar cells as well as front and back surface fields in n-type back junction solar cells. For each of these cell concepts the directed manipulation of the doping profile could help to determine the optimum doping profile and thus increase cell efficiency. It also allows for separating effects governed by the surface doping concentration, e.g. surface recombination, from effects that depend on the depth of the doping profile e.g. surface shielding from (minority) charge carriers.

The second new technique developed in this thesis is the quantitative separation of direct and indirect current conduction in silver thick film contacts. It would be interesting to investigate a screen printing paste that according to the manufacturer relies on indirect current conduction (tunneling). In principle this method may be applied broadly for the characterization of silver thick film metallization.

Concerning the diffusion of the oxidizing species through SiO_x layer deposited by APCVD, it would be of high interest to investigate the underlying microscopic mechanisms. An investigation of the microstructure could identify possible diffusion channels. One could also investigate the diffusion of other atoms. The comparison with thermally grown SiO_2 might even help to identify the diffusing species which causes the formation of the intermediate SiO_2 layer.

Co-Diffusion for bifacial n-type solar cells is still a developing field of research. In order to allow for industrial implementation the efficiency of the bifacial solar cell needs to be increase to about 21 %. In order to achieve this, multiple approaches will be necessary. One approach is a further investigation of the phosphorus doped BSF. Using the technique developed in Section 3.2 one could e.g. vary the depth of the doping profile and investigate its influence on cell efficiency. A second approach would be changes in the screen printed metallization with the aim to decrease the dark saturation current density in the metalized areas of the solar cell or the use of different metallization techniques such as plating.

In order to allow for module integration the reduction of currents under reverse bias conditions is necessary. Even for parallel resistances that do not limit cell efficiency and comply with specifications for p-type solar cells, the currents under reverse bias are too high to allow for module integration. Thus the relation between currents under reverse bias and

parallel resistance seems to be fundamentally different from p-type solar cells, which is to the author's knowledge not understood yet.

Appendix

A Code for the simulation of oxide growth

```
#!/usr/bin/python
# -*- coding: iso-8859-1 -*-

# Berechnung des Oxidwachstums an Grenzfläche SiO2/Si für verschiedene SiO2-Anfangsdicken
# Modelle sind aus Deal and Grove (Abk.: DG) (1965?) und Han and Helms (Abk.: HH) (1987)
# Input: - Tabelle mit Temperaturen und Zeitintervallen
#       - Tabelle mit Anfangsdicken
# Output: Oxidwachstum über Anfangsdicke
# Pro Masoud Model hinzugefügt

from math import sqrt,exp

class Oxiddicke:
    def __init__(self):
        # Einlesen der Daten
        data = []
        # Input: Tabelle mit Temperaturen und Zeitintervallen
        for line in open('tempKoeff_Diffusionssim03p2.txt','r').readlines()[1:]:
            data.append(line.strip().strip().split())
            self.temperature = [float(z[0].strip()) for z in data]
            self.time = [float(z[1].strip()) for z in data]
            self.O2Faktor = [float(z[2].strip()) for z in data]
        # erhalte die Länge der Anzahl der Einträge des Diffusionsrezepts
        def Laenge(self):
            return len(self.temperature)
        # Berechnung Oxidicke nach Deal Grove
        # O2Faktor entspricht der O2-Konzentration in der Gasatmosphäre des
        # Hochtemperaturschritts
        # Modell unterschätzt Oxidwachstum ca. um Faktor 2 bis 3
        def DickeDG(self,Anfangsdicke,length):
            Oxdick = Anfangsdicke
            for i in range(length):
                # kb Einheiten eV/K
                kb = 8.6173324*pow(10,-5)
                # T < 950°C, (100)-Oberfläche, aus P.Moynagh and P. Rosser
                B = 1.373*pow(10,7)*exp(-2.22/(kb*(self.temperature[i]+273.15)))
                BdurchA = 4.666*pow(10,5)*exp(-1.76/(kb*(self.temperature[i]+273.15)))
                A = B/BdurchA
                # Oxdick: Oxidicke über Wachstumsrate ausrechnen
                Oxdick = Oxdick + B*self.O2Faktor[i]*self.time[i]/(2*Oxdick +
                self.O2Faktor[i]**(0.5) *A)
            return Oxdick
        # Berechnung nach Massoud 1987, JAP, Analytical relationship for the oxidation of silicon in
        # dry oxygen in the thin-film regime
        def DickeMas(self,Anfangsdicke,length):
```

```

Oxdick = Anfangsdicke
time = 0
for i in range(length):
    # kb Einheiten eV/K
    kb = 8.6173324*pow(10,-5)
    # T < 1000°C, (100)-Oberfläche, aus Massoud 1987 applied physics
    K1=2.49*pow(10,13)*exp(-2.18/(kb*(self.temperature[i]+273.15)))*60*10**-8 #
K1 (um^2/h)
    K2=3.72*pow(10,13)*exp(-2.28/(kb*(self.temperature[i]+273.15)))*60*10**-8 #
K1 (um^2/h)
    tau1= 4.14*pow(10,-6)*exp(1.38/(kb*(self.temperature[i]+273.15)))/60 #tau (h)
    tau2=2.71*pow(10,-7)*exp(1.88/(kb*(self.temperature[i]+273.15)))/60 #tau (h)
    B = 1.373*pow(10,7)*exp(-2.22/(kb*(self.temperature[i]+273.15)))
    BdurchA = 4.666*pow(10,5)*exp(-1.76/(kb*(self.temperature[i]+273.15)))
    A = B/BdurchA
    # Oxdick: Oxiddicke über Wachstumsrate ausrechnen
    time = time + self.time[i]
    Oxdick = Oxdick + self.O2Faktor[i]*(B+K1*exp(-time/tau1)+K2*exp(-
time/tau2))/(2*Oxdick + A*self.O2Faktor[i]**0.5)*self.time[i]
    return Oxdick
# Berechnung Oxidicke nach Han und Helms (Parallele Oxidation)
# Modell passt am wenigsten auf experminetelle Daten
def DickeHH(self,Anfangsdicke,length):
    Oxdick = Anfangsdicke
    for i in range(length):
        # kb Einheiten eV/K
        kb = 8.6173324*pow(10,-5)
        # Han und Helms, Einheiten in um und h umgerechnet. Faktor (60*pow(10,-8))
        B1 = 6.5*pow(10,11)*exp(-2.2/(kb*(self.temperature[i]+273.15)))*60*pow(10,-8)
        A1 = 0
        B2 = 2.6*pow(10,10)*exp(-1.6/(kb*(self.temperature[i]+273.15)))*60*pow(10,-8)
        B2durchA2 = 2.6*pow(10,8)*exp(-
1.9/(kb*(self.temperature[i]+273.15)))*60*pow(10,-4)
        A2 = B2/B2durchA2
        #print A1, B1, A2, B2
        # wenn Anfangsdicke < 0.0008 divergiert folgende Formel, deshalb 2.
Oxidationsmechanismus für Schichtdicken kleiner 0.8nm nicht berücksichtigt
        if Oxdick <0.000000001:
            Oxidation2 = 0
        else:
            Oxidation2 = B1*self.O2Faktor[i]*self.time[i]/(2*Oxdick)
            Oxdick = Oxdick + B2*self.O2Faktor[i]*self.time[i]/(2*Oxdick + A2) + Oxidation2
        return Oxdick

# ----- Ausführung des Programms -----

# Erhalte die Länge der Diffusionstabelle
Oinit = Oxiddicke()
length = int(Oinit.Laenge())

datalist = []
for line in open('Anfangsdicke.txt', 'r').readlines()[1:]:
    datalist.append(line.strip().split())
Anfangsdicke = [float(z[0].strip()) for z in datalist]

```

```
# In Oxiddicke_Startdicke wird das integrierte Oxidwachstum für verschiedene Anfangsdicken
gespeichert.
# Also ein Wert pro Anfangsdicke
Oxiddicke_Startdicke = []

# j läuft über Anfangsdicken
for j in range(len(Anfangsdicke)):
    # Achtung bei Änderung des Modells diese Zeile ändern !!!!!!!!!!!!!!!!!!!!!!!
    Odicke = Oxiddicke().DickeDG(Anfangsdicke[j],length)
    Oxiddicke_Startdicke.append((Odicke-Anfangsdicke[j])*10**3)
# Schreibe das Ergebnis in ErgebnissOxiddicken.txt
# Achtung bei Änderung des Modells diese Zeile ändern !!!!!!!!!!!!!!!!!!!!!!!
f = open('Ergebnis_Diffusionssim03P2.txt','w')
for i in range(len(Anfangsdicke)):
    f.writelines("%s \t %s \n" % (Anfangsdicke[i], Oxiddicke_Startdicke[i]))
f.close
```

B Simulation using the software tool Gridmaster

This appendix describes the modifications made to the software Gridmaster in this thesis, with the aim to allow for a relatively easy reproduction of the results. In the following first the general approach is described and then each modification made to the model is explained briefly.

The aim is to use the software Gridmaster to model the influence of recombination and resistance of the BSF on the solar cells IV parameters. The general approach is to substitute parameters that were originally meant for emitter description by parameters describing the BSF. The emitter is then incorporated using a constant contribution to recombination and series resistance and by an adjustment of the generated photocurrent.

In the following the chosen input parameters are listed following their position in the user interface in order to allow for simple reproduction of the simulations. For "cell dimensions" a length and width of 15.6 cm are chosen, following the experimental sample size in this thesis. The parameters in the category "grid fingers" meaning specific resistance of $3.5 \mu\Omega\text{cm}$, a finger width of $80 \mu\text{m}$ and a maximum finger height of $20 \mu\text{m}$ are typical values for silver based thick film metallization, which is used on the rear side of the simulated solar cell. The transparency of the grid is set to 100 % assuming only front side illumination. This takes into account that the rear grid does not introduce any shading and corresponds to the experimental conditions of the relevant IV measurements in this thesis. (The shading of the front side grid will be factored in by adaption of the photocurrent.)

The section "front busbar" is used to describe the three rear busbars with a width of $1500 \mu\text{m}$, a height of $24 \mu\text{m}$ and 24 external contact pins. Again the transparency is set to 100 % following the argumentation presented above.

In the input field "effective sheet resistance of the emitter" the resistance resulting from a parallel circuit of base and BSF is entered following the model described in Appendix C. For the base a specific resistance of $3 \Omega\text{cm}$ and a thickness of 0.018 cm are assumed.

The section "front contacts" is used to describe the rear contacts. The specific contact resistance is entered according to experimental data, while the "sheet resistance under metal" is set equal to the field "effective sheet resistance of the emitter".

The sections "contact pad related parameter" and "rear Aluminum" are adapted, so they do not influence the calculations. For each of the 27 p-pads the "area of one p-pad" is set to 0.27 cm^2 . The "sheet resistance of the rear aluminum" is set to 0, the number of external p-current pints to 1000 and the number of p-current columns to 3. The radius of the external contact pins is left at the default value of 0.1.

The irradiation is set at one sun corresponding to the experimental condition of the IV measurement.

In the section “selective emitter” all properties of “n⁺⁺” areas equal that of “n⁺” areas, since in this thesis the BSF is homogeneous. The short circuit current in the n⁺ and n⁺⁺ areas are set to 39 mA/cm², which includes the effects of shading of the front side metallization on the boron emitter. The dark saturation current density j_{0e-n+} is set equal to the experimentally determined value of the dark saturation current density in the passivated area of the BSF $J_{0pass,BSF}$. The input parameter that was originally used to describe the recombination in the base j_{0b} now represents recombination in the base and the emitter, which amounts to 180 fA/cm². The parameters j_{02-n} and j_{02-met} are set to 20 nA/cm². This takes into account that a change in the area coverage of the rear side metallization does not influence j_{02} .

The parallel resistance is set to 10 k Ω cm² in order to avoid an influence on the IV parameters. Finally an additional series resistance of 0.35 Ω cm² is introduced to account for resistive losses of the boron emitter and the associated metallization, corresponding to experimentally obtained values in this thesis. The number of fingers on the BSF is 93.

Table 8: Input parameters used for the analytical model describing the impact of the BSF properties on cell efficiency (Section 4.5)

Variable parameters describing the BSF						
$J_{0pass,BSF}$ [fA/cm ²]	$J_{0met,BSF}$ [fA/cm ²]	ρ_C [m Ω cm ²]	R_{sh} [Ω /sq]			
157-529	365-1334	2-11	43-108			

Constant parameters describing base and emitter				
Base resistivity [Ω cm]	Base thickness [μ m]	J_{0e} [fA/cm ²]	J_{sc} [mA/cm ²]	J_{02} [nA/cm ²]
3	180	180	39	20

Constant parameters describing mainly the rear side metallization						
Specific resistance of metal finger [μ Ω cm]	Rear finger width [μ m]	Rear BB width [μ m]	Effective finger height [μ m]	BB height [μ m]	Number of BB	External contact pins
3.5	80	1500	18.3	24	3	24

Table 8 lists the important input parameters used for the simulations presented in Section 4.5. As mentioned above the values in Table 8 are chosen in order to allow for a comparison of the simulated data with the experimental results in Section 4.6. The values in Table 9, which are chosen for an estimation of further optimization potential (Section 4.8) are chosen differently, since they incorporate e.g. expected improvements in production technology like smaller finger widths of the screen printed metallization.

Table 9: Input parameters used for the analytical model describing the impact of the BSF properties on cell efficiency (Section 4.8)

Variable parameters describing the BSF						
$J_{0pass,BSF}$	$J_{0met,BSF}$	ρ_C	R_{sh}			
[fA/cm ²]	[fA/cm ²]	[mΩcm ²]	[Ω/sq]			
157-529	365-1334	2-11	43-108			

Constant parameters describing base and emitter				
Base resistivity	Base thickness	J_{0e}	J_{sc}	J_{02}
[Ωcm]	[μm]	[fA/cm ²]	[mA/cm ²]	[nA/cm ²]
1.5	180	180	39	20

Constant parameters describing mainly the rear side metallization						
Specific resistance of metal finger	Rear finger width	Rear BB width	Effective finger height	BB height	Number of BB	External contact pins
[μΩcm]	[μm]	[μm]	[μm]	[μm]		
3.5	60	1500	18.3	24	3	24

C Model for lumped series resistance of BSF and base in PERT type structures

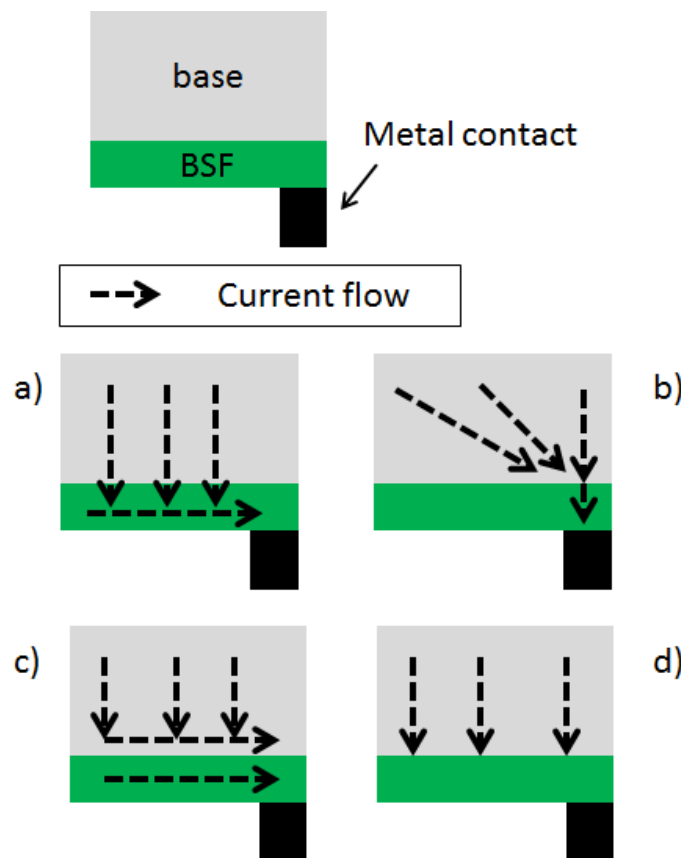


Figure 61: Schematic representation of current flow in base and full area back surface field (BSF). a) depicts the current flow when the sheet resistance of the BSF (R_{sh}) is small compared to the base resistance (R_{base}). Here the current flows vertically in the base and then laterally in the BSF (“base+BSF”). b) is valid if $R_{base} \ll R_{sh}$. The current takes the shortest path minimizing the path length in the BSF. c) visualizes the model used in this thesis, which assumes vertical current flow in the base and then lateral current flow through base and BSF (“base + BSF||base”). d) depicts the model “only base” used as an estimate for the minimum series resistance which only includes the contribution of vertical current flow in the base.

In this appendix the current flow and the resulting lumped series resistance in the base and a full area BSF are discussed. First special cases where analytical solutions are available are described qualitatively and then the model used in this thesis is explained. The situation under investigation is as follows: Current is injected homogeneously into the base and then

needs to reach the local rear metal contact. The current flow depends on material properties and follows the path of minimum resistance.

Two examples to visualize this concept are depicted in Figure 61 a) and b). Figure 61 a) describes a case where the resistance of the base R_{base} is much larger than the sheet resistance of the BSF (R_{BSF}). In order to minimize the total resistance, the current path minimizes the path length in the base ("base +BSF"). This leads to vertical current flow in the base and then horizontal current flow in the BSF. If the resistance of the base is much larger than the resistance of the BSF (Figure 61 b), the path length in the BSF is minimized. This leads to a spatially dependent current flow direction in the base and then vertical current flow through the BSF to the metal finger. Thus in summary, the precise current path depends amongst others on the resistance of base and BSF.

In this thesis the model sketched in Figure 61 c) is used. Here the current is proposed to flow vertically through the base and then horizontally through a parallel circuit of base and BSF ("base + BSF||base"). This decreases the total resistance compared to case a). In order to estimate the error of this model the current flow named "only base" is introduced in Figure 61 d). Here only the contribution of vertical current flow in the base to the lumped series is included, which corresponds to ($R_{\text{sh,BSF}} = 0\Omega/\text{sq}$). This allows for the calculation of a lower limit of the lumped series resistance.

In the following lumped series resistance resulting from the model used in this thesis ("base + BSF||base") as well as a lower limit ("only base") and an upper limit ("base + BSF") are calculated following Fellmeth et al. [150] using equations (0.1),(0.2), and(0.3):

$$R_{s,bBSF} = \rho_b \times d_b \quad (0.1)$$

(model "only base"),

$$R_{s,bBSF} = \rho_b \times d_b + 1/6 \times R_{\text{sh}} \times P/l_f \times (P/2 \times (l_f + w_{\text{BB}}/2)) \quad (0.2)$$

(model "base + BSF"),

$$R_{s,bBSF} = \rho_b \times d_b + 1/6 \times (1/R_{\text{sh}} + 1/(d_b \times \rho_b))^{-1} \times P/l_f \times (P/2 \times (l_f + w_{\text{BB}}/2)) \quad (0.3)$$

(model "base + BSF||base"),

with the base resistivity ρ_b , the sheet resistance of the BSF R_{sh} , the thickness of the base d_b ,

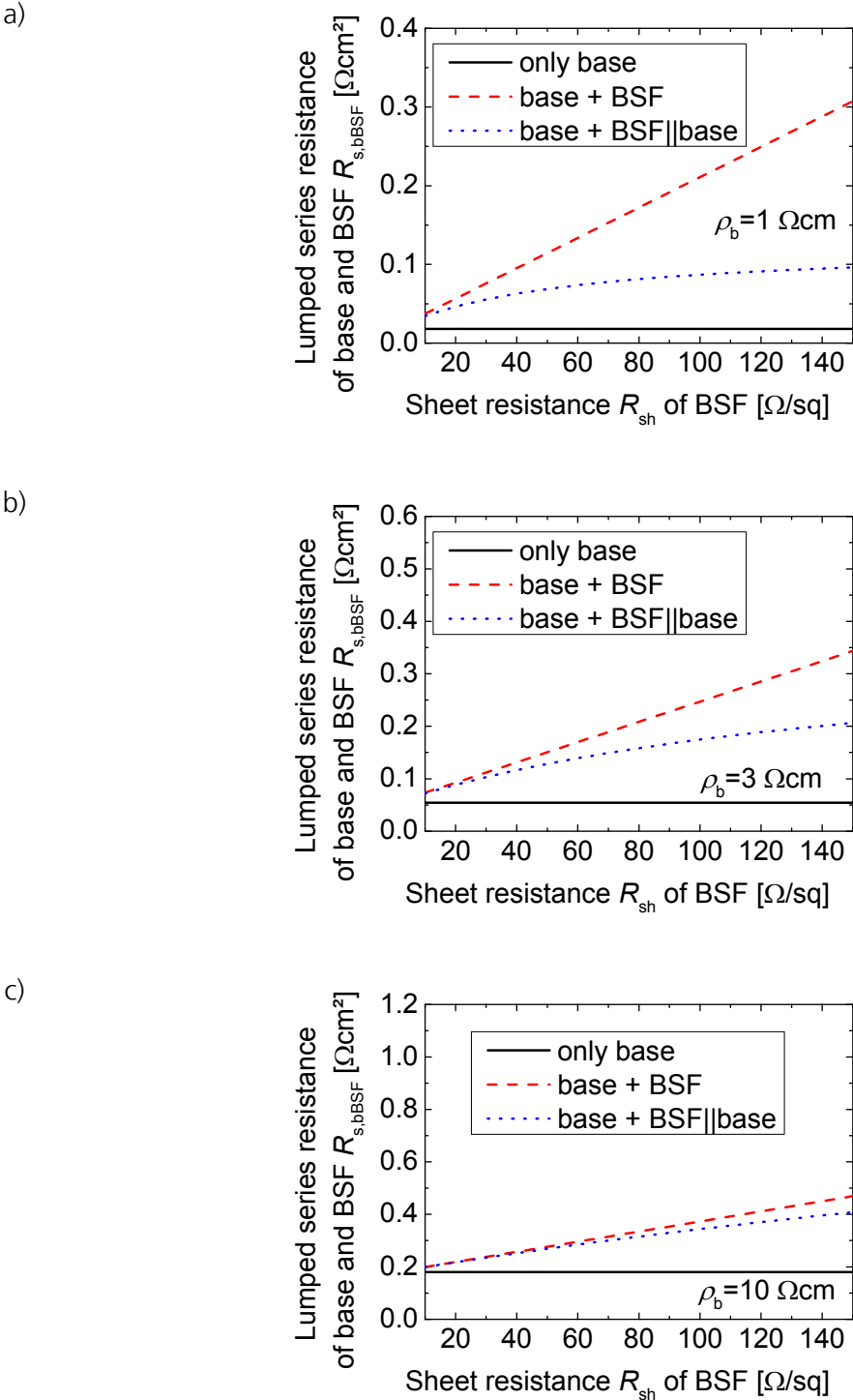


Figure 62: Calculated lumped series resistance of base and BSF $R_{s,bBSF}$ over sheet resistance R_{sh} of the BSF for base for different base resistivities of ρ_b of (a) 1 Ωcm , (b) 3 Ωcm , and (c) 10 Ωcm . The models used for calculation are schematically depicted in Figure 61 d) (“only base”), a) (“base + BSF”), and c) (“base +BSF||base”).

the finger length l_f , the distance between the fingers (pitch) P and the width of the busbars w_{BB} on the front of the solar cells. The equations presented above neglect current collection by busbars.

The evolution of the lumped series resistance $R_{s,bBSF}$ (Figure 62) is generated using the equations presented above and the parameters presented in Table 10.

Table 10: Input parameters used for the analytical modelling of lumped series resistance

ρ_b [Ωcm]	R_{sh} [Ω/sq]	d_b [cm]	l_f [mm]	P [mm]	w_{BB} [mm]
1-10	10-150	0.018	26	1.5	1.5

For the range of sheet resistance and base resistivities under investigation the lumped series resistance resulting from the model “base + BSF” is larger than the value resulting from “base + BSF||base”, which is itself larger than $R_{s,bBSF}$ calculated according to the model “only base”. Since the model “only base” underestimates $R_{s,bBSF}$ and the model “base + BSF” overestimates $R_{s,bBSF}$, the lumped series resistance resulting from the model “base + BSF||base” is between the minimum and maximum estimate of $R_{s,bBSF}$ for the complete parameter range under investigation. The relevant parameter space for this thesis covers base resistivities around 3 Ωcm and sheet resistances between 40 and 110 Ω/sq .

List of abbreviations

Q_{POCl_3}	N_2 - POCl_3 gas flow
d_{PSG}	Thickness of PSG layer
R_{sh}	Sheet resistance
BSF	Back surface field
FSF	Front surface field
J_0	Dark saturation current density
J_{sc}	Short circuit current density
V_{oc}	Open circuit voltage
FF	Fill factor
$J_{0\text{pass,BSF}}$	Dark saturation current density for passivated part of the BSF
$J_{0\text{met,BSF}}$	Dark saturation current density for metalized part of the BSF
SRV	Surface recombination velocity
J_{collect}	Collection current
p_{ox}	Partial pressure of oxygen
ρ_{C}	Specific contact resistance
n_{int}	Number of intervals for ramp up used for iterative modelling of SiO_2 layer growth
Δd_{SiO_2}	Thickness of additionally grown SiO_2 layer
d_i	Initial layer thickness
$J_{0\text{met}}$	Dark saturation current density for metalized areas
R_{p}	Parallel resistance after the two diode equation
$\rho_{\text{cryst,direct}}$	Area coverage of imprints (interpreted as crystals in direct contact with the silicon bulk)
$\rho_{\text{C,crystal}}$	Specific contact resistance of crystallite in direct contact with the bulk silicon
$\rho_{\text{C,tunnel}}$	Contribution from tunneling to specific contact resistance
η	Solar cell conversion efficiency
$APCVD$	Atmospheric pressure chemical vapor deposition

slm Standard liter per minute

Bibliography

1. Woodward, A., K.R. Smith, D. Campbell-Lendrum, D.D. Chadee, Y. Honda, Q. Liu, J. Olwoch, B. Revich, R. Sauerborn, and Z. Chafe, *Climate change and health: on the latest IPCC report*. The Lancet, 2014. **383**(9924): p. 1185-1189.
2. Energien, F.E., *Energiekonzept 2050: eine Vision für ein nachhaltiges Energiekonzept auf Basis von Energieeffizienz und 100% erneuerbaren Energien*. 2010: ForschungsVerbund Erneuerbare Energien.
3. Chapin, D.M., C.S. Fuller, and G.L. Pearson, *A new silicon p-n junction photocell for converting solar radiation into electrical power*. Journal of Applied Physics, 1954. **25**: p. 676-7.
4. Green, M.A., *The path to 25% silicon solar cell efficiency: History of silicon cell evolution*. Progress in Photovoltaics, 2009. **17**(3): p. 183-9.
5. Geerligs, L.J. and D. Macdonald, *Base doping and recombination activity of impurities in crystalline silicon solar cells*. Progress in Photovoltaics: Research and Applications, 2004. **12**(4): p. 309-16.
6. Smith, D.D., P.J. Cousins, A. Masad, S. Westerberg, M. Defensor, R. Ilaw, T. Dennis, N. Bergstrom, A. Leygo, X. Zhu, B. Meyers, B. Bourne, M. Shields, and D. Rose. *SunPower's Maxeon Gen III solar cell: high efficiency and energy yield*. in *Proceedings of the 39th IEEE Photovoltaic Specialists Conference*. 2013. Tampa, FL, USA.
7. Taguchi, M., A. Yano, S. Tohoda, K. Matsuyama, Y. Nakamura, T. Nishiwaki, K. Fujita, and E. Maruyama, *24.7% record efficiency HIT solar cell on thin silicon wafer*. 2013.
8. Schiele, Y., S. Wilking, F. Book, T. Wiedenmann, and G. Hahn, *Record Efficiency of PhosTop Solar Cells from n-type Cz UMG Silicon Wafers*. Energy Procedia, 2013. **38**: p. 459-466.
9. Burgers, A., L. Geerligs, A. Carr, A. Gutjahr, D. Saynova, X. Jingfeng, L. Gaofei, X. Zhuo, W. Hongfang, and A. Haijiao. *19.5% efficient n-type Si solar cells made in production*. in *26th European Photovoltaic Solar Energy Conference*. 2011.
10. Hezel, R., *Novel applications of bifacial solar cells*. Progress in Photovoltaics: Research and Applications, 2003. **11**(8): p. 549-556.
11. Bueno, G., I. Freire, K. Varner, L. Pérez, R. Lago, J.C. Jimeno, J. Salami, H. Kerp, K. Albertsen, and A. Shaikh. *Simultaneous diffusion of screen printed boron and phosphorus*

paste for bifacial silicon solar cells. in *Proceedings of the 20th European Photovoltaic Solar Energy Conference.* 2005. Barcelona, Spain.

12. Deal, B.E. and A.S. Grove, *General relationship for the thermal oxidation of silicon.* Journal of Applied Physics, 1965. **36**(12): p. 3770-8.

13. Massoud, H.Z., J.D. Plummer, and E.A. Irene, *Thermal oxidation of silicon in dry oxygen growth-rate enhancement in the thin regime. I. Experimental results.* Journal of the Electrochemical Society: Solid-State Science and Technology, 1985. **132**(11): p. 2685-93.

14. Massoud, H.Z., J.D. Plummer, and E.A. Irene, *Thermal oxidation of silicon in dry oxygen: growth-rate enhancement in the thin regime. II. Physical Mechanisms.* Journal of the Electrochemical Society: Solid-State Science and Technology, 1985. **132**(11): p. 2693-700.

15. Ghoshtagore, R.N., *Phosphorus diffusion processes in SiO₂ films.* Thin Solid Films, 1975. **25**(2): p. 501-513.

16. Rothhardt, P., R. Keding, A. Wolf, and D. Biro, *Co - diffusion from solid sources for bifacial n - type solar cells.* physica status solidi (RRL)-Rapid Research Letters, 2013. **7**(9): p. 623-626.

17. Lohmüller, E., B. Thaidigsmann, F. Clement, A. Wolf, and D. Biro, *Transfer of the HIP-MWT Solar Cell Concept to n-type Silicon.* Energy Procedia, 2013. **38**(0): p. 436-42.

18. Lohmüller, E., S. Werner, J. Schön, M. Thanasa, S. Mack, W. Wolke, A. Wolf, F. Clement, and D. Biro. *Depletion of boron-doped surfaces protected with barrier layers during POCl₃-Diffusion.* in *Proceedings of the 28th European Photovoltaic Solar Energy Conference and Exhibition.* 2013. Paris, France.

19. Pichler, P., *Intrinsic Point Defects, Impurities, and Their Diffusion in Silicon.* Computational Microelectronics, ed. S. Selberherr. 2004: Springer Verlag. 592.

20. Bentzen, A., A. Holt, J.S. Christensen, and B.G. Svensson, *High concentration in-diffusion of phosphorus in Si from a spray-on source.* Journal of Applied Physics, 2006. **99**: p. 064502.

21. Bentzen, A., *Phosphorus diffusion and gettering in silicon solar cells* in *Department of Physics.* 2006, University of Oslo: Oslo.

22. Vick, G. and K. Whittle, *Solid solubility and diffusion coefficients of boron in silicon.* Journal of the Electrochemical Society, 1969. **116**(8): p. 1142-1144.

23. Yoshida, M., M. Morooka, M. Takahashi, and H. Tomokage, *Effective Diffusion Coefficient and Controlling Process of P Diffusion in Si Based on the Pair Diffusion Models of Vacancy and Interstitial Mechanisms.* Japanese Journal of Applied Physics, 2000. **39**(5R): p. 2483.

24. Seeger, A. and K. Chik, *Diffusion mechanisms and point defects in silicon and germanium*. *physica status solidi (b)*, 1968. **29**(2): p. 455-542.
25. Fair, R.B. and P.N. Pappas, *Diffusion of Ion - Implanted B in High Concentration P - and As - Doped Silicon*. *Journal of the Electrochemical Society*, 1975. **122**(9): p. 1241-1244.
26. Hu, S., *Formation of stacking faults and enhanced diffusion in the oxidation of silicon*. *Journal of Applied Physics*, 1974. **45**(4): p. 1567-1573.
27. Mirabella, S., D. De Salvador, E. Napolitani, E. Bruno, and F. Priolo, *Mechanisms of boron diffusion in silicon and germanium*. *Journal of Applied Physics*, 2013. **113**(3): p. 031101.
28. Blamires, M.N., M. Matthews, and R. Nelson, *Improved profiles of electrical activity in boron implanted silicon*. *Physics Letters A*, 1968. **28**(3): p. 178-179.
29. Hull, R., *Properties of crystalline silicon*. 1999: IET.
30. Solmi, S., A. Parisini, R. Angelucci, A. Armigliato, D. Nobili, and L. Moro, *Dopant and carrier concentration in Si in equilibrium with monoclinic SiP precipitates*. *Physical Review B*, 1996. **53**(12): p. 7836-7841.
31. Kimmerle, A., A. Wolf, U. Belledin, and D. Biro. *Modelling carrier recombination in highly phosphorus-doped industrial emitters*. in *Proceedings of the 1st International Conference on Silicon Photovoltaics*. 2011. Freiburg, Germany: Elsevier Energy Procedia.
32. Cabrera, E., S. Olibet, D. Rudolph, P.E. Vullum, R. Kopecek, D. Reinke, C. Herzog, D. Schwaderer, and G. Schubert, *Impact of excess phosphorus doping and Si crystalline defects on Ag crystallite nucleation and growth in silver screen - printed Si solar cells*. *Progress in Photovoltaics: Research and Applications*, 2013.
33. Kessler, M.A., T. Ohrdes, B. Wolpensinger, and N.-P. Harder, *Charge carrier lifetime degradation in Cz silicon through the formation of a boron-rich layer during BBr₃ diffusion processes* *Semiconductor Science and Technology*, 2010. **25**(5): p. 055001.
34. Ryu, K., A. Upadhyaya, H.-J. Song, C.-J. Choi, A. Rohatgi, and Y.-W. Ok, *Chemical etching of boron-rich layer and its impact on high efficiency n-type silicon solar cells*. *Applied Physics Letters*, 2012. **101**(7): p. 073902.
35. Arai, E., H. Nakamura, and Y. Terunuma, *Interface reactions of B₂O₃-Si system and boron diffusion into silicon*. *Journal of the Electrochemical Society: Solid-State Science and Technology*, 1973. **120**(7): p. 980-7.
36. Kuzmich, W., *Ionization of impurities in silicon*. *Solid State Electronics*, 1986. **29**(12): p. 1223-7.

37. Goetzberger, A., B. Voß, and J. Knobloch, *Sonnenenergie: Photovoltaik - Physik und Technologie der Solarzelle*. Vol. 2., überarbeitete und erweiterte Auflage mit 131 Abbildungen und 2 Tabellen 1997, Freiburg im Breisgau: B. G. Teubner Stuttgart 1979. 261.
38. Ronen, R.S. and P.H. Robinson, *Hydrogen Chloride and Chlorine Gettering: An Effective Technique for Improving Performance of Silicon Devices*. Journal of the Electrochemical Society, 1972. **119**(6): p. 747-752.
39. Chen, R., H. Wagner, A. Dastgheib-Shirazi, M. Kessler, Z. Zhu, V. Shutthanandan, P.P. Altermatt, and S.T. Dunham, *A model for phosphosilicate glass deposition via POCl₃ for control of phosphorus dose in Si*. Journal of Applied Physics, 2012. **112**(12): p. 124912.
40. Han, C.-J. and C.R. Helms, *Parallel oxidation mechanism for Si oxidation in dry O₂*. Journal of the Electrochemical Society: Solid-State Science and Technology, 1987. **134**(5): p. 1297-302.
41. Moynagh, P.B. and P.J. Rosser, *Thermal oxidation of Si*, in *Properties of silicon*. 1987, INSPEC, The Institution of Electrical Engineers. p. 469-79.
42. Wotke, E., *Emitterbildung und Emitterpassivierung für hocheffiziente Industriesolarzellen*, in *Studiengang Umwelttechnik / Regenerative Energien*. 2008, Fachhochschule für Technik und Wirtschaft Berlin: Freiburg im Breisgau. p. 96.
43. Mols, B. and R. Oliemans, *A turbulent diffusion model for particle dispersion and deposition in horizontal tube flow*. International journal of multiphase flow, 1998. **24**(1): p. 55-75.
44. Howell, S., F. Ulacia, and C. Werner. *Numerical Simulation of Gas Flow and Temperature in a Diffusion Furnace*. in *Solid State Device Research Conference, 1989. ESSDERC'89. 19th European*. 1989: IEEE.
45. Ulacia, J. and C. Werner, *Equipment Simulation. II*. Solid State Technology, 1990. **33**(12): p. 71-74.
46. Schroder, D.K., *Semiconductor material and device characterization*. 3rd ed. 2006, Hoboken, New Jersey, USA: John Wiley & Sons. 790.
47. Ambridge, T., J.L. Stevenson, and R.M. Redstall, *Applications of Electrochemical Methods for Semiconductor Characterization I. Highly Reproducible Carrier Concentration Profiling of VPE "Hi - Lo"*. Journal of the Electrochemical Society, 1980. **127**(1): p. 222-228.
48. Blood, P., *Capacitance-voltage profiling and the characterisation of III-V semiconductors using electrolyte barriers*. Semiconductor Science and Technology, 1986. **1**(1): p. 7.

-
49. Komatsu, Y., D. Harata, E.W. Schuring, A.H. Vlooswijk, S. Katori, S. Fujita, P.R. Venema, and I. Cesar, *Calibration of electrochemical capacitance-voltage method on pyramid texture surface using scanning electron microscopy*. Energy Procedia, 2013. **38**: p. 94-100.
50. Bock, R., P.P. Altermatt, and J. Schmidt, *Accurate extraction of doping profiles from electrochemical capacitance voltage measurements*. WIP Munich, Proc. 23rd EU PVSEC, Valencia,(Sept. 2008), 2008: p. 1510-1513.
51. Sinton, R.A., A. Cuevas, and M. Stuckings. *Quasi-steady-state photoconductance, a new method for solar cell material and device characterization*. in *Proceedings of the 25th IEEE Photovoltaic Specialists Conference*. 1996. Washington DC, USA: IEEE; New York, NY, USA.
52. Cuevas, A., M. Stocks, D. Macdonald, and R. Sinton. *Applications of the quasi-steady-state photoconductance technique*. in *Proceedings of the 2nd World Conference on Photovoltaic Energy Conversion*. 1998. Vienna, Austria.
53. Kimmerle, A., P. Rothhardt, A. Wolf, and R.A. Sinton, *Increased Reliability for J_0 -analysis by QSSPC*. Energy Procedia, 2014. **55**: p. 101-106.
54. Sinton, R.A., *User Manual WCT-100 Photoconductance Tool*. 2003, Sinton Consulting. p. 60.
55. IEC, *Photovoltaic devices - part 3: measurement principles for terrestrial photovoltaic (PV) solar devices with reference spectral irradiance data*. . 2nd ed. International Standard, IEC 60904-3. 2008: International Electrotechnical Commission.
56. Krieg, A., *Inbetriebnahme und Weiterentwicklung eines automatisierten IV-Kennlinienmessplatzes und Entwicklung eines Verfahrens zur Materialverfolgung in der Solarzellenproduktion*, in *Fachbereich Ingenieurwissenschaften*. 2007, Fachhochschule für Technik und Wirtschaft Berlin: Freiburg im Breisgau. p. 77.
57. Krieg, A., A. Weil, E. Schäffer, J. Hohl-Ebinger, W. Warta, and S. Rein. *Accuracy of inline IV measurements under industrial conditions*. in *Proceedings of the 22nd European Photovoltaic Solar Energy Conference 2007*. Milan, Italy.
58. Shockley, W., *Research and investigation of inverse epitaxial UHF power transistors*. Report No AI-TOR-64-207 Air Force At. Lab. Wright-Patterson Air Force Base Ohio, 1964.
59. Berger, H.H., *Contact resistance and contact resistivity*. Journal of the Electrochemical Society, 1972. **119**(4): p. 507-14.
60. Berger, H.H. *Contact resistance on diffused resistors*. in *IEEE International Solid-State Circuits Conference*. 1969.

61. Murrmann, H. and D. Widmann, *Current crowding on metal contacts to planar devices*. IEEE Transactions on Electron Devices, 1969. **16**(12): p. 1022-4.
62. Schroder, D.K. and D.L. Meier, *Solar cell contact resistance - a review*. IEEE Transactions on Electron Devices, 1984. **ED-31**(5): p. 637-47.
63. Benninghoven, A., *Surface analysis by means of ion beams*. Critical Reviews in Solid State and Material Sciences, 1976. **6**(3): p. 291-316.
64. Woollam, J.A., *User Manual WVASE32*. 2004.
65. El-Gomati, M., T. Wells, I. Mullerova, L. Frank, and H. Jayakody, *Why is it that differently doped regions in semiconductors are visible in low voltage SEM?* Electron Devices, IEEE Transactions on, 2004. **51**(2): p. 288-292.
66. Spitz, M., U. Belledin, and S. Rein. *Fast inductive inline measurement of the emitter sheet resistance in industrial solar cell fabrication*. in *Proceedings of the 22nd European Photovoltaic Solar Energy Conference*. 2007. Milan, Italy.
67. Valdes, L.B., *Resistivity measurements on germanium for transistors*. Proceedings of the IRE, 1954. **42**(2): p. 420-427.
68. Bentzen, A. *PHOSPHORUS AND BORON DIFFUSION An industrial perspective?* in *nPV workshop*. 2011. Konstanz.
69. Buck, T., R. Kopecek, J. Libal, A. Herguth, K. Peter, I. Röver, K. Wambach, and B. Geerligs. *Industrial screen printed n-type silicon solar cells with front boron emitter and efficiencies exceeding 17%*. in *Proceedings of the 21th European Photovoltaic Solar Energy Conference*. 2006.
70. Ghoshtagore, R.N., *Silicon dioxide masking of phosphorus diffusion in silicon*. Solid-State Electronics, 1975. **18**(5): p. 399-406.
71. Eldridge, J. and P. Balk, *Formation of phosphosilicate glass films on silicon dioxide*. Transactions of the Metallurgical Society of AIME, 1968. **242**(3): p. 539-&.
72. Keding, R., R. Woehl, D. Stüwe, A. Fallisch, A. Hofmann, J. Rentsch, and D. Biro. *Diffusion and characterization of doped patterns in silicon from prepatterned boron- and phosphorus-doped silicate glasses*. in *Proceedings of the 26th European Photovoltaic Solar Energy Conference and Exhibition*. 2011. Hamburg, Germany.
73. Cuevas, A., P.A. Basore, G. Giroult-Matlakowski, and C. Dubois, *Surface recombination velocity of highly doped n-type silicon*. Journal of Applied Physics, 1996. **80**(6): p. 3370-5.
74. Cuevas, A. *A good recipe to make silicon solar cells*. in *Proceedings of the 22nd IEEE Photovoltaic Specialists Conference*. 1991. Las Vegas, Nevada, USA.

75. Sah, C., H. Sello, and D. Tremere, *Diffusion of phosphorus in silicon oxide film*. Journal of Physics and Chemistry of Solids, 1959. **11**(3): p. 288-298.
76. Grove, A.S., O. Leistiko, and C.T. Sah, *Redistribution of acceptor and donor impurities during thermal oxidation of silicon*. Journal of Applied Physics, 1964. **35**(9): p. 2695-701.
77. Bin Tanvir, N., R. Keding, P. Rothhardt, A. Meier, A. Wolf, H. Reinecke, and D. Biro, *Co-Diffusion Sources and Barriers for the Assembly of Back-Contact Back-Junction Solar Cells*. submitted.
78. Rothhardt, P., T. Stoffels, R. Keding, U. Belledin, A. Wolf, and D. Biro. *Control of phosphorus doping profiles for co-diffusion processes*. in *Proceedings of the 27th European Photovoltaic Solar Energy Conference and Exhibition*. 2012. Frankfurt, Germany.
79. Dastgheib-Shirazi, A., M. Steyer, G. Micard, H. Wagner, and P.P. Altermatt, *Relationships between diffusion parameters and phosphorus precipitation during the POCl₃ diffusion process*. Energy Procedia, 2013. **38**: p. 254 - 262.
80. Nobili, D., A. Armigliato, M. Finetti, and S. Solmi, *Precipitation as the phenomenon responsible for the electrically inactive phosphorus in silicon*. Journal of Applied Physics, 1982. **53**(3): p. 1484-91.
81. Keding, R., P. Rothhardt, C. Roters, A. Fallisch, S. Hohage, M. Hofmann, R. Woehl, D. Borchert, and D. Biro. *SILICON DOPING PERFORMED BY DIFFERENT DIFFUSION SOURCES AIMING CO-DIFFUSION*. in *27th EUPVSEC*. 2012. Frankfurt, Germany.
82. Fritz, S., S. Riegel, S. Gloger, D. Kohler, M. König, M. Hörtheis, and G. Hahn, *Influence of Emitter Properties on Contact Formation to P⁺ Silicon*. Energy Procedia, 2013. **38**: p. 720-724.
83. Schiele, Y., S. Fahr, S. Joos, G. Hahn, and B. Terheiden, *Study on boron emitter formation by BBr₃ diffusion for n-type Si solar cell applications*. Proc 28th EU PVSEC. Paris, France, 2013: p. 1242-1247.
84. Benick, J., B. Hoex, G. Dingemans, A. Richter, M. Hermle, and S.W. Glunz *High-efficiency n-type silicon solar cells with front side boron emitter*. in *Proceedings of the 24th European Photovoltaic Solar Energy Conference*. 2009. Hamburg, Germany.
85. Edler, A., *Development of bifacial n-type solar cells for industrial application*, in *Mathematisch-Naturwissenschaftliche Sektion - Fachbereich Physik*. 2014, Universität Konstanz. p. 142.
86. Rothhardt, P., C. Demberger, A. Wolf, and D. Biro, *Co-diffusion from APCVD BSG and POCl₃ for Industrial n-type Solar Cells*. Energy Procedia, 2013. **38**(0): p. 305-11.

87. Klaassen, D.B.M., *A unified mobility model for device simulation - I. Model equations and concentration dependence*. Solid-State Electronics, 1992. **35**(7): p. 953-9.
88. Klaassen, D.B.M., *A unified mobility model for device simulation - II. Temperature dependence of carrier mobility and lifetime*. Solid State Electronics, 1992. **35**(7): p. 961-7.
89. Negrini, P., A. Ravaglia, and S. Solmi, *Boron predeposition in silicon using BBr₃*. Journal of the Electrochemical Society: Solid-State Science and Technology, 1978. **125**(4): p. 609-13.
90. Kurachi, I. and K. Yoshioka, *Enhancement and retardation of thermal boron diffusion in silicon from atmospheric pressure chemical vapor deposited boron silicate glass film*. Japanese Journal of Applied Physics, 2014. **53**(3): p. 036504.
91. Kessler, M.A., T. Ohrdes, B. Wolpensinger, R. Bock, and N.-P. Harder. *Characterisation and implications of the boron rich layer resulting from open-tube liquid source BBr₃ diffusion processes*. in *Proceedings of the 34th IEEE Photovoltaic Specialists Conference*. 2009. Philadelphia.
92. Kopecek, R., T. Buck, J. Libal, R. Petres, I. Röver, K. Wambach, R. Kinderman, L. Geerligs, and P. Fath, *Large area N-type multicrystalline silicon solar cells with B-emitter: efficiencies exceeding 14%*. Proc. 15th IPSEC, Shanghai, 2005.
93. Kessler, M.A., T. Ohrdes, B. Wolpensinger, and N.-P. Harder, *Charge carrier lifetime degradation in Cz silicon through the formation of a boron-rich layer during BBr₃ diffusion processes*. Semiconductor Science and Technology, 2010. **25**(5): p. 055001.
94. Schroder, D.K. and D.L. Meier, *Solar-Cell Contact Resistance - a Review*. IEEE Transactions on Electron Devices, 1984. **31**(5): p. 637-647.
95. McIntosh, K.R. and P.P. Altermatt. *A freeware 1d emitter model for silicon solar cells*. in *Proceedings of the 35th IEEE Photovoltaic Specialists Conference*. 2010. Honolulu, Hawaii, USA.
96. Hoex, B., J. Schmidt, R. Bock, P.P. Altermatt, M.C.M. van de Sanden, and W.M.M. Kessels, *Excellent passivation of highly doped p-type Si surfaces by the negative-charge-dielectric Al₂O₃*. Applied Physics Letters, 2007. **91**(112107): p. 112107/1-3.
97. Green, M.A., *Intrinsic concentration, effective densities of states, and effective mass in silicon*. Journal of Applied Physics, 1990. **67**(6): p. 2944-54.
98. Geerligs, L.J., I.G. Romijn, A.R. Burgers, N. Guillevin, A.W. Weeber, J.H. Bultman, W. Hongfang, L. Fang, Z. Wenchao, L. Gaofei, H. Zhiyan, X. Jingfeng, and A. Vlooswijk. *Progress in low-cost n-type silicon solar cell technology*. in *Proceedings of the 38th IEEE Photovoltaic Specialists Conference*. 2012. Austin, Texas.

99. Krause, J., R. Woehl, M. Rauer, C. Schmiga, J. Wilde, and D. Biro, *Microstructural and electrical properties of different-sized aluminum-alloyed contacts and their layer system on silicon surfaces*. Solar Energy Materials and Solar Cells, 2011. **95**(8): p. 2151-60.
100. Götzberger, A., J.C. Goldschmidt, M. Peters, and P. Löper, *Photovoltaik-Vorrichtung und deren Verwendung*, in *Deutsches Patent*. 2007: Germany.
101. Meier, S., *Charakterisierung mittels Gasphasenabscheidung bei Atmosphärendruck abgeschiedener Dotierschichtsysteme für Co-Diffusionsprozesse*, in *Fakultät für Mathematik und Physik*. 2014, Albert-Ludwigs-Universität Freiburg.
102. Rosencher, E., A. Straboni, S. Rigo, and G. Amsel, *An 180 study of the thermal oxidation of silicon in oxygen*. Applied Physics Letters, 1979. **34**(4): p. 254-256.
103. Kamigaki, Y. and Y. Itoh, *Thermal oxidation of silicon in various oxygen partial pressures diluted by nitrogen*. Journal of Applied Physics, 1977. **48**(7): p. 2891-2896.
104. Taniguchi, K., Y. Shibata, and C. Hamaguchi, *Theoretical model for self - interstitial generation at the Si/SiO₂ interface during thermal oxidation of silicon*. Journal of Applied Physics, 1989. **65**(7): p. 2723-2727.
105. Bazer-Bachi, B., C. Oliver, B. Semmache, Y. Pellegrin, M. Gauthier, N. Le Quang, and M. Lemiti. *Co-diffusion from boron doped oxide and POCl₃*. in *Proceedings of the 26th European Photovoltaic Solar Energy Conference and Exhibition*. 2011. Hamburg, Germany.
106. Lange, P., U. Schnakenberg, S. Ullerich, and H.J. Schliwinski, *Disorder in vitreous SiO₂: the effect of thermal annealing on structural properties*. Journal of Applied Physics, 1990. **68**(7): p. 3532-3537.
107. Schmiga, C., H. Nagel, and J. Schmidt, *19% efficient n - type Czochralski silicon solar cells with screen - printed aluminium - alloyed rear emitter*. Progress in Photovoltaics: Research and Applications, 2006. **14**(6): p. 533-539.
108. Urrejola, E., P. Kristiansen, A.-K. Soiland, and E. Enebakk, *POCl₃ diffusion with in-situ SiO₂ barrier for selective emitter multicrystalline solar grade silicon solar cells*. 2009: Bibliothek der Universität Konstanz.
109. Mack, S., A. Wolf, E. Wotke, A. Lemke, B. Holzinger, T. Dimitrova, D. Biro, and R. Preu. *Impact of solar cell manufacturing processes on thermal oxide-passivated silicon surfaces*. in *Proceedings of the 24th European Photovoltaic Solar Energy Conference, Hamburg, Germany*. 2009.
110. Erlat, A., R. Spontak, R. Clarke, T. Robinson, P. Haaland, Y. Tropsha, N. Harvey, and E. Vogler, *SiO_x gas barrier coatings on polymer substrates: morphology and gas transport considerations*. The Journal of Physical Chemistry B, 1999. **103**(29): p. 6047-6055.

111. Gould, H.J., *Determining p - and n - Type Conduction in Very Small Crystals*. Review of Scientific Instruments, 1962. **33**(12): p. 1471-1472.
112. Bazer-Bachi, B., P. Lill, M. Dahlinger, S.J. Eisele, R. Zapf-Gottwick, J.R. Köhler, and J.H. Werner. *OPTIMIZING P FURNACE DIFFUSION LAYERS FOR LASER DOPING*. in *EU PVSEC*. 2012. Frankfurt.
113. Hu, S. and T. Yeh, *Approximate Theory of Emitter - Push Effect*. Journal of Applied Physics, 1969. **40**(11): p. 4615-4620.
114. Strunk, H., U. Gösele, and B. Kolbesen, *Interstitial supersaturation near phosphorus - diffused emitter zones in silicon*. Applied Physics Letters, 1979. **34**(8): p. 530-532.
115. Hu, S., P. Fahey, and R. Dutton, *On models of phosphorus diffusion in silicon*. Journal of Applied Physics, 1983. **54**(12): p. 6912-6922.
116. Romijn, I., *Industrial n-type solar cells: towards 20% efficiency*. Photovoltaics International, 2012. **15**: p. 81-90.
117. Rothhardt, P., S. Meier, S. Maier, K. Jiang, A. Wolf, and D. Biro, *Characterization of POCl₃-based codiffusion processes for bifacial n-type solar cells*. IEEE Journal of Photovoltaics, 2014. **4**(3): p. 827-33.
118. Kane, D.E. and R.M. Swanson, *Effect of electron-hole scattering on the current flow in semiconductors*. Journal of Applied Physics, 1992. **72**(11): p. 5294-304.
119. Richter, A., F. Werner, A. Cuevas, J. Schmidt, and S.W. Glunz, *Improved parameterization of auger recombination in silicon*. Energy Procedia, 2012. **27**: p. 88-94.
120. Fellmeth, T., F. Clement, and D. Biro, *Analytical Modeling of Industrial-Related Silicon Solar Cells* IEEE JOURNAL OF PHOTOVOLTAICS, 2013. **PP**(99): p. 1-10.
121. Richter, A., S. Henneck, J. Benick, M. Hörteis, M. Hermle, and S.W. Glunz *Firing stable Al₂O₃/SiNx layer stack passivation for the front side boron emitter of n-type silicon solar cells*. in *Proceedings of the 25th European Photovoltaic Solar Energy Conference and Exhibition*. 2010. Valencia, Spain.
122. Boscke, T., D. Kania, A. Helbig, C. Schollhorn, M. Dupke, P. Sadler, M. Braun, T. Roth, D. Stichtenoth, and T. Wutherich, *Bifacial n-type cells with > 20% front-side efficiency for industrial production*. Photovoltaics, IEEE Journal of, 2013. **3**(2): p. 674-677.
123. Kimmerle, A., A. Wolf, U. Belledin, and B. Biro. *Modelling carrier recombination in highly phosphorus-doped industrial emitters*. in *Proceedings of the 1st International Conference on Silicon Photovoltaics*. 2011. Freiburg, Germany: Elsevier Energy Procedia.

124. Negrini, P., D. Nobili, and S. Solmi, *Kinetics of phosphorus predeposition in silicon using POCl₃*. Journal of Electrochemical Society: Solid-State Science and Technology, 1975. **122**(9): p. 1254-60.
125. Wagner, H., A. Dastgheib-Shirazi, R. Chen, S. Dunham, M. Kessler, and P. Altermatt. *Improving the predictive power of modeling the emitter diffusion by fully including the phosphosilicate glass (PSG) layer*. in *Photovoltaic Specialists Conference (PVSC), 2011 37th IEEE*. 2011: IEEE.
126. Solmi, S., A. Parisini, R. Angelucci, A. Armigliato, D. Nobili, and L. Moro, *Dopant and carrier concentration in Si in equilibrium with monoclinic SiP precipitates*. Physical Review B, 1996. **53**(12): p. 7836-41.
127. Kulushich, G., R. Zapf-Gottwick, V.X. Nguyen, and J.H. Werner, *Role of phosphorous in contact formation on silicon solar cells*. Physica Status Solidi RRL 2012. **6**(9-10): p. 370-2.
128. Basore, P.A. and D.A. Clugston. *PC1D version 4 for Windows: from analysis to design*. in *Proceedings of the 25th IEEE Photovoltaic Specialists Conference*. 1996. Washington D C.
129. Clugston, D.A. and P.A. Basore. *PC1D version 5: 32-bit solar cell modeling on personal computers*. in *Proceedings of the 26th IEEE Photovoltaic Specialists Conference*. 1997. Anaheim, California, USA: IEEE; New York, NY, USA.
130. Greulich, J., M. Glatthaar, and S. Rein, *Fill factor analysis of solar cells' current-voltage curves*. Progress in Photovoltaics: Research and Applications, 2010. **18**(7): p. 511-5.
131. Frey, A., J. Engelhardt, S. Gloger, G. Hahn, and B. Terheiden. *n-Type Bi-Facial Solar Cells with Boron Emitters from Doped PECVD Layers*. in *EUPVSEC*. 2014. Amsterdam.
132. Blévin, T., A. Lanterne, B. Grange, R. Cabal, J.P. Vilcot, and Y. Veschetti, *Development of industrial processes for the fabrication of high efficiency n-type PERT cells*. Solmat, 2014.
133. Schiele, Y., F. Book, C. Demberger, K. Jiang, and G. Hahn. *Co-Diffused APCVD Boron Rear Emitter with Selectively Etched-Back FSF for Industrial n-Type Si Solar Cells*. in *Proceedings of the 29th European Photovoltaic Solar Energy Conference and Exhibition*. 2014. Amsterdam, The Netherlands.
134. Nold, S., N. Voigt, L. Friedich, D. Weber, I. Hädrich, M. Mittag, H. Wirth, B. Thaidigsmann, M. Hofmann, J. Rentsch, and R. Preu. *Cost modelling of silicon solar cell production innovation along the PV value chain*. in *Proceedings of the 27th European Photovoltaic Solar Energy Conference and Exhibition*. 2012. Frankfurt, Germany.
135. Geisemeyer, I., F. Fertig, W. Warta, S. Rein, and M.C. Schubert. *Impact of reverse breakdown in shaded silicon solar cells on module level: simulation and experiment*. in

Proceedings of the 27th European Photovoltaic Solar Energy Conference and Exhibition. 2012. Frankfurt, Germany.

136. Thaidigsmann, B., S. Werner, S. Gutscher, F. Fertig, F. Clement, A. Wolf, and D. Biro. *Manipulation of the reverse bias behaviour of silicon solar cells*. in *Proceedings of the 21st International Photovoltaic Science and Engineering Conference*. 2011. Fukuoka, Japan.

137. Cabrera, E., S. Olibet, J. Glatz-Reichenbach, R. Kopecek, D. Reinke, and G. Schubert, *Experimental evidence of direct contact formation for the current transport in silver thick film metallized silicon emitters*. *Journal of Applied Physics*, 2011. **110**(11): p. 114511.

138. Ballif, C., D.M. Huljic, G. Willeke, and A. Hessler-Wyser, *Silver thick-film contacts on highly doped n-type silicon emitters: structural and electronic properties of the interface*. *Applied Physics Letters*, 2003. **82**(12): p. 1878-80.

139. Li, Z.G., L. Liang, and L.K. Cheng, *Electron microscopy study of front-side Ag contact in crystalline Si solar cells*. *Journal of Applied Physics*, 2009. **105**(6): p. 066102.

140. Li, Z.G., L. Liang, A.S. Ionkin, B.M. Fish, and M.E. Lewittes, *Microstructural comparison of silicon solar cells' front-side Ag contact and the evolution of current conduction mechanisms*. *Journal of Applied Physics*, 2011. **110**.

141. Schubert, G., F. Huster, and P. Fath, *Physical understanding of printed thick-film front contacts of crystalline Si solar cells—Review of existing models and recent developments*. *Solar Energy Materials & Solar Cells*, 2006. **90**: p. 3399-406.

142. Hilali, M.M., M.M. Al-Jassim, B. To, H. Moutinho, A. Rohatgi, and S. Asher, *Understanding the formation and temperature dependence of thick film Ag contacts on high-sheet-resistance Si emitters for solar cells* *Journal of the Electrochemical Society*, 2005. **152**(10): p. G 742-9.

143. Schubert, G., *Thick film metallisation of crystalline silicon solar cells* 2006, Universität Konstanz: Konstanz. p. 142.

144. Kulushich, G., R. Zapf-Gottwick, V.X. Nguyen, and J.H. Werner, *Role of Phosphorus in contact formation on silicon solar cells*. *Physica Status Solidi RRL*, 2012. **6**(9-10): p. 370-372.

145. Rothhardt, P., R. Hoenig, A. Wolf, and D. Biro, *Influence of surface near doping concentration on contact formation of silver thick film contacts*. submitted, 2014.

146. Kontermann, S., A. Ruf, R. Preu, and G. Willeke, *Simulating the interface morphology of silver thick film contacts on n-type Si-(100) and Si-(111)*. *Applied Physics Letters*, 2012. **101**: p. 121907.

147. Wagner, H., S. Steingrube, B. Wolpensinger, A. Dastgheib-Shirazi, R. Chen, S.T. Dunham, and P.P. Altermatt. *Analyzing emitter dopant inhomogeneities at textured Si*

surfaces by using 3D process and device simulations in combination with SEM imaging. in *Photovoltaic Specialists Conference (PVSC), 2012 38th IEEE*. 2012: IEEE.

148. Kontermann, S., M. Hörteis, M. Kasemann, A. Grohe, R. Preu, E. Pink, and T. Trupke, *Physical understanding of the behavior of silver thick-film contacts on n-type silicon under annealing conditions*. *Solar Energy Materials & Solar Cells*, 2009. **93**: p. 1630-35.

149. Kontermann, S., G. Willeke, and J. Bauer, *Electronic properties of nanoscale silver crystals at the interface of silver thick film contacts on n-type silicon*. *Applied Physics Letters*, 2010. **97**(19): p. 191910.

150. Fellmeth, T., F. Clement, and D. Biro, *Analytical Modeling of Industrial-Related Silicon Solar Cells*. *Photovoltaics, IEEE Journal of*, 2014. **4**(1): p. 504-513.

Publications

Publications directly relevant to the content of this thesis

Rothhardt, P., Meier, S., Maier, S., Jiang, K., Wolf, A., & Biro, D. (2014). Characterization of POCl₃-Based Codiffusion Processes for Bifacial N-Type Solar Cells, *IEEE Journal of Photovoltaics* **4**(3), 827-833

Rothhardt, P., Hoenig, R., Wolf, A., & Biro, D. Influence of surface near doping concentration on contact formation of silver thick film contacts, 2014, *submitted*

Rothhardt, P., Meier, S., Demberger, C., Wolf, A., & Biro, D. (2014). Co-diffused bifacial n-type solar cells (CoBiN). *Energy Procedia*, *55*, 287-294

Rothhardt, P., Demberger, C., Wolf, A., & Biro, D. (2013). Co-diffusion from APCVD BSG and POCl₃ for Industrial n-type Solar Cells. *Energy Procedia*, *38*, 305-311

Rothhardt, P., Demberger, D., Zunft, H., Jiang, K., Habermann, D., Wolf, A., Biro, D. (2012) Diffusion from doped glasses deposited by APCVD for industrial n-type solar cells, In *Proc. 22nd International Photovoltaic Science and Engineering Conference, Hangzhou, China*

Rothhardt, P., Stoffels, T., Keding, R., Belledin, U., Wolf, A., & Biro, D. (2012). Control of phosphorus doping profiles for co-diffusion processes. In *Proc. 27th European Photovoltaic Solar Energy Conference and Exhibition, Frankfurt, Germany*.

Patent applications

Rothhardt, P., Wolf, A., Stoffels, T., Biro, D., Verfahren zur Dotierung von Halbleitersubstraten sowie dotiertes Halbleitersubstrat DE 10 2012 018 746 A1

Rothhardt, P., Wolf, A., Biro, D., Belleding, U., Verfahren zur Dotierung von Halbleitersubstraten sowie dotiertes Halbleitersubstrat, DE 10 2012 025 429 A1

Other publications

Kimmerle, A., Rothhardt, P., Wolf, A., & Sinton, R. A. (2014). Increased Reliability for J_0 analysis by QSSPC. *Energy Procedia*, 55, 101-106.

Rothhardt, P., Keding, R., Wolf, A., & Biro, D. (2013). Co-diffusion from solid sources for bifacial n-type solar cells. *physica status solidi (RRL)-Rapid Research Letters*, 7(9), 623-626.

Keding, R., Rothhardt, P., Roters, C., Fallisch, A., Hohage, S., Hofmann, M., & Spitz, M. (2012). Silicon doping performed by different diffusion sources aiming co-diffusion. In *27th Eur. Photovoltaic Solar Energy Conf. Exhib., Frankfurt, Germany*.

Zamponi, F., Rothhardt, P., Stingl, J., Woerner, M., & Elsaesser, T. (2012). Ultrafast large-amplitude relocation of electronic charge in ionic crystals. *Proceedings of the National Academy of Sciences*, 109(14), 5207-5212.

Zamponi, F., Ansari, Z., Schmising, C. V. K., Rothhardt, P., Zhavoronkov, N., Woerner, M., & Haschke, M. (2009). Femtosecond hard X-ray plasma sources with a kilohertz repetition rate. *Applied Physics A*, 96(1), 51-58.

Danksagung

An erster Stelle gilt mein besonderer Dank Herrn Prof. Eicke R. Weber für motivierende Gespräche und hilfreiche inhaltliche Anregungen. Vielen Dank auch an Prof. Oliver Waldmann für die Bereitschaft das Zweitgutachten zu verfassen. Ich danke Ralf Preu für die freundliche Aufnahme in den Bereich “Produktionstechnologie und Qualitätssicherung” am Fraunhofer ISE. Daniel Biro danke ich für seine positive Ausstrahlung und die Idee APCVD für Co-Diffusionsprozesse zu nutzen. Meinem Arbeitsgruppenleiter Andreas Wolf gilt besonderer Dank unter anderem für geduldiges Erklären, genaues Nachfragen und viele hilfreiche inhaltliche Diskussionen und Anmerkungen. Bei meinem Diplomanden Sebastian Meier möchte ich mich für eine sowohl inhaltlich als auch menschlich sehr bereichernde Zusammenarbeit bedanken. Ebenso bei Thomas Stoffels und Emily Kopp für Hilfe bei der Entwicklung der POCl_3 basierten Co-diffusionsprozesse. Auch meinen Hiwis Lena und Clemens gebührt Dank, ohne euch wäre so manches Experiment nicht möglich gewesen. Des Weiteren gilt besonderer Dank Christoph Schwab für viele motivierende Gespräche, wenn ich das Gefühl hatte, dass nichts so läuft wie es soll. Ich bedanke mich außerdem für geduldiges Erklären unter anderem bei Sebastian Mack, Armin Richter, Achim Kimmerle, Johannes Greulich, Benjamin Thaidigsmann, Jan Benick, und Roman Keding um nur einzelne zu nennen. Des Weiteren bei den vielen Mitarbeitern des PVTEC für Prozessierung, Wartung der Anlagen und die vielen Dingen, die oft übersehen werden. Auch bei der Firma SCHMID möchte ich mich für eine sehr unkomplizierte und ergiebige Zusammenarbeit bedanken. Des Weiteren möchte ich mich bei vielen guten Freunden am Fraunhofer ISE für eine sehr bereichernde und schöne Zeit außerhalb der Arbeit bedanken.

Zum Schluss gilt ein besonderer Dank an viele Studenten aus meinen Tutoraten für interessante Diskussionen, komplizierte Fragen und die Möglichkeit den Tag mit etwas Produktivem abschließen zu können. Um Feynman zu zitieren: “I don't believe I can really do without teaching. The reason is, I have to have something so that when I don't

have any ideas and I'm not getting anywhere I can say to myself, At least I'm living; at least I'm doing something; I am making some contribution”.

Crystalline solar cells based on n-type silicon promise high energy conversion efficiencies. In order to allow for cost effective manufacturing, the present dissertation introduces the concept of co-diffusion, which greatly simplifies production and reduces cost. The co-diffusion approach is based on a doped layer deposited by atmospheric pressure chemical vapor deposition and an atmosphere containing POCl_3 and allows for the fabrication co-diffused bifacial n-type solar cells (CoBIN) with peak efficiencies of 19.9%.

